Universidade do Minho
Escola de Engenharia

João Henrique de Castro Fernandes

Large-scale, controlled growth of two-dimensional materials by chemical vapor deposition

novembro de 2021

Large scale, controlled frowth of two dimensional materials by chemical vapor deposition
João Fernandes
UMinho | 2021

Universidade do Minho
Escola de Engenharia

João Henrique de Castro Fernandes

Large-scale, controlled growth of two-dimensional materials by chemical vapor deposition

Dissertação de Mestrado
Engenharia Física

Trabalho efetuado sob a orientação do
Dr. Andrea Capasso
Professor Dr. João Pedro dos Santos Hall Agorreta de Alpuim

novembro de 2021

Acknowledgments

First and foremost, I am extremely grateful to my supervisor Dr. Andrea Capasso for all the support, constant availability to help, and guidance throughout this work. His expertise and experience have encouraged me during my research.

I am also profoundly grateful to Professor Pedro Alpuim for all the inspiring classes throughout my degree and for the opportunity to develop my thesis work at 2D Materials and Devices group at INL.

I would like to acknowledge all members from the 2DMD group at INL. Thanks for all the training, stimulating discussions, and good times.

Finally, I must express my very profound gratitude to my family and friends. A special word to my parents and brother that provided me with unfailing support and continuous encouragement throughout my years of study. To my friends, I thank them for the unwavering companionship and all the good moments we have experienced together.

Statement of Integrity

I hereby declare having conducted this academic work with integrity. I confirm that I have not used plagiarism or any form of undue use of information or falsification of results along the process leading to its elaboration.

I further declare that I have fully acknowledged the Code of Ethical Conduct of the University of Minho.

Abstract

In this work, the optimization of two atmospheric pressure chemical vapor deposition systems was carried out in order to grow two different bidimensional materials, namely hBN and $MoSe_2$. The first is an insulator with a structure similar to graphene and it is seen as an optimal candidate for several applications, in particular photonics and optoelectronics. The latter is a prominent semiconductor belonging to the family of two-dimensional transition metal dichalcogenides which demonstrated outstanding optoelectronic properties, such as thickness-dependent photoluminescence, combined with lightweight and flexibility. Several deposition parameters were investigated in parallel with an extensive characterization methodology carried out by optical microscopy, Raman spectroscopy, atomic-force microscopy, scanning-electron microscopy, x-ray photoelectron spectroscopy, energy dispersive x-ray spectroscopy and transmission electron microscopy. As a final result, reliable experimental procedures have been established which lead to the growth of few-layer polycrystalline hBN films (up to $20cm^2$) and μm-sized single crystals of monolayer $MoSe_2$. Selected samples were tested in experimental devices. The fluorescent properties of 2D hBN films were probed to quantify its performance as a single-photon emission source at room temperature. A sensing device based on 2D $MoSe_2$ was assembled to investigate the optical response of the material to various degree of tensile strain.

KEYWORDS

Chemical vapor deposition, hexagonal boron nitride, molybdenum diselenide, two-dimensional materials

Resumo

Neste trabalho, a otimização de dois sistemas de deposição química de vapores, operados à pressão atmosférica, foi levada a cabo a fim de depositar dois materiais bidimensionais diferentes: hBN e $MoSe_2$. O primeiro é um isolante com uma estrutura semelhante ao grafeno e é visto como um ótimo candidato para várias aplicações, em particular na área da fotónica e optoeletrónica. Por sua vez, o segundo é um semicondutor proeminente pertencente à família dos dicalcogenetos de metais de transição bidimensionais que demonstrou excelentes propriedades optoeletrónicas, em particular a dependência da sua fotoluminescência em função do número de camadas, combinadas com a sua leveza e flexibilidade. Vários parâmetros de deposição foram investigados em paralelo com uma extensa caracterização realizada através de microscopia ótica, espectroscopia Raman, microscopia de força atômica, microscopia eletrónica de varredura, espectroscopia de fotoeletrões de raios-X, espectroscopia de energia dispersiva de raios-X e microscopia eletrónica de transmissão. No final, obtiveram-se dois procedimentos experimentais confiáveis que levam ao crescimento de filmes policristalinos de hBN compostos por poucas camadas (até $20cm^2$) e cristais monoatómicos de $MoSe_2$ na ordem dos micrómetros. As amostras selecionadas foram testadas em dispositivos experimentais. As propriedades fluorescentes dos filmes de hBN foram medidas de modo quantificar seu desempenho como fonte de emissão de fotão único à temperatura ambiente. Um dispositivo de deteção baseado em 2D $MoSe_2$ foi montado de modo investigar a resposta ótica do material a vários graus de tensão.

Palavras-Chave

Deposição química de vapores, diseleneto de molibdénio, materiais bidimensionais, nitreto de boro hexagonal

Index

FIGURE INDEX

TABLE INDEX

LIST OF ABBREVIATIONS, INITIALS AND ACRONYMS

AB- Ammonia borane

aBN- Amorphous boron nitride

AFM- Atomic-force microscopy,

APCVD- Atmospheric pressure chemical vapor deposition

BN – Boron nitride

BN- Boron nitride

BNNS- Boron nitride nanosheets

BNNS- Boron nitride nanosheets

CB- Conduction band

cBN- Cubic boron nitride

CVD- Chemical vapor deposition

DIW- Deionzed water

DoS- Density of states

EDX/EDS- Energy dispersive x-ray spectroscopy

FET – Field effect transistor

hBN- Hexagonal boron nitride

HRTEM- High resolution transmission electron microscopy

IPA- Isopropyl alcohol

IR- Infrared

LED – Light emitting diode

LP- Lone-pair

LPCVD- Low pressure chemical vapor deposition

LPE- Liquid phase exfoliation

MBE- Molecular beam epitaxy

ML- Monolayer

$MoSe_2$- Molybdenium diselenide

NIR - Near infrared

OM- Optical microscope

PDMS- Poly(dimethylsiloxane)

PEN- Polyethylene naphthalate

PMMA- Poly(methyl 2-methylpropenoate)

PVD- Physical vapor deposition

PZT- Lead zirconate titanate

QD- Quantum dot

rBN- Rhombohedral boron nitride

RF- Radio frequency

SEM- Scanning-electron microscopy

SLG- Single layer graphene

SPE- Single photon emission

SPEs- Single photon emitters

tBN- Turbostratic boron nitride

TEM- Transmission electron microscopy

TMDCs- Transition metal dichalcogenides

UHV- Ultra high vacuum

VB- Valence band

vdW- van der walls

vdWHs- vand der walls heterosctrutures

wBN- Wurtzite boron ntiride

XPS- X-ray photoelectron spectroscopy

ZPL- Zero phonon line

ZPL- Zero phonon line

2D- Two-dimensiona

1. INTRODUCTION

Nanomaterials are paving the way to next generation of devices for several technologies, such as photonics, (opto)electronics and photovoltaics. A generic photonic system involves the generation, detection and manipulation of photons, achieved by using different technologies like optical fibers, lasers and detectors. In particular, photonic quantum information, a subfield that takes advantage of exploiting single photon as quantum information carriers, promise a revolution in the world of information processing, from simulation and computing to communication and sensing. A central building block in this field is a single photon emitter (SPE) — a source that emits exactly one photon at a time into a given spatiotemporal mode. In this regard, a viable platform that is able to produce bright and optically stable SPEs at room temperature is actively sought to further development of the field. Optoelectronics is a field under fast evolution. Novel photodetectors, excitonic light-emitting devices (LEDs) and optical generation of spin–valley currents are examples of devices exploited in recent years. The main goal is to achieve ultrahigh, ultrafast, ultrabroad and ultrasensitive devices for a variety of applications. Besides, flexible optoelectronic devices might play a key role in the development of bendable and wearable systems. Due to their inherent exceptional mechanical flexibility and strength, 2D materials provide an ideal platform for strain engineering, enabling versatile modulation and significant enhancement of their optical properties.

The use of two-dimensional (2D) materials have been proposed for the aforementioned technologies due to their host of superior optical and electronic properties. Atomically thin hexagonal boron nitride (hBN) is a typical insulator (with a crystal structure analogous to that of graphene) which shows novel optoelectrical properties combined with mechanical robustness, thermal stability, and chemical inertness. Furthermore, 2D transition metal dichalcogenides (TMDCs) are a famous group of semiconductor materials within 2D materials class that may be useful in this regard. Molybdenium diselenide ($MoSe_2$), in particular, demonstrated outstanding optoelectronic properties, such as thickness-dependent photoluminescence, combined with lightweight and flexibility. Nowadays, further experimental work is necessary to start integrating these materials in technology. The production of high-quality 2D crystals over wafer scales is the first critical required by the industry. Substantial efforts have been devoted to producing atomically thin 2D materials with large lateral dimensions, controllable and uniform thicknesses, and minimum defects. Among all, chemical vapor deposition (CVD) is one of the promising methods. By relying on chemical reactions, it enables tunable deposition rates as well as high-quality products with excellent conformality. However, due to the complicated growth mechanism, which involves

several interrelated parameters, maintaining the controllability, repeatability, and high quality of the CVD grown compound materials is still a big challenge.

In this thesis, CVD growth of atomically thin hBN and $MoSe_2$ was investigated. The respective growth procedures were optimized to achieve control over the materials properties, In terms of sample size and layer number. The result is a set of CVD parameters to consistently produce atomically thin hBN films and single-crystal monolayer $MoSe_2$ flakes. Sample characterization was carried out by optical microscopy, Raman spectroscopy, atomic-force microscopy, scanning-electron microscopy, x-ray photoelectron spectroscopy, energy dispersive x-ray spectroscopy and transmission electron microscopy. Furthermore, the grown samples of each material were evaluated in terms of practical applications.

The present dissertation is organized into six chapters. The first chapter starts by describing the motivation, addressing the main challenges, and referring the main goals of this thesis. A brief insight into the history, properties, production, and applications of 2D materials is also given. Furthermore, a more detailed allusion is done to both BN and TMDCs, which are the target materials in this work. The second chapter gives an overall review of the production methods used for 2D materials, with special emphasis on CVD technique, where a detailed overview is given. The following chapter introduces all characterization techniques used during the course of this work. Chapter 4 and 5 are respective to the experimental work and are organized following the same structure: description of the materials and methods used; discussion of the several optimization steps; extensive characterization of the optimized sample; the performance of the grown sample for a target application and conclusions. Finally, chapter 6 suggests some thoughts to be developed as future work.

1.1 2D Materials: properties, production and applications

A 2D material is defined as a material whose free charges are immobile in one spatial dimension, but mobile in the other two. This confinement of electrons in a plane breaks the periodicity in the direction perpendicular to the plane, which can greatly change the electronic band structure. The modified band structure gives rise to novel physical properties. Additionally, their higher surface area-to-volume ratio makes them more sensitive to their surroundings. These properties enable 2D materials to have new or superior functions, distinct from traditional bulk materials or thin films. Interest in 2D materials dates to the late 1970s and early 1980s. In 2004, the successful exfoliation of graphite into atomically thin 2D graphene sparked a resurrection of interest in 2D materials. Graphene is exceptionally strong, lightweight, and flexible, it has high optical transmittance, and allows electrons to move much faster than other materials with higher thermal conductivity. However, the lack of bandgap did not allow the use of this

material in (opto)electronic applications. The rapid and prosperous development of graphene stimulated numerous research interests on other 2D materials. More than one thousand structures of 2D materials have been predicted to be easily exfoliated to monolayers or multilayers with fascinating physical properties, forming a large family of 2D materials [1]. Among all, hBN and TMDCs have gathered a lot of attention. The first has a similar structure and lattice parameter to graphene and so it has been regarded as an ideal substrate for the graphene growth. On the other hand, bulk TMDCs are layered materials in which a plane of transition metal atoms, such as Mo or W, is sandwiched between two planes of chalcogen atoms (S, Se, or Te). Their general formula is thus MX_2 with M a transition metal element and X a chalcogen. Some representative examples of this class of materials are MoS_2, $MoSe_2$, WS_2, or $MoTe_2$. Some graphene analogues such as black phosphorene [2], borophene [3], silicene [4], germanane [5], stanene [6], and tellurene [7] have also been synthesized in the past few years. Although these 2D materials have an atomic layer structure similar to that of graphene, their physical properties are distinct from those of graphene. Thus, these 2D materials can act as complementary materials and have the potential for broader applications.

Extensive efforts have been dedicated to the synthesis of atomically thin materials with laterally large dimensions. Various approaches are investigated which can be typically assorted into two categories which entail top–down and bottom–up techniques. The most notable top–down approaches are exfoliation techniques, including liquid and mechanical exfoliation. Liquid exfoliation presents challenges in balancing produced quality vs large area yield of 2D flakes. Agglomerations, limited-sized 2D sheets with arbitrary shapes and random distribution on substrates, have been drawbacks of liquid-phase exfoliation. On the other hand, mechanical exfoliation is able to provide high-quality exfoliated 2D sheets, and innovative approaches have enhanced the lateral size and controllability in patterned transfer. However, its very low yield does not make it suitable for 2D production. Bottom–up approaches, mainly CVD, prevail as the most potent techniques so far. This method is industry-relevant and applicable to many materials with ease of operation. However, numerous operating parameters require thorough knowledge and engineering to obtain high-quality crystals. Engineering and tuning these parameters for the synthesis of each material will enhance controlling nucleation and growth rates leading to more homogenous growth with fewer defects and large 2D sheet sizes.

Although the breakthrough properties of graphene its integration into practical devices was not easy. Graphene is a semi-metal and can work as a good electrical conductor, but by definition has no electronic bandgap, which limits its application in (opto)electronic devices such as field-effect transistors (FETs), solar cells, photodetectors and light-emitting diodes (LEDs). This has led to a sub-field of research

dedicated to developing approaches (such as doping and nano-structuring) aimed at introducing a bandgap in graphene. Although stimulating, such approaches would increase the complexity and number of steps required for the preparation of the material, with adverse effects on its exceptional carrier mobility. Fortunately, other 2D materials with electronic properties complementary to those of graphene such as h-BN and the large group of TMDCs can be used in this regard. The techniques developed to synthesize, transfer and characterize graphene are most of the time compatible with these materials too. These materials consist of a covalently bonded, dangling-bond-free lattice and can weakly bound to neighboring similar materials by the weak van der Waals interactions. This makes it feasible to mix and match different 2D materials to create a wide range of van der Waals heterostructures (vdWHs) without the constraints of lattice matching and processing compatibility. Exploiting the novel properties in these vdWHs with a diverse layering of metals, semiconductors or insulators, new designs of electronic devices emerge, including tunnelling transistors, barristors and flexible electronics, as well as optoelectronic devices, including photodetectors, photovoltaics and light-emitting devices with unprecedented characteristics or unique functionalities.

1.2 Boron nitride: structure, properties and applications

Boron nitride (BN) is a III-V semiconductor compound exhibiting an equal number of B and N atoms. It is thought to be a synthetic material although a rare natural occurrence has been reported [8]. It exhibits extraordinary properties and is regarded as an important candidate for electronic, optical, and other engineering applications[9–11]. BN atomic orbitals can be either sp^2 or sp^3 hybridized, thus producing several crystalline forms. BN forms hexagonal (h) and rhombohedral (r) lattices via sp^2 hybridized bonding and forms cubic (c) or wurtzite (w) lattices via the sp^3 hybridization configuration. In fact, two less ordered sp^2 configured polymorphs, amorphous BN (aBN) and turbostratic BN (tBN), can form during the synthesis of hBN and rBN. The first one can be seen as disordered hBN and it is unstable in air, reacting with water vapor to form boric acid, boric oxides, and hydroxides. tBN, on the other hand, forms due to a fault in the c axis orientation of the hBN layers and this type of BN has also been reported to be unstable after long-term exposure to air, forming ammonium borate compounds. Among all the crystalline forms, the cubic and hexagonal phases are the most stable ones. cBN exhibits a zinc-blende structure consisting of tetrahedrally coordinated boron and nitrogen atoms, analogous to that of diamond, while hBN possesses a layered nature with each sp^2-bonded monolayer having a honeycomb structure formed of neighboring B and N atoms, strongly bonded by covalent interactions. The interaction between adjacent

layers is of the weak van der Waals (vdW) type. The four primary crystalline phases of BN are illustrated in Figure 1.

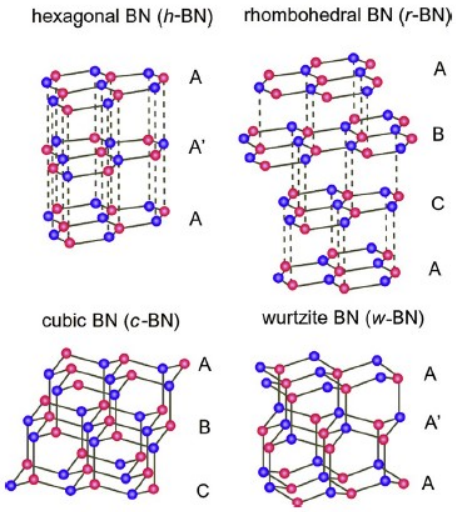

Figure 1. Structure schematics for the four-primary crystalline BN phases: h-BN, r-BN, c-BN and w-BN. Taken from Ref. [37]

hBN holds a lot of attention since it is an insulating analogue of graphite with a hexagonal crystal structure and a small lattice mismatch (~1.8%) with graphite, and so is an "ideal partner" for graphene and a promising key building block in van der Waals heterostructures. This layered structure of this crystalline form gives rise to different stacking configurations. Besides the AA' ground-state stacking configuration (where the B atoms in one hBN layer are positioned above the N atoms in the second hBN layer, and vice versa for the N atoms) AB stacking configuration is also reported to be energetically favorable in few-layer films [12]. In this later, B and N atoms in one hBN layer are translated with respect to the second hBN layer in the unit cell by a fraction of the in-plane lattice vector. Both possible stacking configurations are illustrated in Figure 2.

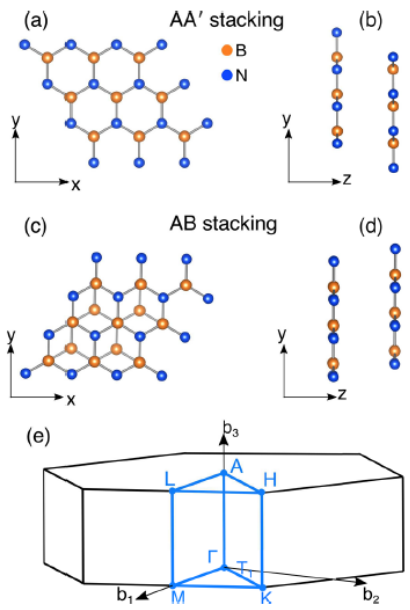

Figure 2. (a) Top view and (b) side view of the ground-state AA′ stacking configuration. (c) Top view and (d) side view of the AB stacking configuration.(e) Brillouin zone of bulk h-BN. Taken from Ref. [39]

The remarkable properties exhibited by BN-based nanomaterials have attracted much attention and have risen the expectations of breakthrough applications. During the last years, low-dimensional BN-based materials have been intensively exploited. Similar to the carbon allotropes of graphene, carbon nanotube, and fullerene, h-BN can form BN nanosheets [13], BN nanotubes [14] and BN fullerene [15]. In addition, various other exotic morphologies such as nanoribbons [16], nanowires [17], nanofibers [18] and foams [19] have also been reported. From far, BNNs are the most promising configuration. BNNS (or atomically thin hBN) have the same hexagonal structure as graphene but a white color, so they are sometimes called "white graphene". Due to their analogous crystal structures, atomically thin BN has many properties similar to those of graphene such as Young Modulus and breaking strength. However, it has also many properties distinct from those of graphene, which turns their combination attractive. The most well-known difference between them is their electrical conductivity: graphene is semi-metal whereas BNNS are insulating.

The outstanding physical properties of few-layer hBN made him become one serious candidate in large range of applications such as: substrate/gate dielectrics for 2D electronics; passivation/protection layer; 2D-based heterostructures and optics/photonics. Regarding low-dimensional electronics, substrates play a critically important role in their performance. Many features are crucial such as coupling, scattering from charged surface states, impurities as well as surface roughness and optical phonons. Compared with the traditional substrates such as SiO_2, SiC, or Al_2O_3, 2D hBN is considered very promising as

substrate, especially together with those 2D materials such as graphene, because of the minimal lattice mismatch involved and almost atomically flat surface that can be free of dangling bonds or surface charge traps [20]. In addition, the large bandgap, surface optical phonon modes (with energies two times higher than SiO_2), dielectric characteristics ($\varepsilon \sim 3–4$), high breakdown field ($V \sim 0.7\ V\ nm^{-1}$), and excellent thermal conductivity (600 times higher than that of SiO_2) render 2D hBN suitable in 2D electronics. As reported, graphene-FETs with hBN as substrate shown a mobility of 60 000 $cm^2\ V^{-1}\ s^{-1}$, which was three times larger than that with SiO_2, mainly attributed to the decreased scattering of the charge impurities [21]. Indeed, large-area graphene devices based on high-quality BNNs have been constructed which are shown to exhibit a threefold higher mobility and current on/off ratio, paving the way for potential large-scale applications of hBN in nanoelectronics. Besides that, 2D hBN can also be used as a gate dielectric for nanoelectronics. When compared with conventional oxide dielectrics, such as HfO_2 or SiO_2, 2D hBN is more reliable as there are no charge trapping/de-trapping and stress-induced leakage current, rendering the devices more robust and with a long lifetime [22]. Furthermore, the excellent electrical insulation, high thermal stability and chemical inertness makes 2D hBN suitable for passivation applications, especially together with other 2D materials. The degradation of intrinsic characteristics and deterioration of device performance could be effectively suppressed by encapsulation with hBN to cover the active regions. For example, the encapsulated graphene FET exhibited big ballistic transport an extremely high intrinsic charge carrier mobility indicating that the hBN encapsulation makes graphene highly insusceptible to the ambient atmosphere and effectively immune to other contamination [23]. As discussed before, the integration of different 2D materials have been extensively exploited in the recent years. Several types of vertical 2D heterostructures are constructed not only for the improved performance, but also for the rich functionalities and novel physical properties which can be used in opto-electronic devices, where they can be tuned by stacking sequence, orientation, interlayer coupling, and application of an external electric field. For example, a graphene/hBN system has been reported with a significant improvement in carrier mobility [21] and photo-induced doping effect [24]. Despite this rising interest in hBN and the large number of studies devoted to this material, with its seemingly simple crystal structure, the very basic question of the nature of its bandgap remains controversial. There is a strong contrast between band structure calculations, which predict an indirect bandgap crystal [25,26], and optical measurements, which indicate a direct bandgap [11]. More recently, it was demonstrated that bulk hBN has an indirect bandgap at 5.95 eV and that the optical properties of hBN are profoundly determined by phonon-assisted transitions [27]. The nature of the bandgap as well as the energy can change when going from bulk to few- or mono-layers counterparts. For monolayer hBN there is a clear

the existence of a direct-gap at around 6.1 eV [28]. This energy gap has a weak dependence on the thickness, in contrast with what happens for other materials. Also, 2D hBN exhibit a high transparency of 99% with wavelengths in the range of 250–900 nm, because of hardly any optical absorption, whereas a sharp absorption peak appears in the deep ultraviolet (DUV) range (200–220 nm) which suits him for DUV detection [29].

Furthermore, hBN appears as a viable platform to produce bright and optically stable single photon emitters (SPEs) at room temperature, actively sought for quantum technologies. After decades of rapid advances, light sources have become high-performance, yet low-cost and reliable components. A new frontier of research is the development of non-classical light sources: sources that produce streams of photons with controllable quantum correlations. A central building block is a SPE — a fundamental resource for many scalable quantum information technologies. The ideal on-demand SPE emits exactly one photon at a time into a given spatiotemporal mode, and all photons are identical. The signature of an SPE is a characteristic dip in the second-order correlation function, $g_2(\tau)$, which correlates arrival times of photons that reach a detector. The simplest way to record $g_2(\tau)$ is to split the signal between two avalanche photodiodes and record coincidence counts. A dip below 0.5 at zero delay time, i.e., $g_2(0) < 0.5$, indicates that the emitter is an SPE. Such SPEs play a central role in quantum information processing, computing, and metrological applications [30]. Generally, SPEs in layered materials can be classified broadly into two types. The first is called a quantum dot (QD). The emission originates from a bound exciton that is confined to zero dimensions by a potential field generated by local strain and/or a crystallographic defect. The second type of SPE is a color center, an impurity or an isolated crystallographic point defect (a vacancy or an atom at an irregular point in the lattice) with electronic states that lie deep in the bandgap and possess the characteristics of an isolated artificial atom.

hBN resembles diamond in that it has a wide indirect bandgap of ~6 eV and hosts a broad range of SPEs with ZPL (an emission generated by an electronic transition that does not involve phonons) energies spanning the NIR-visible range (~1.6–2.2 eV) and the UV range (~4.1 eV) [31]. However, the atomic structure of these emitters is debated. The broad range of emission energies observed in samples suggests that a number of distinct defect structures or defect charge states are responsible for the observed SPEs. A number of atomic structures have been considered, with an emphasis on defect complexes composed of nitrogen and boron vacancies, and nitrogen, carbon, and oxygen impurities. However, all the assignments made to date are speculative, and more work is needed to determine the atomic structures of emitters in hBN. Apart from that, deterministic fabrication of emitters in predefined locations in a host is important for scalable engineering of nanophotonic devices and circuits. hBN

emitters are present in random locations of some as-grown samples. They can be generated by various postgrowth processing techniques that include annealing, irradiation by ions and electrons [32] or plasma processing [33]. However, in most of these studies, it is unclear whether new defects are produced by the postgrowth processing methods or activated via modification/restructuring of preexisting defects. Some studies report preferential occurrence of emitters at or near grain boundaries and flake edges, which is undesirable for device applications. However, this is not a universal characteristic, and emitters do also occur well away from edges and extended defects. In this work, the fluorescence emission properties of the grown hBN samples will be investigated in order to ascertain its performance to act as SPE sources.

1.3 Transition Metal Dichalcogenides: structure, properties and applications

Transition metal dichalcogenides (TMDCs) with the formula MX_2, where M is a transition metal (Mo, W, and so on) and X is a chalcogen (S, Se, or Te), have attracted much attention due to their layered structure and semiconducting properties. These 2D materials are in the form of XMX, where a plane of metal atoms is sandwiched between two planes of chalcogen atoms by covalent interaction, and different layers are held together by van der Waals interactions. The elements that can form TMDCs compounds are highlighted in Figure 3a.

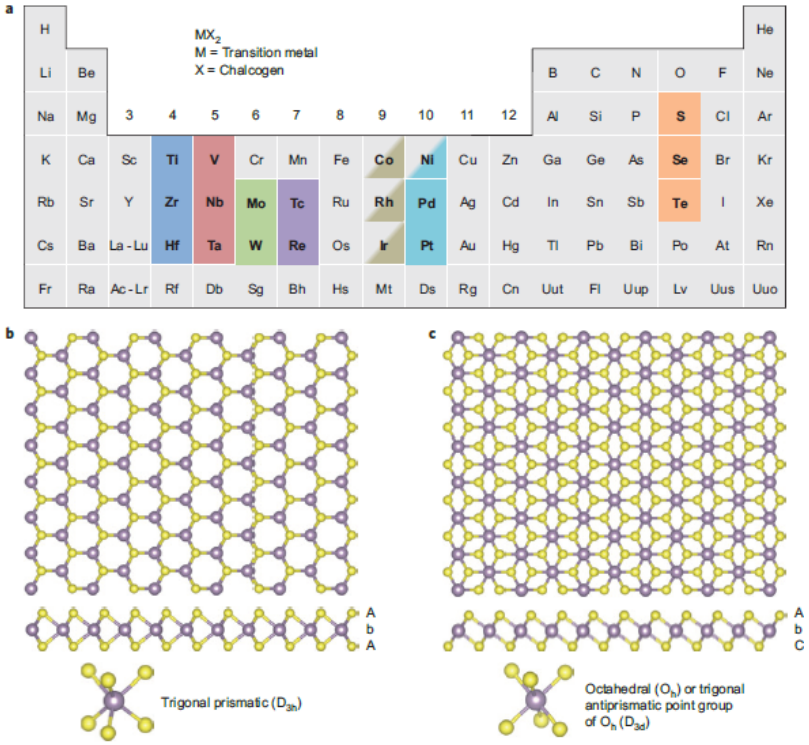

Figure 3. a) Periodic table highlighting the elements that make up the compounds from the TMDC family. b) and c) Single-layer TMDC with trigonal prismatic and octahedral, respectively. Taken from Ref. [11]

These compounds exhibit a rich chemistry due to the presence of lone-pair electrons of chalcogen atoms and the presence of d-orbitals of transition metal atoms [34]. The electron configuration of chalcogens in the valence shell is $ns^2p_x^1p_y^1p_z^2$, i.e. there are two electrons located on the atomic s-orbital, and two of the three p-orbitals possess unpaired electrons while the third one is occupied by a pair of electrons. The latter are usually called lone-pair (LP) electrons and usually do not participate in the formation of covalent bonds. The s-electrons are also chemically inactive in most cases. On the other hand, there is the presence of transition metals, alternatively called d-elements. A transition metal is an element whose atom has a partially filled d sub-shell, or which can give rise to cations with an incomplete d sub-shell'. These metal atoms provide four electrons to fill the bonding states of TMDCs such that the oxidation states of the metal (M) and chalcogen (X) atoms are +4 and –2, respectively. The lone-pair electrons of the chalcogen atoms terminate the surfaces of the layers, and the absence of dangling bonds renders those layers stable against reactions with environmental species. The metal coordination of layered TMDCs can be either trigonal prismatic or octahedral as illustrated in Figure 3b-c. The preferred phase adopted by TMDCs depends predominantly on the d-electron count of the transition metals, although a certain dependence on the relative size of the atoms plays a role. Group IVB metals all have octahedral structures. Most of group V metals also have octahedral structures, while some have trigonal prismatic structures; the reverse is true for the group 6 metals. In group 7 one finds again octahedral structures, although in this case they are distorted. Finally, group 10 TMDCs are all in octahedral structure.

As mentioned, TMDCs exhibit a layered structure with consecutive layers being bonded by van der Waals forces and ionic-covalent bonds as intra-layer bonds. The weaker forces at the inter-layer gap dictate the preferential cleaving direction for bulk TMDC crystals. Bulk TMDCs exhibit a wide variety of polymorphs and stacking polytypes because an individual MX_2 monolayer, which itself contains three layers of atoms (X–M–X), can be in either one of the two phases. Most commonly encountered polymorphs are 1T, 2H and 3R where the letters stand for trigonal, hexagonal and rhombohedral, respectively, and the digit indicates the number of X–M–X units in the unit cell (that is, the number of layers in the stacking sequence). The structural polymorphs are illustrated in Figure 4.

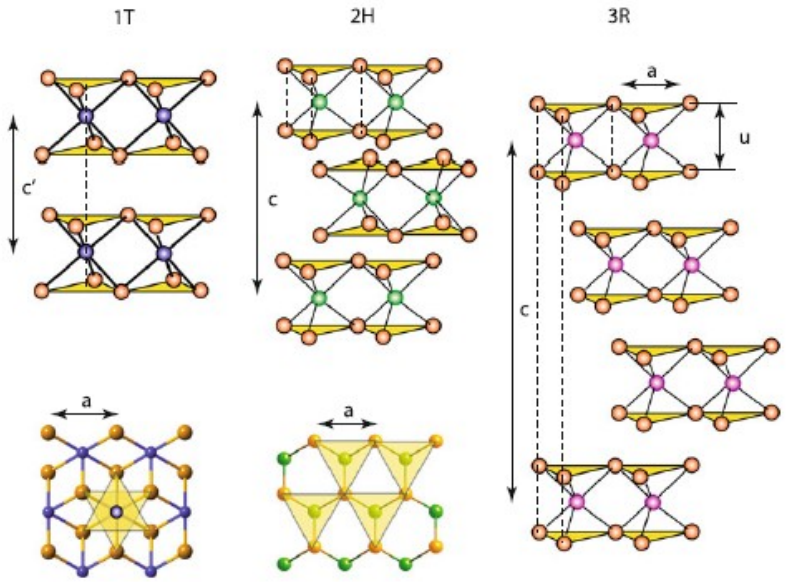

Figure 4. Schematics of the structural polytypes of TMDC from left to right: 1T, 2H and 3R. Taken from Ref. [10]

The properties of bulk TMDCs are diverse- ranging from insulators such as HfS_2, semiconductors such as MoS_2 and WS_2, semimetals such as WTe_2 and $TiSe_2$, to true metals such as NbS_2 and VSe_2. The electric behavior of each TMDC can be deduced by the DoS presented in Figure 5. When the orbitals are partially filled, as in the case of 2H-$NbSe_2$ and 1T-ReS_2, TMDs exhibit metallic conductivity. When the orbitals are fully occupied, such as in 1T-HfS_2, 2H-MoS_2 and 1T-PtS_2, the materials are semiconductors. The effect of chalcogen atoms on the electronic structure is minor compared with that of the metal atoms, but a trend can still be observed: the broadening of the d bands and corresponding decrease in bandgap with increasing atomic number of the chalcogen.

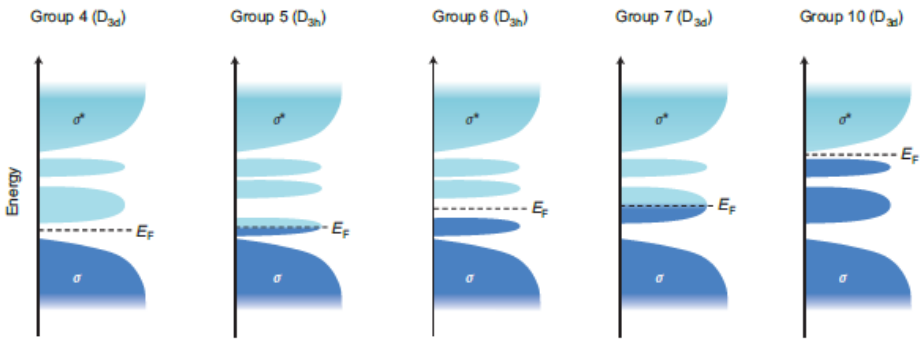

Figure 5. Schematic DoS for TMDCs from different groups of the Periodic Table. Taken from Ref. [11]

Nowadays there is a big excitement about low-dimensional TMDCs due to their superior properties. Their physical and chemical properties are highly dependent on their dimensionalities and size scale, and recently creatively exploring these properties has been extremely impactful. Atomic-scaled low-

dimensional (zero-, one-and two-dimensional) TMDCs nanostructures have been attracting much interest as strong candidates in various fields, including optoelectronics and photovoltaics. Among them, 2D TMDCs are particularly appealing and there has been an exponential explosion of reports spanning diverse research fields. Despite the great properties of 2D TMDCs, their low-dimensional counterparts such as zero-dimensional (0D) and one-dimensional (1D) structures are also highly attractive. 0D TMDs including the dot structures with the sizes of below 100 nm in all dimensions, such as TMDCs quantum dots (QDs), small nanoflakes, and nanoparticles, have been prepared and widely applied in the sensing field [35]. In addition, the unique 1D morphologies of TMDCs nanostructures, such as nanoribbon, nanotubes, and nanobelts are also presented with a range of great applications [36,37].

Among the TMDCs, $MoSe_2$ is considered as an important semiconductor with superior performance to the corresponding sulfide. $MoSe_2$ exhibits higher electrical conductivity due to the Se which brings its intrinsic metallic nature, higher optical absorbance, smaller band gap of 1.55 eV (1.9 eV in monolayer MoS_2), a ten-fold narrower line width and tunable excitonic charging effects. Few-layer $MoSe_2$ possesses tailorable attributes and designed functionalities due to layer-number-dependent optical and electrical properties, and the band gap varies from 1.55 eV in a monolayer to 1.1 eV in a bulk counterpart, which will be beneficial to high-efficiency photoelectronic and photovoltaic devices. Given the wide variety of properties, it comes as no surprise that $MoSe_2$ has a wide range of applications. It can be used to build field effect transistors showing high carrier mobility and high I_{ON}/I_{OFF} ratios (FETs) [38,39]. Besides that, the nature and narrower bandgap of $MoSe_2$ makes it more interesting for harvesting solar energy in single junction solar cells [40] or CIGS [41] by covering both the visible and IR parts of the solar spectrum. Not only are the optical properties of $MoSe_2$ interesting for solar cells, but they make it an interesting material to be used for photodetectors [42,43]. In addition to this, it is worth mention other interesting and promising applications outside the scope of this work, such as computer memory applications [44] and the possibility of incorporating these materials in the rising fields valleytronics [45] and polaritronics [46]. Besides that, in order to further expand the application fields of 2D TMDCs, various techniques have been exploited to modulate/enhance their physical properties, including doping [47], inducing defects [48] and strain engineering [49]. Among them, the latter is the most effective and straightforward strategy for tuning their lattice and electronic structure (and therefore modulate/enhance their physical properties) which broadens their applications in flexible nanoelectronics and optoelectronic devices [50]. In this regard, in the past few years many theoretical works have been devoted to the study of the role of strain on the physical properties of semiconducting 2D TMDCs, such as MoS_2 [51]. As an example, in aspect

of optical properties, strain can directly change the phonon structure and energy band structure of MoS_2, resulting in the shift of Raman and PL peaks [52].

As an example of a practical application, Fazio et al. demonstrated a polymer electrolyte gated CVD-based flexible photodetector (Figure 6) [53]. The device is assembled by stacking on a PET substrate CVD single layer graphene on top of a CVD-grown single layer of MoS_2. In this configuration, MoS_2 acts as visible light absorber, while graphene is the conductive channel for photocurrent flow. The device works for visible wavelengths with external responsivity up to 45.5 A/W, photoconductive gain ~4 × 105, operation voltage <1 V, and optical transparency >82%. Its responsivity, flexibility, transparency, and low operation voltage makes this photodetector attractive for wearable, biomedical, and low-power optoelectronic applications.

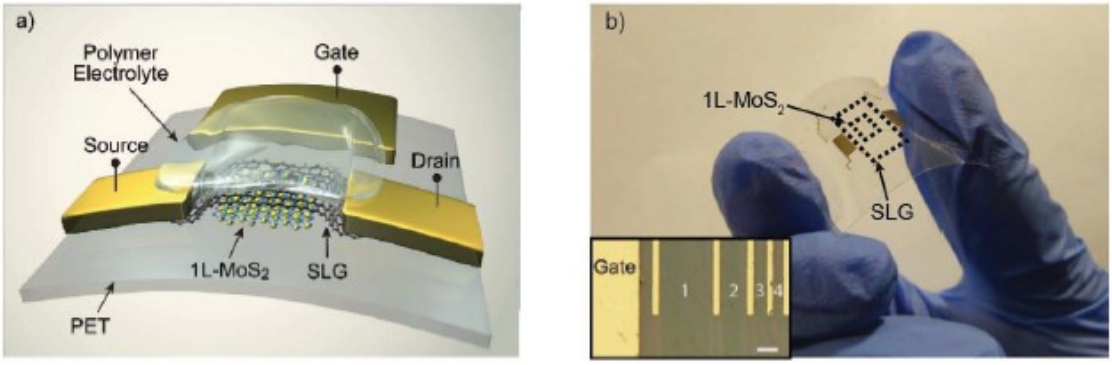

Figure 6. (a) Schematic SLG/MoS_2 flexible photodetector. (b) Picture of a typical photodetector, showing transparency and flexibility. (Inset) Optical image of 4 photodetectors with different channel lengths and common side gate electrode. Scale bar is 200 μm. Taken from Ref. [29]

The bright, narrow, single PL peak typical of single-layer $MoSe_2$ opens opportunities to use the material for optoelectronic applications. Besides, the PL emission (both intensity and position) can be tuned by strain engineering. Regarding $MoSe_2$, to date only a few reports explore how external strain may affect its physical properties [54–56]. Strain studies on CVD $MoSe_2$ flakes will be shown in the section 5.6 to ascertain the effect of external uniaxial strain on their optical properties aiming the hypothetical integration of this material in practical applications, such as the device shown in Figure 6 will be discussed

2. Production Methods

2D materials can be synthesized by either one of two radically different approaches: top-down or bottom-up. Top-down approaches yield 2D layers of material by taking the bulk materials and thinning them down to atomically-thin layers by taking advantage of the weaker van der Walls forces established inter layers. These include mainly mechanical and liquid phase exfoliation. On the other hand, bottom-up approaches are methods which grow or deposit the material layer by layer and thus allowing to control the thickness/number of layers of the material. They are methods such as chemical vapor deposition (CVD) and physical vapor deposition techniques (PVD). All these approaches are described In this chapter, with greater emphasis being put on the CVD process.

2.1 Mechanical Exfoliation

Mechanical exfoliation has been the first tool to provide high-quality 2D materials. This method is based on the adhesion of a layered crystal between two pieces of an adhesive tape, before peeling the tape apart to cleave the crystal. The adhesion between the tape and the basal plane of the crystal is significantly stronger than the weaker van der Waals forces between the layers, allowing isolation of increasingly thin flakes. Repeating this process on the freshly peeled flakes has been found to produce single- and few-layer nanosheets that can be transferred onto a substrate for further characterization and device fabrication. To date, mechanical exfoliation is the most efficient way to produce the cleanest, crystalline, and atomically thin nanosheets of layered materials. This method, also known as the Scotch tape method, has been widely used to exfoliate bulk hBN. As a result, BNNS with large lateral size and relatively free of contamination (aside from the tape adhesive which can be removed by a thermal anneal) are reported [57]. Furthermore, this technique is currently one of the most efficient ways to obtain atomically thin TMDC layers. However, isolating large areas of atomically thin TMDCs crystals still remains a challenging task. To turn the exfoliation easier, it was proposed to start using other substrates taking advantage of chemically enhanced adhesion. As an example, the usage of chemical affinity of S, Se or Te atoms, that can bind to a gold surface more strongly that to neighboring layers, was reported to exfoliate single layers of several TMDCs such as MoS_2, WSe_2 and Bi_2Te_2 with lateral sizes of several hundreds of microns [58]. After exfoliation, these thin crystals can be used for several applications since their high quality, as it is reported for $MoSe_2$ [39].One of the most remarkable strengths of this method is the possibility of the construction of van der Waals heterostructures where 2D sheets are stacked in a specified layered order. Additionally, this method keep unchanged the intrinsic properties of the 2D materials that are mostly

observed on exfoliated flakes but are either inaccessible or suppressed in samples prepared by other methods. Despite the improvements done in this technique, it is still very limited in yield, lateral size and contamination.

2.2 Liquid Phase Exfoliation

Liquid phase exfoliation (LPE) is considered to be one of the most promising and simplest routes for the production of 2D materials on a large scale. The most commonly used liquid exfoliation technique is based on ultra-sonication, where the layered materials are exfoliated by microjets and shock waves generated by the collapse of the liquid (due to the formation of cavitation-induced microbubbles). Alternatively, a high-shear tool can also be used for the exfoliation of several 2D materials. In this case, the exfoliation mechanism is mainly dependent on high shear force with aid of collision and cavitation. Besides that, there are other less recurrent approaches of LPE based on high shear force, such as ball milling and micro fluidization. The general LPE experimental procedure can be described as follows: the bulk layered material, typically in powder form, is first added to either a pure solvent or dispersant-containing solution, followed by an exfoliation step performed by applying ultrasonic and/or shear force. It is required that the resulting exfoliated nanosheets are stabilized to avoid re-aggregation after sonication. Then the exfoliated thin nanosheets are separated from the un- or incompletely exfoliated thick layered materials typically using centrifugation or natural sedimentation over time by gravitational force. Finally, the supernatant, containing well-dispersed and thin nanosheets, is collected. The LPE method has been extensively investigated for the successful exfoliation of hBN. A wide selection of exfoliation solvents are reported, including organic solvents (isopropanol [59], 1,2- dichloroethane [60], N,N-dimethylformamide (DMF) [61]), protonic acid (phosphoric acid [62], methanesulfonic acid [63]) and surfactants [64], etc. The diversity of exfoliation solvents also provides great convenience for the subsequent application of the obtained solution. Moreover, hBN nanosheets were directly exfoliated in pure water (without the use of any surfactants or organic solvents) by cutting the pristine hBN with the assistance of bath sonication. The solvent polarity effect in combination with sonication can lead to complete exfoliation of hBN into mono- or few-layers, forming ‘‘clean’’ aqueous dispersions of hBN nanosheets. However, the hBN flakes thus obtained are of reduced lateral sizes, because of the sonication-assisted hydrolysis. With the introduction of a suitable ionic surfactant (sodium cholate), a relatively high yield of hBN crystals with excellent dispersibility was successfully exfoliated in water medium, where pyrene derivatives are used as stabilizers. Likewise, liquid exfoliation by direct ultrasonication was also employed to fabricate single-layer and multilayer nanosheets of a number of layered TMDCs [65], such as MoS_2, WS_2, $MoSe_2$ and others,

where the authors initially sonicated commercial powders in a number of solvents with varying surface tensions. Successful solvents were those with dispersive, polar, and H-bonding components of the cohesive energy density within certain well-defined ranges. Again, exfoliation can be performed in water, followed by ultrasonication in an aqueous solution of sodium cholate, a surfactant that prevents their re-aggregation. Ion-intercalation, such as lithium intercalation, is another liquid phase exfoliation method used to obtain TMDCs monolayer. The bulk material in powder form is submerged in a solution containing the lithium ionic species (such as n-butyllithium) for a period of days, allowing the lithium to intercalate. The intercalated material is then submerged into water – the water will react with the lithium, between the layers, which will result in the formation of H_2 gas, separating the layers. This method yields monolayers nanosheets with lateral size in the sub-micron. This method has been demonstrated for several TMDCs, including $MoSe_2$ [66].

Despite all the interesting pros, LPE technique involves some drawbacks. This method requires long-term ultrasonic treatment, which not only consumes a large amount of energy but also easily causes the temperature to rise, then inducing organic solvents into volatilizing. Also, the choice of solvent is not always obvious, and it should have surface energies comparable to those of the exfoliated crystals. The main challenges of this method are the increase in the monolayer yields and avoid reduction in the lateral size of the nanosheets.

2.3 Physical Vapor Deposition

Physical vapor deposition (PVD) is a bottom-up synthesis process, where materials are vaporized from a solid or liquid source in the form of atoms or molecules and are transported towards a substrate under UHV (ultra-high vacuum) or a low-pressure gas (plasma) environment for deposition. The vapor from the source materials is normally generated by two techniques: thermal evaporation or sputtering. In the thermal evaporation process, the source material is heated up. Required heating could be achieved by various methods including hot filament, electrical resistance or electric arc. Molecular beam epitaxy (MBE), an advanced form of thermal evaporation where molecular beams are produced by evaporation/sublimation of suitable materials contained in ultrapure crucibles, has attracted extensive attentions in recent years because it can control chemical composition and doping concentration precisely and have low temperature process. The term epitaxy (or epitaxial growth) suits for the growth of a single crystal film on top of a crystalline substrate, matching its lattice. The deposited layers have the same crystalline structure of the substrate or a structure with similar symmetry and a lattice parameter that differs no more than ~10% from that of the substrate. Instead, Sputtering techniques utilize an electrically

excited gas plasma (typically Ar^+) in a vacuum system. The ions in the plasma are accelerated toward the cathode, which upon bombardment eject neutral atoms from the cathode surface. The ejected atoms collect on all surfaces including the substrate surface. Among sputtering techniques there are a lot of configurations, and it may depend on the material wanted to grow.

PVD processes have been used to study the growth of 2D materials, including both hBN and $MoSe_2$. Actually, ion beam sputtering (with Ar^+) of a pure h-BN target has been employed to grow mono- to few-layer hBN on Cu and Ni substrates [67]. The same result was achieved by employing radio frequency (RF) magnetron sputtering of a B target in an ultrahigh-vacuum N_2/Ar atmosphere. The N supply is given by the atmosphere instead of being present in the physic target. The use of Ru(0001) substrate was crucial since it offers an orientation for B and N species to assemble into an ordered hBN layered film [68]. Besides that, growth of hBN is also possible by using MBE. The hBN monolayer coverage can be reproducible controlled by tuning growth temperature, time and B:N flux ratios using plasma-assisted MBE [68]. However, the progress in this technique has been relatively slow, partly due to a lack of an efficient MBE source for boron, due to its very low vapor pressure. In the context of PVD techniques for the growth of TMDCs, the biggest challenges lies in the control of the stoichiometry, due to the very high vapor pressure of the chalcogenide species with respect to the metal. There are many applied growth strategies to grow 2D TMDC layers by sputtering method. The most common and easiest one is the direct sputtering from TMDCs targets of MoS_2 [71] or $MoSe_2$ [72], using a magnetron sputtering system. MBE is also been used to grow many materials of belonging to the TMDCs family such as MoS_2 [73] or WSe_2 [74]. The molecular-beam epitaxy growth of ML and sub-ML $MoSe_2$ was reported somewhere else [75]. For growth an overpressure of Se of more than ten times that of Mo has been used throughout this experiment to guarantee thermal equilibrium considerations but also because of the kinetics of high rate Se desorption from the surface.

In general, PVD constitutes a family of synthesis processes with inherent qualities enabling large-scale and thickness controlled 2D films. However, they generally require UHV conditions and well-calibrated, high-purity atomic sources which increases the costs and also the complexity of the technique which turns it unsuitable for industrial purposes.

Table 1- PVD techniques. Taken from Ref. [76]

Sputtering		**Evaporation**	
Ions Beam		E-Beam	
Diode		Inductive	
Triode		Resistive	
Reactive Sputter Deposition		Arc	Stirred Random Cathodic Arc Deposition
Magnetron	RF- Radio Frequency DC- Direct Current MEP - Magnetically Enhanced Plasma UBMS - Unbalanced Magnetron Sputtering DMS – Dual Magnetron Sputtering HiPIMS/ HPPMS - High-Power Impulse/ Pulse Magnetron Sputtering		

2.4 Chemical Vapor Deposition

Chemical vapor deposition (CVD) is a process serving to deposit a solid material from a vapor phase by specific chemical reactions occurring on or in the vicinity of a substrate surface kept at a required temperature. A CVD system must meet several basic requirements: i) precise delivery of the gas-phase reactants; ii) a sealed reaction chamber; iii) evacuation of the gases and control of the reaction pressure; iv) supply of the energy source for the chemical reactions; v) treatment of the exhaust gases to obtain safe and harmless levels. In order to meet these basic requirements, a typical CVD system consists of a gas delivery system, a reaction chamber, a vacuum system, an energy system, an exhaust gas treatment system, and a control system. There are several different CVD systems, ranging from simple and cheap setups to complex and costly ones. Regardless of the variations in CVD types, the fundamental process is similar and consists of the following elementary steps (Figure 7). First, the reactant gases are carried into the reaction chamber. These reactant gases then either undergo gas-phase reactions to form intermediate reactants and gaseous by-products via homogeneous reactions or diffuse directly through the boundary layer to the substrate. In both cases, the reactant gases and the intermediate reactants adsorb onto the heated substrate surface and diffuse on the surface. The subsequent heterogeneous reactions at the gas–solid interface lead to material formation via nucleation, growth and coalescence as well as formation of reaction by-products. Finally, any gaseous products and unreacted species desorb from the surface and are carried away from the reaction zone. The gas-phase reactions occur when the temperature is sufficiently high or additional energy is introduced (for example, in the form of plasma). In addition, the heterogeneous reaction is essential if the deposition reaction relies on the surface catalysis of the underlying substrate, such as in the case of the catalytic growth of graphene on a metal surface [77].

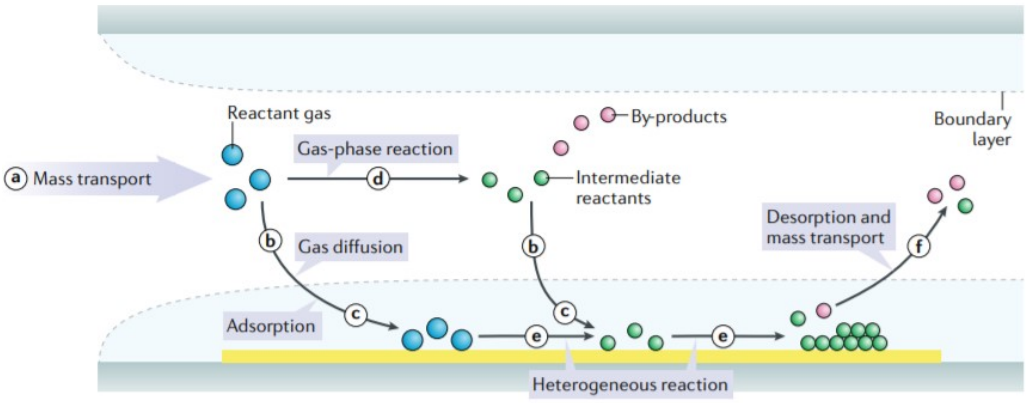

Figure 7. Schematic of general elementary steps of a typical CVD process. Taken from Ref. [79]

The CVD process is rather complex due to the several parameters involved and their interrelation. In order to achieve the ideal growth, it is crucial to understand the general mechanisms behind CVD growth, i.e., how parameters such as the precursor, substrate, pressure, and temperature affect mass and heat transport, interface reactions, and consequently the growth of the materials [78]. Figure 8 illustrates the parameters involved and how they are related, affecting the growth.

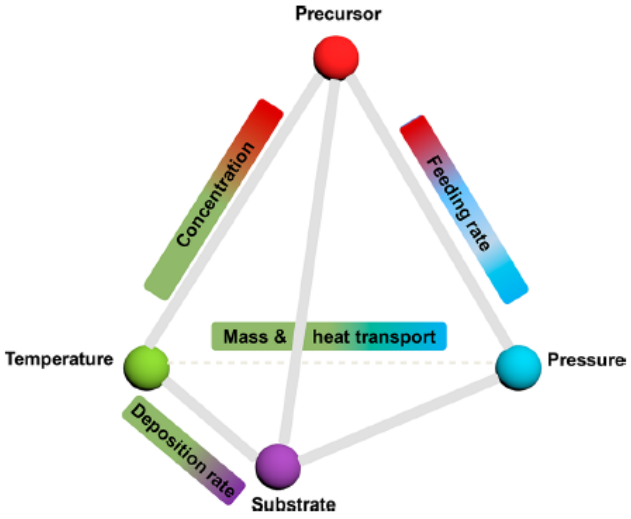

Figure 8. Schematic showing how various parameters including precursor, temperature, pressure, and substrate affect the thermodynamics and kinetics in the CVD growth of 2D materials. Taken from Ref. [80]

Regarding the preparation of 2D compound materials, CVD is one of the promising methods because it can grow a series of 2D compound materials with high quality as well as reasonable cost. The physical properties of 2D materials are closely related to their structures, including size, number of layers, morphologies, orientations, phases, doping, defects, grain boundaries, among others. As an example, the electronic structure and further performance of 2D material based electronic and optoelectronic devices is highly dependent on the number of layers, the phases and any doping. Additionally, crucial phenomena

for device performance like charge mobility and interface scattering are heavily dependent defect concentration or gain boundaries. For practical applications, large area high quality continuous 2D crystals with uniform properties are pre-requisites. This fact calls for a deep understanding of the material growth mechanism for preparing 2D materials which is yet very challenging. That is why despite its early success, CVD method still remains a challenge due to the enormously diverse results from different precursors, evaporation and reaction temperatures, ramp rates, reaction time, flow rates and components of carrying gases, seeding and patterning, morphology and pretreatment of substrates, and the pressure in the growth, to name a few.

Thus, CVD is one of the promising methods because it can grow a series of 2D compound materials with high quality as well as reasonable cost. Besides that, in contrast to PVD methods, such as evaporation and sputtering, CVD offers a clear advantage by relying on chemical reactions that enable tunable deposition rates as well as high-quality products with excellent conformality. However, due to the complicated growth mechanism like sublimation and diffusion processes of multiple precursors, maintaining the controllability, repeatability, and high quality of CVD-grown compound materials is still a big challenge, which prevents their widespread use.

2.4.1 CVD of hBN

Several CVD precursors were proposed to grow hBN thin films: gaseous (e.g., boron trifluoride, boron trichloride, diborane and ammonia) [79], liquid (e.g., borazine, molten Fe82B12 alloy) [80,81], and solid (e.g., ammonia borane – AB) [82]. Borazine is one of the most common precursor, due to its high vapor pressure. However, this compound is toxic, highly flammable, and difficult to store, thus presenting obvious safety concerns. One of the borazine derivatives, b-trichloroborazine, has also been used. The major drawback of this precursor is the release of HCl gas when it is exposed to humid air, which is corrosive to the CVD fittings and equipment. Moreover, hBN thin films can be grown from mixtures of diborane and ammonia, but diborane is also toxic and pyrophoric. By contrast, AB is a non-hazardous and inexpensive compound which makes it very appealing for hBN growth. However, AB decomposition under CVD conditions is complex and hence has hindered tailored hBN production and its exploitation. Time and temperature-dependent studies have been reported for AB decomposition to understand the release of a N_xB_y species and, as a result, significant changes of the N:B ratio during hBN synthesis [83]. Sometimes there are solid decomposition products that are transported to the growth zone by the carrier gas and this can be prevented by decomposing AB in a separated zone (sitting outside the furnace) fitted with a valve or by using filters, which retain those unwanted products [84,85].

The morphology of the substrate is of the utmost importance for the hBN growth, which is a surface-mediated growth process. Regarding the catalytic substrates, several metals (i.e., Ru, Ni, Rh, Pt and Cu) were tested, each one with distinct parameters such as composition, lattice symmetry and constant, and electronic structure. High binding energy and good lattice match are usually preferable in a CVD substrate. The price of the substrates is also relevant, de-facto excluding the choice of metals as Rh and Pt for industrial production, as an example. Ni and Cu have relatively high binding energies and a lattice mismatch with hBN of 0.4% and 0.9%, respectively: These features and a reasonable cost, which make them the most suitable substrates for hBN growth. These catalytic substrates are bought commercially in the form of foils. These as-received foils normally require chemical treatment prior to material growth to remove the oxide layer and organic contaminants. Acetone and isopropyl alcohol (IPA) are used to remove any organic contamination. Besides that, pre-treatments including acetic acid or dilute nitric acid are widely used to remove the oxidized layer and contaminants. Additional treatments such electrochemical polishing and long term annealing are usually reported for Cu foil substrates [86,87]. On the polycrystalline Cu substrates, the presence of grain boundaries and other defects often lower the lateral size and homogeneity of the BN nanosheet. Electropolishing can help smoothening and minimizing defects on the substrate. Long annealing of the Cu substrate at high temperatures can facilitate the growth of single crystal BNNS with large lateral sizes.

Pressure is one of the most important parameters for the hBN growth since it directly influences its structure and morphology. In general, an atmospheric pressure setup utilizes fewer resources, has a lower operating cost, and is generally simpler in design when compared to a low-pressure setup. Uniform planar thin hBN grows under LPCVD conditions whereas medium pressure and APCVD growth conditions afford thicker and less crystalline films (due to the faster growth rate). High-quality hBN samples are commonly grown by low-pressure LPCVD. In this case, the growth is preferentially surface-reaction-limited and thus less affected by the substrate geometry or the gas flow conditions. Kim et al. reported the growth of large-area, monolayer hBN on Cu foil at 350 mTorr [85]. By further lowering the pressure (10mTorr), Ismach et al. grew hBN films (a few to 50 layer thick), implementing a sequential growth with ammonia and diborane precursors [88]. Wang et al. reported the epitaxial growth of single-crystal, monolayer hBN on 100-cm^2 Cu (110) surface, by annealing and reconstructing an industrial copper foil [89]. To date, a handful of groups attempted to grow hBN by atmospheric pressure chemical vapor deposition (APCVD). Tay et al reported the growth of ~35 μm crystalline monolayer h-BN hexagons using an electro-polished Cu substrate under APCVD (growth was carried at 1050°C for 10-30min using AB as precursor). They concluded that the nucleation density and domain sizes are highly dependent on the surface morphology

and oxygen content of the Cu substrate[86]. Song et al reported the synthesis of μm-scale h-BN films consisting of two to five atomic layers using AB as precursor (heated up to 120-130 °C, in order to turn it more volatile). During the growth process, which took 30-60 min, Ar/H_2 flow was kept as 200 sccm [90]. Furthermore, a systematic study conducted by Tay et al. allowed the controllable growth of hBN on a Cu substrate while using AB as the precursor. Several CVD parameters such as substrate position; AB weight and pre-processing temperature; growth temperature and duration were investigated. In their experiments, 2/3-layer hBN crystals as well as ~2-nm-thick films were grown [91]. In a similar study, Song et al presented a comprehensive investigation on the growth thermokinetics of hBN using solid AB as precursor. Again, substrate dependence, flow rate of carrier gas, heating temperature of ammonia borane, growth temperature and time were studied in detail. With the optimized growth condition monocrystalline domains as large as 80 μm^2 and polycrystalline ultrathin film were achieved. [92].

Any CVD process entails several optimization steps to achieve the ideal conditions for the growth. Critical parameters such as growth temperature, deposition time, substrate position and carrier gases have been systematically investigated in order to understand their influence on the growth of the h-BN domain/films. Stehle et al. investigated the growth stages of the hBN single crystals, by varying critical parameters [93]. The experiments took place under APCVD conditions, and the setup used is illustrated in Figure 9a. As shown in Figure 9b, the morphology of single domains deposited at 1065°C slowly changes from triangular to truncate triangular, and finally to pseudo hexagonal shape as the substrate position moves away from CVD tube inlet. The changes occur because of misbalance between boron and nitrogen throughout the tube. This changes in crystal shape are normal in APCVD because there is a non-uniform density distribution of the precursor in the chamber in contrast to the perfect triangles usually grown by LPCVD. Changing the buffer gas from argon to nitrogen led to exclusively triangular shapes of hBN crystals throughout whole length of the CVD tube (Figure 9c). This drastic difference in the hBN crystal shape as compared to the growth in argon atmosphere can be explained by an additional source of active nitrogen. Besides that, lowering the growth temperature (deposition at 1000 °C with Ar buffer gas) results in exclusively triangular shaped crystals but smaller when compared to the ones grown at 1065°C (Figure 9d). In general, hBN growth at higher temperatures results in larger crystal sizes similar to what was observed for graphene synthesis in the past.

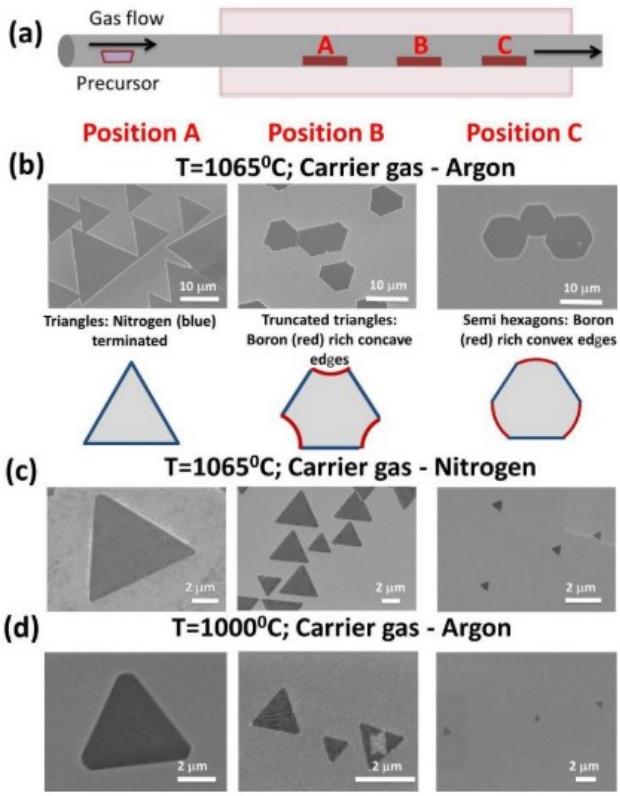

Figure 9. a) APCVD experimental set up for hBN growth. SEM images of the hBN domains grown: (b) at 1065 °C using Ar, (c) at 1065 °C using N_2 and (d) at 1000 °C and using Ar. A sketch of the resulting hBN crystal shapes and corresponding termination is provided. Taken from Ref. [92]

Tay et al. studied the effect of growth time [91]. The domain sizes and coverage can also be controlled by varying the deposition time. Figure 10a–d shows the increase in size and film coverage of h-BN on region C3 at 5, 10, 30 and 60 min, respectively. However, the film became continuous on D3 when the precursor was heated beyond 30 min. Figure 10e-f show the progression of coverage with an increasing number of layers of film on region D3 at 30 and 60 min, respectively, which proves that the growth of h-BN films on Cu substrates is not self-limited. After a long growth time, the film grows in thickness, this could possibly be because the growth mode follows the combination of a layer-by-layer growth and island growth (Stranski–Krastanov growth). A transition from layer-by-layer growth to island growth occurs at a critical thickness, depending on the chemical and physical properties of the substrate and of the film, such as surface energies and lattice parameters. Figures 10g-h illustrate how film coverage and thickness depend on the growth time. Apart from this, other parameters such as precursor weight or carrier gas flow may be optimized during the process to obtain an ideal hBN growth.

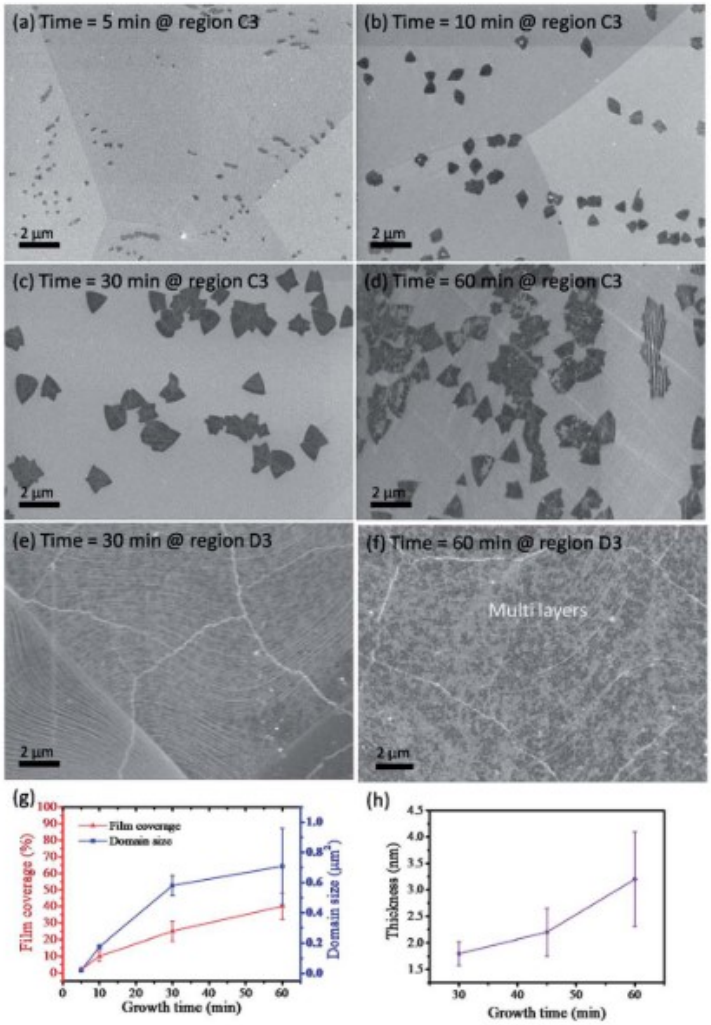

Figure 10. SEM images of the grown hBN with a growth time of (a) 5 min, (b) 10 min, (c) 30 min, (d) 60 min at region C3, and of (e) 30 min and (f) 60 min at region D3. (g) Plots of film coverage and domain size vs. growth time and (h) a plot of thickness vs. growth time. Taken from Ref. [90]

2.4.2 CVD of $MoSe_2$

I. Basic routes

$MoSe_2$ – as several 2D TMDCs – can be grown by CVD on Si/SiO_2 substrates using a two-powder approach. The process is based on the evaporation of the two volatile solid precursors, typically Se and MoO_3 or MoO_2, typically held in two distinct zones of a quartz-tube furnace and brought to the desired temperature to allow their controlled evaporation. Transported by carrier gases (*i.e.*, Ar/N_2, often mixed with a low concentration of H_2), the vaporized precursors react in the gas phase and condense on the substrate (kept at a specific temperature). This two-powder approach can potentially give rise to both single-crystal flakes or films. Shaw et al. reported the growth of highly crystalline single- and multi-layer $MoSe_2$ flakes with edges around 30μm under ambient pressure [94]. Under these atmospheric pressure

conditions, single-crystal growth is very susceptible to the CVD parameters used. Actually, by varying the vertical distance between substrate and precursor it is feasible to control single crystal morphology allowing to obtain 2D triangles, hexagons, 3D pyramids or vertically sheets [95]. Apart from this, hydrogen is known to have a critical role in the growth: it etches multilayer cores and promotes selenization process, as reported [61]. Besides that, it is also possible to have control over crystal shape through variation of the H_2 content in the gas flow mix, as illustrated in Figure 11. When H_2 content was set to 49 Ar/1 H_2, only white rhomboidal-shaped nanosheets covered the substrate (Figure 11a). As H_2 content was gradually increased, the color of the rhomboidal nanosheet transformed into violet (Figure 8b). With increased H_2 content, the $MoSe_2$ domain shape transformed from hexagonal shapes into a truncated triangle, and finally into a sharp-edged triangle (Figure 11c–e). By further increasing H_2 content, the $MoSe_2$ film morphology-maintained triangle shape but with decreasing size (Figure 11f–h) [96].

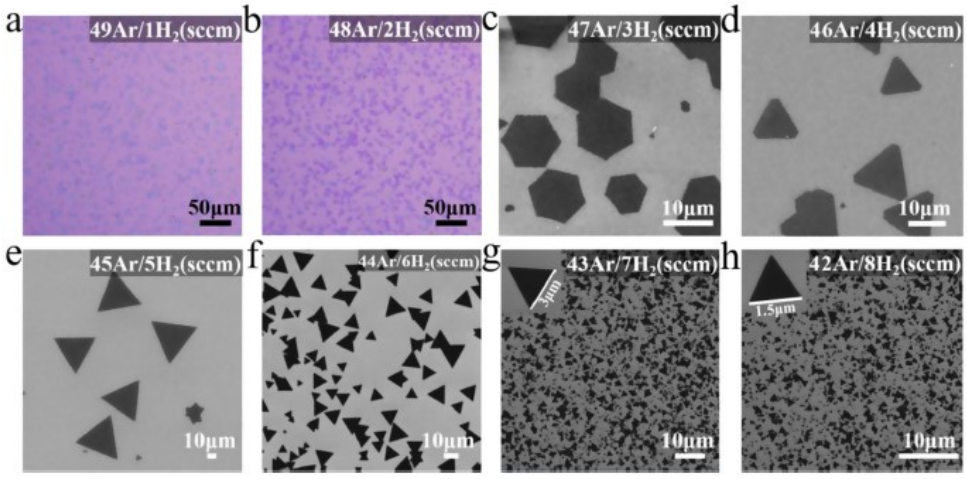

Figure 11. a)-b) Optical microscopy images of $MoSe_2$ morphology under low H_2 content. c)–h) SEM images of the $MoSe_2$ flakes in an increasing H_2 gradient. Taken from Ref. [96]

Besides single-crystal domains, the growth of large-area films with this approach has been reported. Wang et al. have synthesized highly crystalline continuous μm-scale films with controlled nucleation density via reverse-flow CVD using the setup shown in Figure 12 (growth was carried at ~760°C with 80 sccm Ar/5 sccm H_2 flow for 10 min). This method prevents the unintended supply of the chemical vapor and thus allowing controlled nucleation, without the assistance of any catalyst or promoter [97]. Still on μm-scale, Campbell *et al.* showed continuous monolayer $MoSe_2$ film on Si/SiO_2 areas up to a few hundred μm^2, grown at 800°C with Ar/H_2 22.5/2.5 sccm for 40 min [98]. Zhao *et al.* reported a polycrystalline monolayer $MoSe_2$ film on a millimeter-scale area through atmospheric pressure CVD (Ar/H_2 flow rates 1500/150 sccm at 750°C) [99]. Chen et al. reported the growth of highly crystalline centimeter-scale monolayer, bilayer and few-layer $MoSe_2$ films by H_2-assisted APCVD grown at 730-760°C [100]. By

switching to low-pressure (20 Torr), Lu *et al.* reported H_2-assisted CVD growth at 800°C on Si/SiO_2 substrates (up to a size of 1 cm^2) via selenization of MoO_3. The authors produced mono- to few-layer, polycrystalline $MoSe_2$ films, with grain lateral sizes up to few hundreds nm [101]. Gong *et al.* hold the record for $MoSe_2$ single crystal sizes, reporting mm-sized domains as well as being able to grow 2x2 cm^2 polycrystalline films. The average reported grain size is ~1.5 mm, with grains showing no preferential orientation on the substrate, and secondary growth taking place in some regions of the substrate.

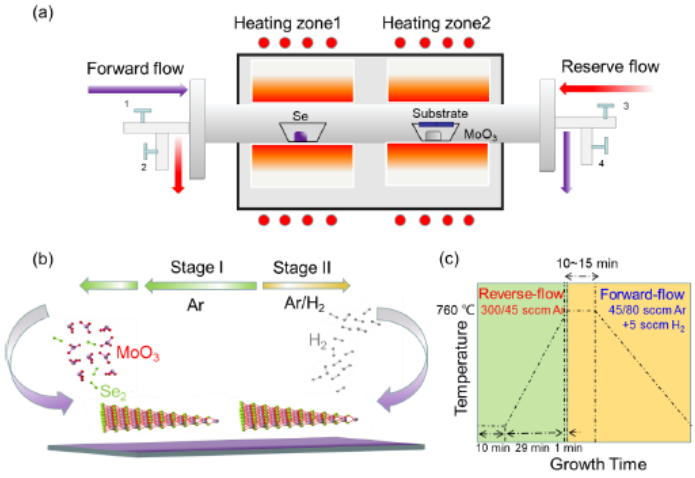

Figure 12. (a)-(b) Schematic illustration of the reverse-flow chemical vapor deposition process. (c) The diagram of the growth time and temperature. Taken from Ref. [97]

Related to CVD technique, there is another route that is suitable for the growth of TMDCS. This technique is based on the vapor phase reaction of transition metal oxides with chalcogen precursors. This process has been reported for several TMDCs composites such as $MoSe_2$[102], MoS_2[103], WTe_2[104] or $MoTe_2$[105]. In case of $MoSe_2$, a metallic foil (Mo) is placed inside a furnace chamber together with a chalcogen precursor (Se) in powder form. The precursor zone is heated to its evaporation point or higher, leading to the transition to vapor phase. The vapor phase precursor will then be carried to the metal foil by using a carrier gas flow (an inert gas, such as Ar), where it reacts with the native oxide layer of the foil. The thickness of the obtained TMDC layer is usually in the order of the tens of micrometres, as it depends on the thickness of native oxide layer in the metallic foil. This method is good for scalability however weak control over the thickness of the resulting film. By using the Mo foil as Mo precursor, the amount of MoO_x available for reaction is that of the native oxide layer of the metal – which makes the initial conditions unknown, unless a controlled annealing or deliberate of oxidation is done.

II. Novel Routes

Na has been reported as a catalyst for the growth of $MoSe_2$. It has been shown that Na increases the growth rate of several TMDCs, including $MoSe_2$. To achieve this effect, NaCl can usually either mixed with

the metal powder precursor, or soda-lime glass (SLG) can be used as growth substrate due to the presence of Na in its composition. Despite its efficiency, the exact mechanism that allows for Na to be beneficial for the growth of TMDCs has not yet been uncovered, with authors providing different hypotheses. Li et al. reported the growth of sub-millimeter size single-crystal $MoSe_2$ monolayers by NaCl assisted CVD. The procedure was employed at 30Torr and the NaCl powder was mixed with MoO_3 powder, normally used in the two-powder method (growth took place at 750°C for 15min under Ar/H_2 flow rates of 50/10sccm) [106]. Following the same thinking, Yan et al. reported the APCVD growth of MoSe2 films by NaCl assisted CVD (grown at 800°C for 15min under 40 sccm Ar flow). Remarkably, they did it without the assistance of hydrogen, which is systematically used in the two-powder approach. This work successfully synthesized large area monolayer, bilayer, and few-layer $MoSe_2$ continuous films on SiO_2/Si substrates. The $MoSe_2$ film is several centimeters in size and the size of the monolayer $MoSe_2$ reaches ~3 mm [107]. Wang et al. have also utilized Na-containing powders mixed with the precursor to enhance the $MoSe_2$ growth. In their case, they showed that in addition to NaCl, NaBr can also be used. In their work they showed that the $MoSe_2$ domains grown without the aid of Na kept a regular triangular shape; in contrast, the ones that did exhibited a fractal or dendritic structure. The results have demonstrated that the addition of sodium salts in the CVD growth of $MoSe_2$ promotes the formation of liquid Na-Mo-O droplets that induces the ultrafast nucleation and growth of $MoSe_2$ [108].

Apart from powder supply, it is possible to use substrates with the desire salts in their composition. Chen et al. reported the fast growth of millimeter-size monolayer $MoSe_2$ crystals on molten glass under ambient pressure conditions. Ar was used as carrier gas, and a small amount of H_2 was used to control the start and end point of the reaction. The temperatures of selenium powders and molten glass during growth were kept at 280 and 1050 °C, respectively. The experimental setup and results are illustrated in Figure 13. The authors claim that the advantage of molten glass is the generation of a low-defect, highly homogeneous template with low nucleation density [109].

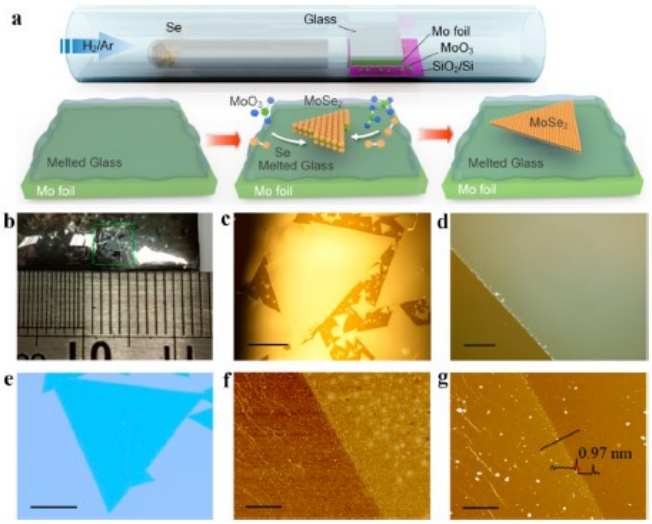

Figure 13. a) Scheme showing the CVD process. b) Photograph of the grown $MoSe_2$ crystals. c)-d) Optical images of grown $MoSe_2$ crystals. e) Optical image of the $MoSe_2$ crystals transferred onto a Si/SiO_2 substrate.f)-g) AFM images of the $MoSe_2$ crystals. Taken from Ref. [109]

3. CHARACTERIZATION TECHNIQUES

In this chapter the techniques used for characterization of the resulting materials are described. Through material characterization it will be possible to relate the CVD growth conditions with the resulting properties of the samples. Characterization techniques will serve to ascertain structural, optical, and chemical properties of the CVD grown materials. As for the characterization, a wide range of techniques were used, including optical microscopy, Raman spectroscopy, atomic-force microscopy, scanning-electron microscopy, X-ray photoelectron spectroscopy, energy dispersive X-ray spectroscopy, and transmission electron microscopy. Table 2 summarizes the crucial signatures about each technique employed.

Table 2- Characterization tools and their settings for assessing 2D materials.

Assessment tool	Spatial resolution	Property	Advantages	Disadvantages	Considerations
Optical microscopy	Micrometres or less	Individual domain shapes; surface coverage; number of layers; grain boundaries; defects (wrinkles and folds)	Simple to operate; large-area characterization; non-destructive to the sample	Low resolution; usually needs a suitable substrate	Clearer images when choosing a suitable wavelength of light or adding an optical filter
Scanning electron microscopy	Approximately nanometres	Individual domain shapes; surface coverage; number of layers; grain boundaries; defects (wrinkles and folds)	Simple to operate; large-area characterization; high resolution; good environmental adaptability	Damages the graphene atomic lattice	Based on electron scattering; electron beam energy ranges from a few 100 eV to a few keV
Atomic force microscopy	Nanometres or less	Individual domain shapes; surface coverage; roughness; grain boundaries; number of layers	High resolution; good environmental adaptability	Scanned area is small; scanning speed is slow; unsuitable for samples with significant surface topography	Sample surface must be clean; pollutants contaminate the tip and can result in virtual and/or false images
Transmission electron microscopy	Ångstroms or less	Atomic structures (point defects, grain boundaries); crystal orientation; purity	Atomic resolution; can obtain cross-section geometry	As-grown graphene must be transferred to a suitable substrate	High-energy electron beam (several 10 keV to few 100 keV) can induce defects
Raman spectroscopy	~100 nm (diffraction limit)	Number of layers; defects; strain; doping	Simple to operate; high sensitivity; spatially resolved distribution easily obtained by mapping the sample	Qualitative only	SiO_2 is the most frequently used substrate
X-ray photoelectron spectroscopy	100 μm	Purity	Surface-sensitive technique to analyse elemental composition and chemical state	Low spatial resolution; no accurate quantification	Detecting depth ranges from 1 to 10 nm

3.1 Optical microscopy

Optical microscopes are the oldest design of microscope and were possibly invented back in the 17th century. The optical microscope (OM), also referred to as a light microscope, is a type of microscope that uses visible light and a system of lenses to generate magnified images of small specimens. The image magnified by the system can be observed directly be eye or acquired by electronic detectors such as CCD or CMOS detectors. Basic optical microscopes can be very simple, although many complex designs aim to improve resolution and sample contrast. Optical microscopy is a simple and quick tool to examine 2D materials whether in form of films or single crystal flakes. In case of CVD grown films, optical microscope

can give a feeling about thickness, uniformity and relative contamination. As an example, optical microscopy of hBN films transferred to SiO_2 substrates are widely reported once the high contrast between them allows the easy check of the film. Besides, optical microscope can give information about the lateral size an nucleation density on single-crystal flake samples, as reported for $MoSe_2$ [97].

In this work, images were acquired using a Motic PSM-1000 microscope with 3 lenses (10x, 50x and 100x) and a mechanical stage (Figure14). Digital images were acquired with a Moticam 5+ and the Motic Images Plus application software.

Figure 14. Optical microscope at INL facilities.

3.2 Raman spectroscopy

In 1928, the Indian physicist Raman discovered a light-scattering effect: the optical frequency changed when light was scattered by a medium due to the interaction between the incident light and molecular motion. When monochromatic radiation reaches a system with a certain angular frequency (ω_i) a part of it is transmitted, while the other is scattered (ω_d). The scattered light has two components: elastic ($\omega_d=\omega_i$) and inelastic ($\omega_d \neq \omega_i$), named as Stokes ($\omega_d < \omega_i$) or anti-Stokes ($\omega_d > \omega_i$). The wavenumbers of the Stokes and anti-Stokes lines are the direct measurements of the vibrational energies of the molecule. The shift in wavelength of the scattered light depends upon the chemical composition of the molecules responsible for scattering. Thus, Raman spectroscopy is a powerful and non-destructive characterization tool to study 2D materials. It has the capability of characterizing the structural properties of 2D materials, as well as detecting the layer thickness, band structures, strain effects, doping type or the presence of defects. The four important components of a Raman spectrometer are: a laser excitation source, a fiber-optic Raman probe, an imaging spectrograph, and a charge-coupled device (CCD) detector. A sample is illuminated with a laser beam (in the visible or near infrared range) and the scattered light is received by a lens and analyzed through a spectrophotometer to obtain a Raman spectrum from a sample.

Regarding hBN, the fundamental vibration mode is called E_{2g} mode, sometimes called G peak due to similarities with graphene. For monolayer hBN this Raman signature stands in the range from at 1368-1373 cm^{-1}. The position and FWHW of this peak depend on the thickness of the sample, as expressed in Figure 15. Additionally, other vibration modes could be present in the spectrum. hBN is usually characterized on top of a SiO_2 substrate, which has its own vibration peak at 1450 cm^{-1}. Additionally, impurities such as carbon contamination could be also detected by this technique.

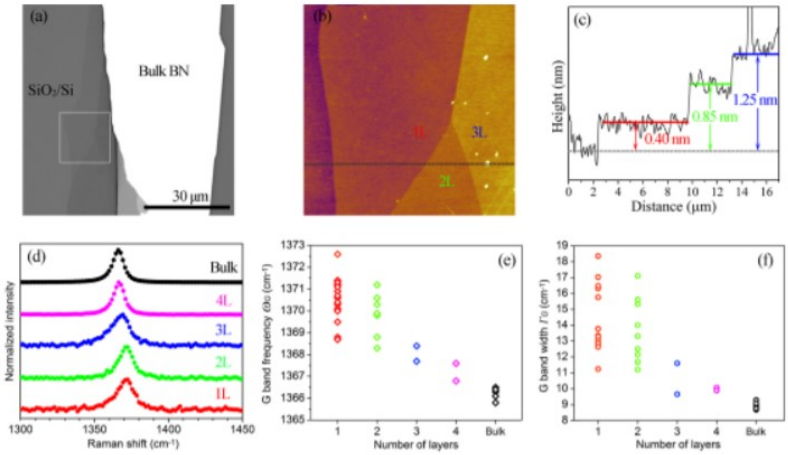

Figure 15. (a) Optical microscopy image of 1–3L BN on SiO_2/Si substrate. (b)-(c) the corresponding AFM image and height traces. (d) Raman spectra of BN nanosheets and a bulk hBN single crystal. (e)-(f) summaries of the Raman G band frequency and width. Taken from Ref. [110]

In case of $MoSe_2$, there are two main peaks in the spectrum: a sharp peak at low wavenumber corresponding to the A_{1g} mode (out of plane vibration) and another, broader peak, at high wavenumber corresponding to the E_{2g} mode (in plane vibration), as shown in Figure 16. Also, there is the presence of B_{2g} mode. This mode is inactive in bulk but becomes Raman active for reduced thickness samples due to the breakdown of translation symmetry in few layers, which is useful to identify thinner samples.

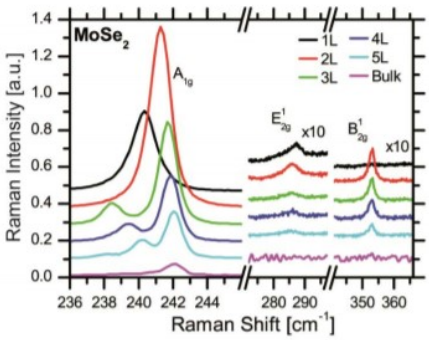

Figure 16. Raman spectra of bulk, few-layer and monolayer $MoSe_2$. Taken from Ref. [111]

Due to easy accessibility, Raman spectroscopy was the main tool used to characterize the samples and have feedback on the effect of the CVD parameters, as it allows quick identification of the deposition results. Measurements were carried out on an ALPHA300 R Confocal Raman Microscope (WITec) using 532 nm laser light for excitation at room temperature (Figure 17). The laser beam was focused on the sample by a 50x and 100x lens (Zeiss). Single acquisitions and mappings were performed with 15 mW laser power (600 g/mm grating) for hBN samples whereas 1 mW power (1800 g/mm grating) was used for $MoSe_2$ samples.

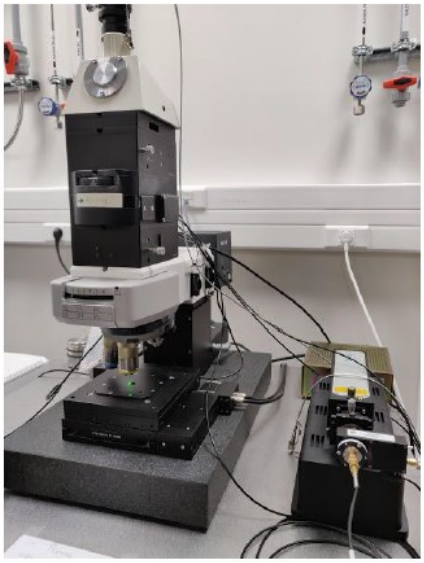

Figure 17. Raman microscope at INL facilities.

3.3 Photoluminescence

Photoluminescence (PL) is a non-destructive optical technique used for the characterization, investigation, detection of point defects or for measuring the bandgaps of materials. This optical technique is based on the light emission from a material after being with irradiated photons. Light irradiation promotes the excitation of electrons from the valence band (VB) to the conduction band (CB), forming electron-hole pairs. Following excitation, various relaxation (energy and momentum) processes typically occur towards the band minimum. Finally, the electrons recombine with holes emitting a photon with the energy corresponding to the bandgap of the material when returning to its non-excited state. The PL characterization is more suitable for direct band gap materials, where the top of the valence band and the bottom of the conduction band occur at the same value of momentum. The PL efficiency is determined by the competition between radiative and nonradiative recombination. For an indirect gap material, the PL process, which requires a change in both energy and momentum for the excited electron and hence

involves both a photon and a phonon, is a second-order process with a long radiative lifetime and therefore a relatively small efficiency because of the competition with nonradiative combination. In contrast, in a direct gap material, the emission of a PL photon does not need the assistance of a phonon to conserve momentum. Therefore, the PL process in a direct gap material is a first-order process and a much higher PL efficiency in comparison with an indirect gap material.

Even though the band structure has been studied experimentally and theoretically, hBN bandgap properties, including the bandgap energy, are not clear at present. Both direct and indirect properties of the bandgap have been reported, with the bandgap energies ranging from 3.6 to 7.1 eV [11]. Due to both lack of a proper excitation laser in the facilities and the misunderstanding of hBN bandgap energy PL measurements were not performed. By contrast, PL technique is widely used for the characterization of TMDCs. Taking $MoSe_2$ as example, the indirect-direct transition that takes place for monolayer samples enables strong photoluminescence at the wavelength corresponding to the direct bandgap of the material. The direct A and B excitons in this material are found at 1.57 eV and 1.82 eV. Figure 18 shows the photoluminescence spectrum of 1-3 layers of exfoliated $MoSe_2$. The observed emissions from monolayer and bilayer $MoSe_2$ exhibit a single prominent A exciton related maximums at 1.57 eV and 1.54 eV, respectively. Only the $MoSe_2$ trilayer exhibits two well-separated maxima with one being at the same energy as for the bilayer (related to the A exciton) and the other assigned to the indirect band gap. Actually, PL is quenched when in bulk, so it enables quick identification of the thickness of the sample (since strong PL signifies an atomically thin film) and identification of the optical bandgap as well. Besides that, PL technique can also give an indication of samples quality by analyzing the A and B exciton ratio [112], making photoluminescence spectroscopy a very useful technique in the scope of this work.

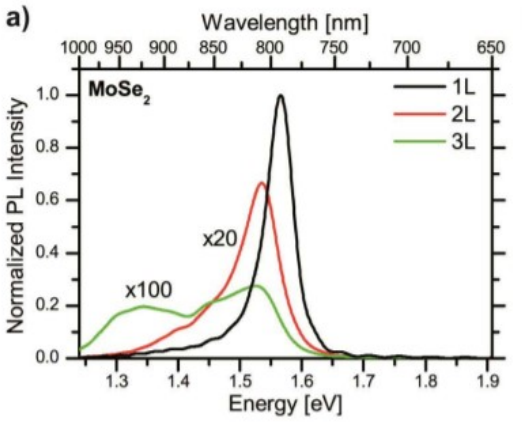

Figure 18. PL spectra of monolayer and few-layer $MoSe_2$. Taken from Ref. [111]

Both Raman and PL measurements were carried out in the same equipment (WiTec Alpha300R). The photoluminescence of the $MoSe_2$ grown samples was measured by exciting the materials with a 532 nm wavelength laser at room temperature. The intensity of the laser source is controlled by the shutter and was set to 1 mW.

3.4 Atomic Force Microscopy

Atomic Force Microscopy (AFM) is generally used to capture 3D topographic images of sample surfaces. Nowadays, it can routinely achieve atomic resolution to identify monatomic steps, ripples and also get roughness information. Any kind of surface such as an insulator, conductor or organic can be imaged by the AFM. AFM in conjunction with related scanning-probe microscopy (SPM) techniques are used to make dimensional, electrical, magnetic, optical and mechanical measurements. AFM involves scanning a sharp probe across a sample surface while capturing information about surface properties. An AFM probe is composed of a substrate, a cantilever, and a sharp tip. The substrate is a rectangular chip with sides measuring on the millimeter scale and serves as the connection point for the probe. The cantilever protrudes from the substrate and at is end there is the tip, the part that interacts with the sample surface and provides high resolution. The AFM probe is capable of high-resolution imaging due to a combination of: i) efficient piezoelectric actuation that is used to precisely drive the tip or the sample, ii) the use of a sharp tip with optimal mechanical properties; and iii) a fast feedback control loop for maintaining the user-defined tip-sample interaction. The piezoelectric actuators together with the feedback loop allow for tip or sample movement control at a picometer scale. Typically, these micro-cantilever systems are operated in three open-loop modes: (i) non-contact mode, (ii) contact mode, and (iii) tapping mode. In the non-contact mode the cantilever is moved slightly away from the sample surface and kept oscillating at or near its natural resonance frequency. By mounting the cantilever on a PZT element and measuring the shift from its natural resonance frequency due to sample attractive interactions, topographical information of the sample can be extracted. Alternatively, the contact mode acquires sample attributes by monitoring interaction forces while the cantilever tip remains in contact with the target sample. However, this mode might cause damage to the sample due to contact from the tip. The tapping mode of operation combines qualities of both the contact and non-contact modes by gleaning sample data and oscillating the cantilever tip at or near its natural resonance frequency while allowing the cantilever tip to impact the target sample for a minimal amount of time. As the AFM tip moves over features of different height the deflection of the AFM cantilever changes. This deflection is tracked by a laser beam reflected from the back side of the AFM cantilever which often has a thin metal coating, making it a mirror and

directed into a position sensitive photodetector. The amount of bending is monitored and recorded by position-sensitive photodiodes (PSPD) that are arranged in four quadrants. The amount of bending is then converted by a pre-defined algorithm to produce the final image. The mechanism is illustrated in Figure 19a.

This technique is mostly used to extract height profiles in 2D materials. Its high resolution allows for the observation with unprecedented small steps and thus has been routinely used to measure the thickness of 2D materials, including hBN which monolayer thickness is ~0.55nm [84] and $MoSe_2$ whose monolayer thickness is known to be ~0.7 nm [99]. AFM measurements in this experimental work were made under tapping mode as to avoid damage to the films. Firstly, a region with a scratch (where the substrate was visible underneath) was selected to make the thickness measurements. Gwydion, open source software, was used to analyze the gathered data and make an adequate fitting. Atomic force microscopy (AFM) (Bruker Dimension Icon) was used to determine the thickness of the films (Figure 19b).

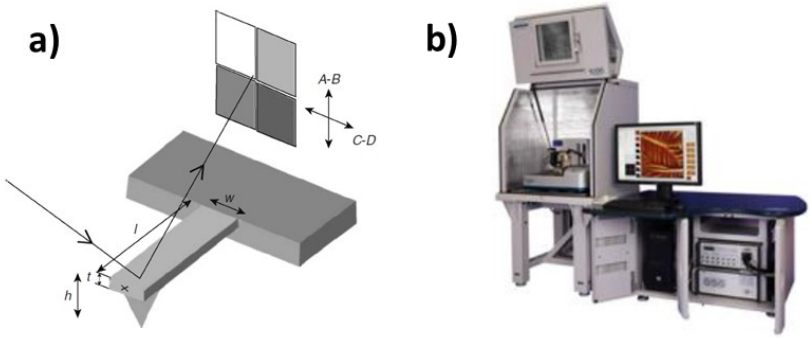

Figure 19. a) Detection of cantilever deflection by a laser beam reflected from the rear side of the cantilever. Taken from Ref. [113]. *b) Atomic force microscope at INL facilities.*

3.5 Scanning Electron Microscopy

Scanning electron microscopy, or SEM, is a non-destructive technique that uses an electron beam to achieve greater magnification than cannot be achieved through optical microscopy. The sample is shot in an SEM using a high energy electron, and the outcoming electrons/X-rays are analyzed. These outcoming signals give information about topography, morphology, composition, orientation of grains and crystallography of a material. In a typical SEM, a source of electrons is focused into a high energy beam. These electrons are projected in a raster manner over the surface of the sample. Three types of electronic signals can be emitted from the surface of the specimen exposed to the incident beam: back scattered electrons which possess energy close to that of the incident beam, secondary electrons which have a

kinetic energy less than 50eV and Auger electrons produce by deexcitation of atoms. The de-excitation of atoms also produces a photon within an emission domain in the range x-ray to visible. This process is illustrated in Figure 20.

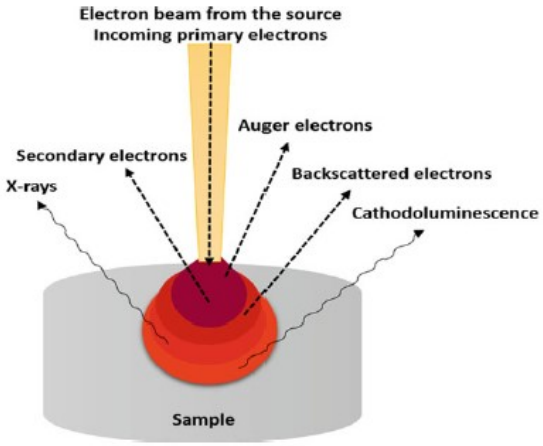

Figure 20. The interaction between the electron beam and the sample and the consequent emitted signals. Taken from Ref. [114]

The signals are gathered by detectors, which are then manipulated by the computer to form the required analysis. According to the detected signal (secondary electrons, backscattered electrons or X-rays), different information about the sample could be observed. The two routinely used electrons for sample image creation are the backscattered and secondary electrons. However, secondary electrons are considered the most important electrons, indicating sample morphology and topography, while backscattered electrons are used for demonstrating the contrasts in multiphase samples composition. The released X-rays are used primarily for chemical analysis rather than imaging since the energy of each X-ray is unique to the specific element and transition. This is the principle of energy-dispersive X-ray (EDX or EDS) analysis. EDX detectors are normally used together with SEM for a more detailed characterization. SEM has a specific sample holder where the stub should be fixed containing the sample on the surface. Generally, carbon tap is used for sticking the sample to the stub. First two-sided carbon tap should fix on the stub and then a thin layer or a small amount of material will be placed on the carbon tap because the thin layer properly sticks with the carbon tap which reduces the charging problem and help in getting a good image. Additionally, the samples to analyze in SEM must be electrically conductive to avoid overcharging on the surface. This overcharging may introduce extreme brightness and poor images. Thus, non-conductive samples like polymers are usually sputter coated with a thin layer of carbon or metal that readily reflects electrons and provides a conductive surface.

Due to insulator behavior of hBN it is difficult to identify on top of insulating substrates such as SiO_2 or Si. This is due to the charge built up on the insulating surface under electron beam irradiation, which repels

further incident electrons and restricts the secondary electron generation. Normally, the use of conducting substrates or metal coatings can improve the images. SEM allows to identify domain size and coverage of hBN films as well as the typical wrinkle and striations [91]. SEM has been also used to characterize CVD grown $MoSe_2$ nanosheets [94]. It allows to know the morphology of the surface in greater detail than with an optical microscope, as well as better contrast between the substrate and the grown film. Besides that, it can help identification of the composition of any contaminants or particles resulting from the deposition, namely the presence of oxides. In this work, SEM images were taken at a FEI Quanta 650 FEG with a cold field electron source, at 5 kV voltage (Figure 21).

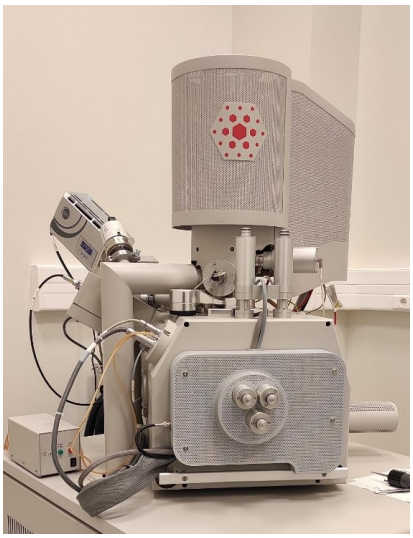

Figure 21. SEM at INL facilities.

3.6 X-ray photoelectron spectroscopy

XPS technique is primarily used to quantify the chemical and electronic states of the elements existing within the first few atomic layers of a material's surface. It is a surface analysis technique with a sampling volume that extends from the surface to a depth of approximately 50-100 Å. By using this technique, the elements in the material's surface, their chemical bonds and hence the chemical composition and empirical formulae (stoichiometry) can be also identified. In a XPS experiment, a beam of X-rays strikes the sample surface and interact with the atomic electrons in the sample, mainly by photon absorption to produce the ejection of photoelectrons. These x-rays are generally emitted from magnesium or aluminium source and therefore intensity of the ejected photoelectron form the sample is plotted as a spectrum of their binding energies. The obtained spectrum is compared with spectra from standard databases. The peak positions and shapes correspond to the material's electronic configuration, and therefore elements compounds show their own unique characteristic peaks.

Regarding hBN, the presence of B and N has been identified at 190.3 eV and 398.8 eV, respectively [90]. Two small broad peaks also can appear at energies of 9 eV and 25 eV (plasmon and bulk plasmon loss peaks) higher than the B 1s and N 1s core level peaks, respectively, which is a fingerprint signature of the sp2 bonding between B and N atoms [115]. XPS has also been useful to identify the stoichiometry and elemental composition of $MoSe_2$ films. The binding energies of Mo 3d3/2 and Mo 3d5/2 are ~232.4 eV and ~229.3 eV, and the binding energies of Se 3d5/2 and Se 3d3/2 are ~54.9 eV and ~55.8 eV respectively, as reported [97]. Sometimes the presence of oxides is also noticed, namely MoO_x oxide. In the scope of this experimental work, XPS was utilized to obtain a measure of the stoichiometry of the grown hBN and $MoSe_2$ samples. XPS measurements were carried out in an ESCALAB 250Xi system (Figure 22).

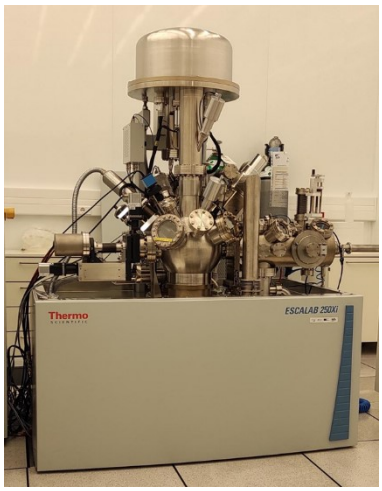

Figure 22. XPS at INL facilities.

3.7 Transmission electron microscopy

TEM has been commonly used to obtain varied information about materials, including their morphology, crystallography, particle size distribution and element composition. Thus, this technique can provide a better understanding about the physical and chemical properties of the materials under study. The TEM operates on the same basic principles of image formation as the light microscope but uses electrons instead of light. Because the wavelength of electrons is much smaller than that of light, the highest image resolution attainable in TEM images is many orders of magnitude better than that from a light microscope. In TEM, a beam of focused high energy electrons is transmitted through a thin specimen in order to generate an image of the area being illuminated. The beam of electrons, generated by the electron gun, is focused into a small, thin, mostly parallel beam by the condenser lenses. As the electron beam passes

through the sample, most of the beam is transmitted, with electrons being either deflected or undeflected. The transmitted electrons are focused by the objective lens, then amplified by the projector lenses to finally produce the desired image on the fluorescent viewing screen. A wide variety of materials including metals, minerals, ceramics, semiconductors, and polymers can be characterized by TEM. However, one of the most important conditions required is that the sample must be appropriately thin to allow the electrons to transmit through it, allowing for a readable image to be acquired. TEM has the capability to provide both images and selected area electron diffraction patterns (SAEDPs) of the same region by adjusting the strength of the magnetic projection lenses. In nanotechnology, SAEDPs offer a unique capability to determine the crystal structures of nanomaterials and different parts of a sample. Recently, high-resolution transmission electron microscopy (HRTEM) has become a powerful tool for nanostructured materials characterization, due to its to capability to characterize nanostructures with resolution as low as one angstrom, allowing for the direct imaging of their atomic structure.

Scanning transmission electron microscopy (STEM), another type of TEM, is a characterisation technique that can reach sub-Å resolutions, making it a powerful method to observe and study materials at the atomic level. Unlike in conventional TEM, electrons are focused into a convergent probe of sub-nanometre dimensions to scan the sample, where the particles are scattered to many directions according to the fine structural and chemical details of the sample. The contrast of a STEM image is therefore closely tied to the scattering angle of the transmitted electrons, so that annular-type detectors with varied angular ranges are used to obtain different types of information from a particular specimen. These detectors integrate the intensity of the scattered beam at each raster position, ultimately generating an image made up of all the collected points in the scanned area. Taking a prominent imaging mode as an example, high-angle annular dark-field (HAADF) imaging uses a detector designed for large scattering angles to achieve image contrast that is directly related to mass-thickness, allowing even for differentiation between light and heavy atomic species through a dependence with Z^2 (where Z is the atomic number).

In general, transmission electron microscopy is a powerful method to study 2D materials. As stated above, HAADF-STEM is a technique suited to the identification of point defects, grain boundaries and layer thickness, based upon HAADF intensity, which varies with Z. The individual B and N atoms and the impurity atoms inside the BNNS have been successfully detected by HAADF-STEM analysis [116]. The crystallinity of the BNNS is generally examined by SAED analysis in TEM [82]. The appearance of six-fold symmetrical spots in the SAED pattern confirms the presence of crystalline BNNS. TEM is also widely used for structural analysis of TMDCs. In case of $MoSe_2$, this technique has been employed in the investigation of both single-crystal flakes and films. In the first case, it has been used to accurately

measure the lateral size of single-crystal monolayer $MoSe_2$. For multilayer flakes, bright-field TEM image could be used to identify the stacking growth mode [117]. Regarding $MoSe_2$ polycrystalline films, TEM can be an helpful tool in finding domains and grain boundaries [118]. Analogously to hBN, SAEDPs from $MoSe_2$ samples are used to confirm the hexagonal single crystalline nature of the material. In this work, the structure and composition of the samples was investigated with an aberration-corrected FEI Titan Cubed Themis (operated at 60 kV) equipped with X-FEG electron source, image corrector, probe corrector and Super-X EDS system (Figure 23).

Figure 23. TEM at INL facilities.

4. GROWTH OF 2D HBN

4.1 Materials and methods

The growth of hBN films was carried out in a two-zone split tube furnace (1" quartz tube) at atmospheric pressure (Figure 24). The left furnace sets the temperature of the precursor while the right one is meant to control substrate temperature. During this experimental work an extensive optimization of process was carried out, spanning from the substrate and precursor pre-treatments to the CVD parameters fine-tuning.

Figure 24. CVD furnace at INL.

Precisely, 25-µm thick foils (cut in squares, with an area up to 2×10 cm^2) were used as substrates. Prior to deposition, the substrate was cleaned by three different methods: Ac+IPA+DIW; Ac+IPA+DIW+HCl (5%) and an aqueous solution (280ml DIW, 10 ml HCl 37%, 2.5ml 2M $FeCl_3$). The substrate was then dried with N_2 flow, placed on a cleaned Si/SiO_2 holder and loaded into the second heating zone of the furnace. Later, 8.5 mg of AB, chosen as precursor, was placed in an Al holder and loaded in the first heating zone of the furnace (25/45cm upstream from the substrate). The process started with a tube purging which took 20 min under an Ar/H_2 flow (100 sccm of a mixture of 95% Ar and 5% H_2). After the purge, the second heating zone was ramped up to 1020°C (40°C/min) to anneal the Cu foil substrate (40 min at 1020°C under the same Ar/H_2 mixture). After the annealing, the Cu was allowed to cool down to room temperature by opening the furnace lid. To investigate the Cu annealing role in the hBN growth, a specific experiment without the previous step was done. Then, the first heating zone was heated up to perform the AB pre-treatment. Several pre-treatment conditions were tested such as temperature (80°C and 100°C), time (150 and 180min) and Ar/H_2 flow (95/5%) (15 and 100 sccm). Again, in a particular experiment AB was not performed in order to investigate its role, passing directly to the growth. Once the AB pre-treatment was completed, the first heating zone was kept in the same pre-treatment conditions

and the second heating zone was ramped up to 1020°C (40°C/min) for the hBN growth, which lasted for 30/60 min under 100 sccm Ar/H_2 flow (95/5%). After the growth, both furnaces were turned off and allowed to cool down before retrieving the samples. Both schematic illustration of the setup and the temperature timeline for each furnace are shown in Figures 25 and 26.

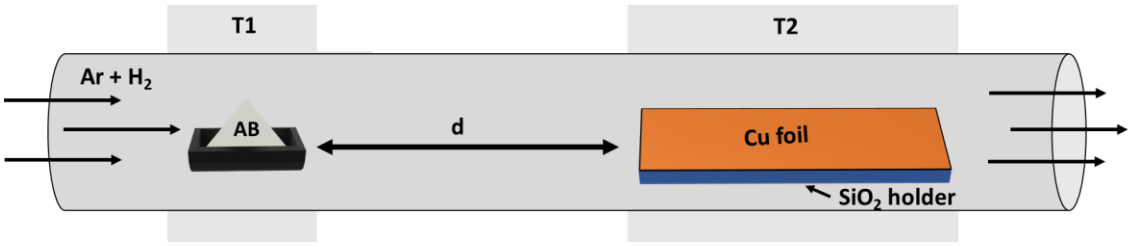

Figure 25. Schematic illustration of the experimental setup utilized for the synthesis of hBN films.

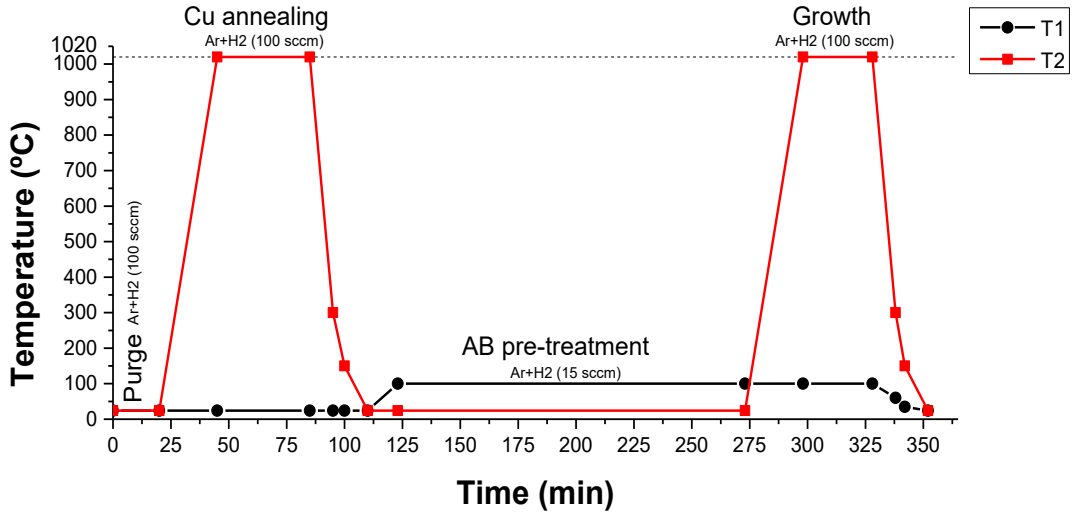

Figure 26. Temperature timeline for each furnace during the procedure.

After growth, hBN films were transferred onto SiO_2/Si substrates by PMMA-assisted method (Figure 27) [119]. A layer of PMMA was spin coated on the Cu/hBN sample. The Cu backside was cleaned via O_2 plasma (250 sccm O_2 flow, 0.4 mbar, eight consecutive cycles of 30s plasma exposure, 200W RF power) to remove the adventitious hBN. The cleaned Cu/hBN/PMMA sample was placed in a 0.2 M $FeCl_3$ solution for 2 h to etch away the Cu. After the etching, the freestanding hBN/PMMA sample was rinsed in deionized water several times and scooped out of the water bath with a SiO_2 substrate (and then dried on a hot plate at 65°C for 30min). It is worth to mention that other target substrates were used such as Si or borosilicate glass cover slips, to meet the requirements of specific experiments. The sample was

soaked in an acetone bath overnight to remove the PMMA coating. Finally, the sample was rinsed in IPA and deionized water (15 min each) and dried gently under N_2 flow.

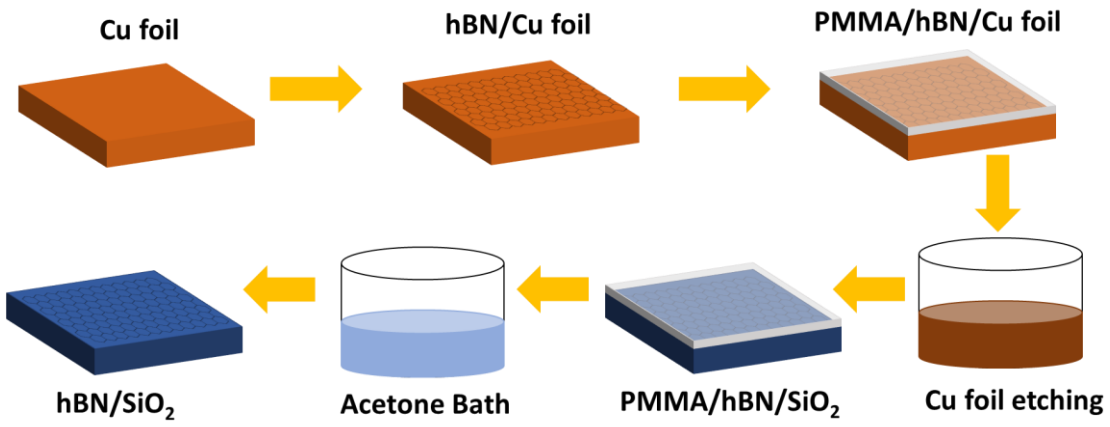

Figure 27. Schematic illustration of the PMMA-assisted transfer.

4.2 Parameters and optimization

4.2.1 Cu foil cleaning

The Cu foil substrates were cleaned prior to deposition in order to remove any oxide layer and organic contaminant. To ascertain the most efficient cleaning treatment, three different methods were tested. As first attempt, a standard procedure was used: soaking the Cu foil in acetone, IPA and DIW (15 min each, Method 1). Although acetone and IPA can remove organic components, another cleaning step is needed to remove the superficial oxide layer, which may adversely affect the Cu catalytic properties. Method 2 consists of adding a final 30 min bath in HCl at RT to Method 1. As it can be seen in Figure 28, for the same growth conditions A (Precursor Temperature: 80°C; Growth Temperature: 1020°C; Time: 60min; 100sccm flow of $Ar+H_2$), the use of Method 2 led to a more uniform film with less contamination, meaning that HCl bath was beneficial. Furthermore, based on graphene grown on Cu reports, a third pre-treatment was tried. The procedure consists of soaking the Cu foil in an aqueous solution (280ml of DIW, 10 ml of HCl 37% and 2.5ml of 2M FeCl3) for 1 min in ultrasonic bath followed by a de-ionized water rinse. For the same growth conditions B (Precursor Temperature: 100°C; Growth Temperature: 1020°C; Time: 30 min; 100sccm flow of $Ar+H_2$) no apparent difference can be noticed regarding uniformity but the latter seems to show fewer contaminations on the hBN film. Thus, Method 3 shown to be the most efficient way to clean Cu substrates prior to deposition.

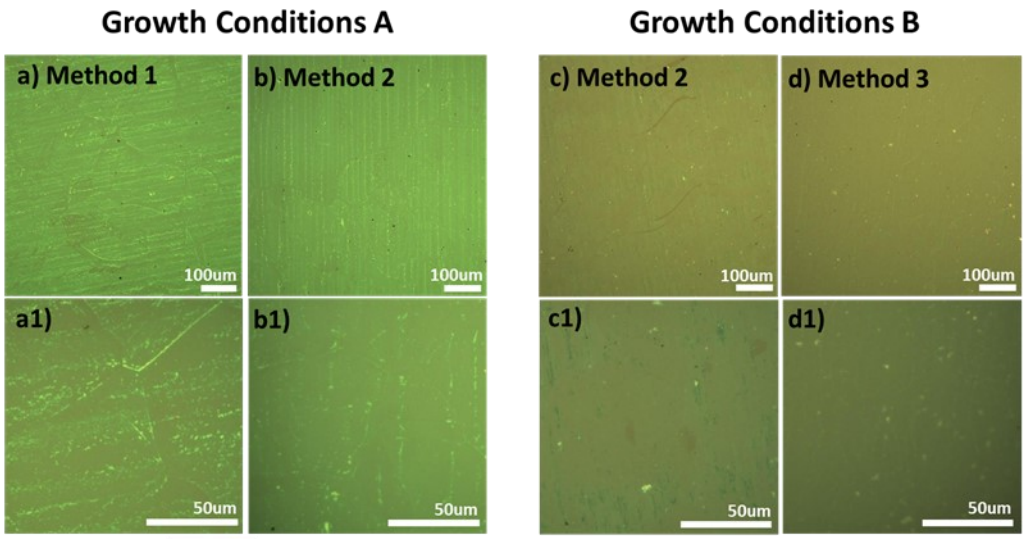

Figure 28. Optical Microscope images of the grown films using a)-a1) Method 1, b-b1)/c-c1) Method 2 and d-d1) Method 3 to clean the Cu foil substrate prior to deposition. Two growth conditions were used during the experiments.

4.2.2 Cu pre-treatment influence

Cu pre-annealing may also play a crucial role in the hBN growth. Long Cu substrate annealing at high temperatures is known to facilitate the growth of single hBN crystals with high lateral size and reducing nucleation. For this, annealing temperature and atmosphere should be tuned to induce the desire transformation of crystallographic structures on the Cu foil. Despite a Cu annealing optimization was not done (in terms of temperature and atmosphere) during this work Cu annealing importance was proved. Figures 29a-b show OM images of the film grown without and with Cu annealing step, respectively. The first one was revealed to be a carbon-based film, as evidenced by the prominent D and G bands in the Raman spectrum (Figure 29a1). On the other hand, Figure 29b1 confirms the successful growth of a hBN film, proved by the presence of E_{2g} vibration mode peak at 1370 cm^{-1}. With this, Cu annealing proved to be a crucial optimization step in our procedure.

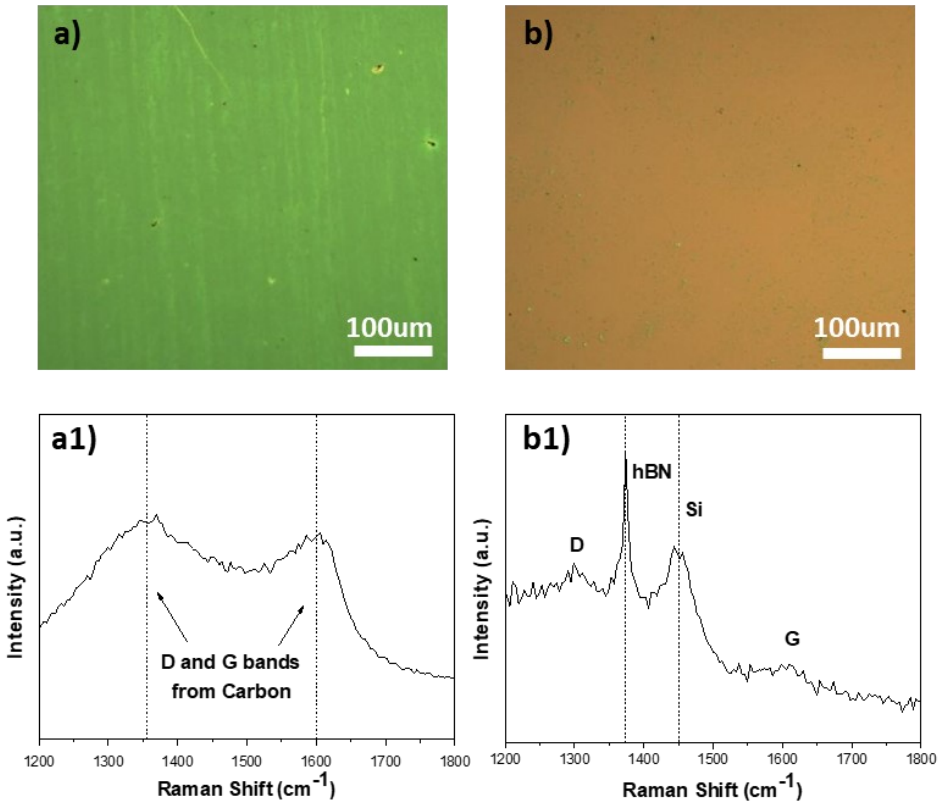

Figure 29. Optical Microscope images of the samples grown a) without and b) with Cu annealing step. a1-b1) Representative Raman spectrum of each sample, respectively.

4.2.3 AB pre-treatment tuning

AB is an effective precursor for the CVD growth of hBN, but its thermal decomposition is rather complex and difficult to control. A controlled decomposition of AB before and during CVD growth is crucial to provide a balanced flow of N_xB_y species along the tube, to reach and react with the heated Cu surface. First, the effect of an AB annealing pre-treatment was evaluated by comparing two kind of hBN films: a) with no AB pre-treatment and b) with an AB pre-treatment done at 80°C for 180 min. Figures 30a-b show that the AB pre-treatment led to a more uniform and thinner film (as evidenced by the optical contrast in Figure 30a). This is confirmed by the Raman spectra (Figure 30c), showing more intense E_{2g} and SiO_2 vibration bands for the film grown with the AB pre-treatment. Thus, AB pre-treatment must be considered for proper hBN growth.

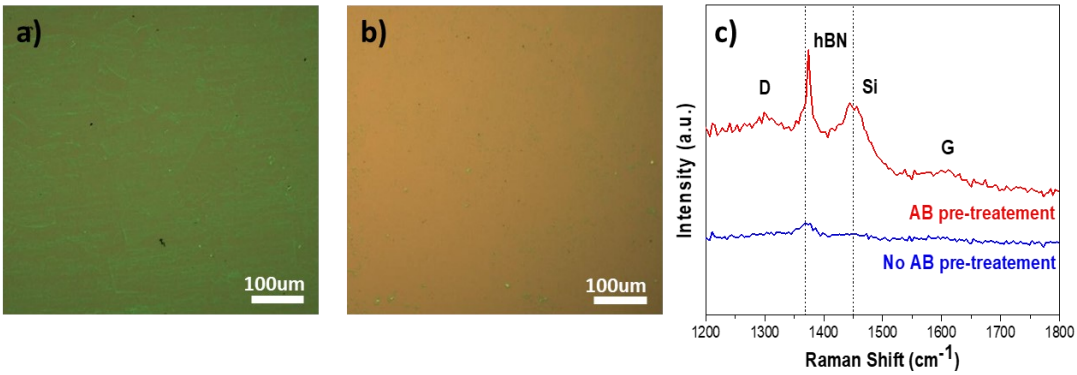

Figure 30. Optical Microscope images of a sample grown a) without and b) with AB pre-treatment. (c) Representative Raman spectrum of each two films.

Among the list of precursors available for the synthesis of 2D hBN, AB was chosen. By controlling the solid-state phase transition of AB via heating, it is possible to maximize its volatility and release gaseous AB. In this work, AB pre-treatment was perfect to optimize its solid-state phase transition: This was accomplished by adjusting (i) the AB temperature, (ii) treatment time and (iii) gas flow. The first two steps have major influence on the success of the AB pre-treatment because it is known to be essentially a time and temperature-dependent process. As an example, if time is too long or the temperature too high there is the risk of total AB decomposition, which would supress hBN growth. On the other hand, not sufficient time and temperature would not allow AB decomposition. During the experiments three conditions were studied, namely: a) T=80°C for 150min; b) T=80°C for 180min and c) T=100°C for 150min. Figures 31a-c show Optical Microscope images of the respective grown films. By optical contrast, it is possible to claim that the samples vary in thickness, uniformity, and contamination. In fact, Figure 31c looks thinner and cleaner, when compared to the first ones. Raman Spectra illustrated in Figures 31a1-c1 confirm that, under the three conditions, hBN is present due to the occurrence of E_{2g} peak. Actually, the representative Raman spectrum of the sample grown with a) conditions show that it is thicker due to the absence of SiO_2 substrate peak (which means that the film is thick enough to quench the signal from the substrate). Besides that, it also shows the presence of carbon contamination backed by the presence of D and G carbon bands. Conditions b) led to a somehow different spectra since Si vibration mode is now visible. Furthermore, the contribution from D and G bands seems to decrease substantially. Lastly, c) conditions seem to be optimal since E_{2g} and Si related peaks show a balanced ratio (in contrast to what happens in Figure 31b1) while D and G carbon band are now negligible, meaning that carbon contamination was dramatically reduced. Therefore, conditions c) were adopted for the AB pre-treatment.

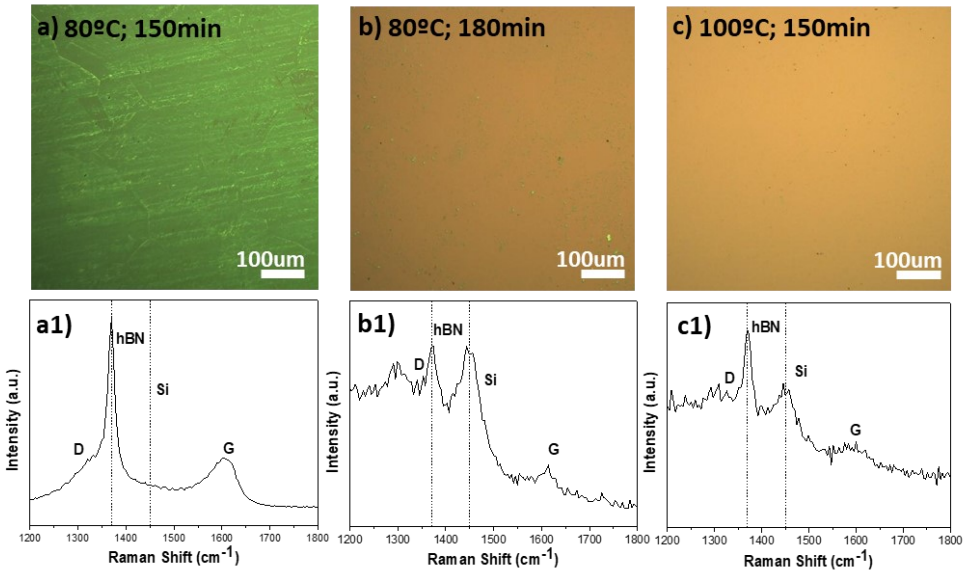

Figure 31. Optical microscope images of the films grown with three different AB pre-treatment conditions: a) T=80°C for 150min; b)T=80°C for 180min and c) T=100°C for 150min. a1-c1) Representative Raman spectrum of each film.

Furthermore, during AB pre-treatment, BN nanoparticles might be released from the solid AB so the established Ar+H_2 flow could possibly transport them into the growth zone, leading to undesired contamination. For this reason, the Ar+H_2 flux during the AB pre-treatment was also investigated. Figure 32a shows an optical microscopy of the hBN film grown with 100sccm while Figure 32b is referring to the film grown with a flux of 15sccm. A quick comparison between both optical microscope images allows to claim that a low flow during the AB pre-treatment leads to a less contaminated film. Figure 32c shows the representative Raman spectrum of each film. Comparing both spectra it is visible that reducing the flow helped sharpening the E_{2g} peak and, most important, helped reducing D and G carbon bands, meaning that carbon became less frequent in the sample.

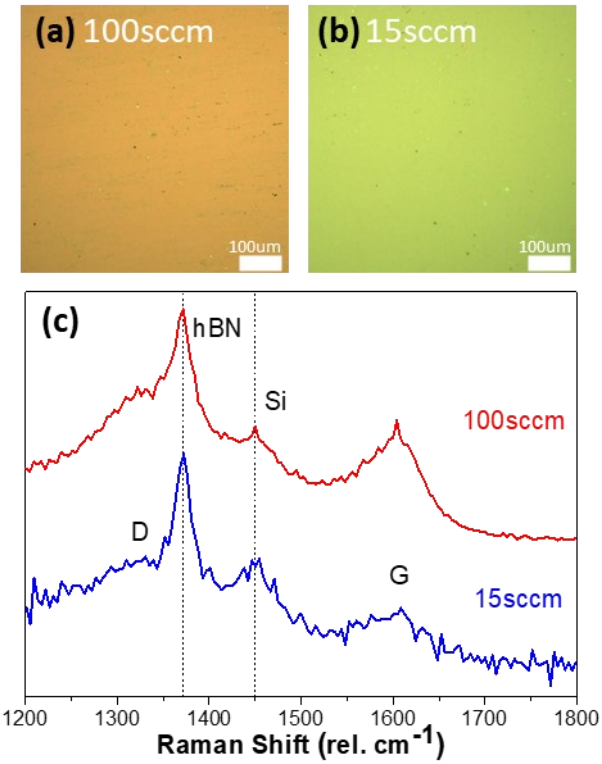

Figure 32. Optical microscope images of the films grown with an Ar+H_2 flux of a) 100sccm and b) 15sccm. (c) Representative Raman spectrum of each sample.

4.2.4 Distance between AB and Cu foil

Atmospheric-pressure CVD procedures imply less controlled atmospheres inside the reaction tube, which turn unpredictable the growth conditions in each zone of the tube. This fact combined with other factors such as temperature gradient and gas flow dynamics cause a non-uniform concentration of active species along the quartz tube. Besides that, the by-products arising from the composition of the AB can also influence the growth conditions along the tube. This fact suggests an optimization regarding the position of the Cu foil substrate in order to have uniform and continuous growth. In our experiments, the distance between the precursor and the Cu foil was varied: a 10cm long Cu foil was placed 25cm (ranging from 25-35cm) and 45cm (ranging from 45-55cm) from the AB precursor. After growth, different portions of the Cu foil, representing the several distances, were transferred. Each portion was then characterized by Raman spectroscopy and the representative spectra are illustrated in Figure 33. Although E_{2g} vibration mode was detected in each sample, meaning that all distances are suitable for hBN growth, the contribution from D and G carbons bands change throughout the tube. For 25-30 cm spectra D and G band are prominent (although less intense for 35cm) meaning that carbon contamination in these samples is considerable. However, when distance was increased to the range 45-55cm carbon related

bands softened and a more balanced ration between hBN and Si vibration modes is displayed. As a consequence, 45cm was adopted as optimal distance for hBN growth.

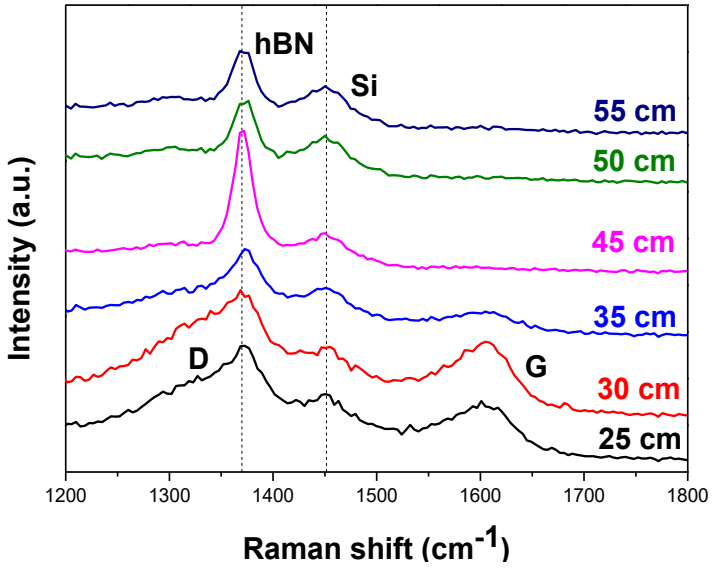

Figure 33. Representative Raman spectrum from different portions of the Cu foil.

4.2.5 Growth time

Growth time is reported to be as an effective way to regulate the thickness of hBN films [91]. The growth pattern of these films is known to follow Stranski–Krastanov model, i.e., at the first stage layer-by-layer growth takes place (allowing the lateral growth of films) however after a critical time vertical growth becomes dominant leading to an increase in thickness. In other to understand the role of the growth in our procedure two growth times were studied: 30min and 60min. Figures 34a-b show optical microscope images of the two films, respectively. The well-defined borders of each film allowed to perform accurate AFM measurements of the thickness, that are displayed in Figures 34a1-b1. A 30 min growth gave rise to a 1.8nm thick hBN film, which is the value reported for 4-5L hBN [120]. Increasing the growth time to 60min had a big impact on the thickness, the measured value went from 1.8nm to 6.4nm, which corresponds to >8 layers [121]. This observation allows us to claim that it is possible to tune film thickness by varying the growth time. Consequently, a 30 min growth was adopted in order to keep the few-layer nature of the grown films.

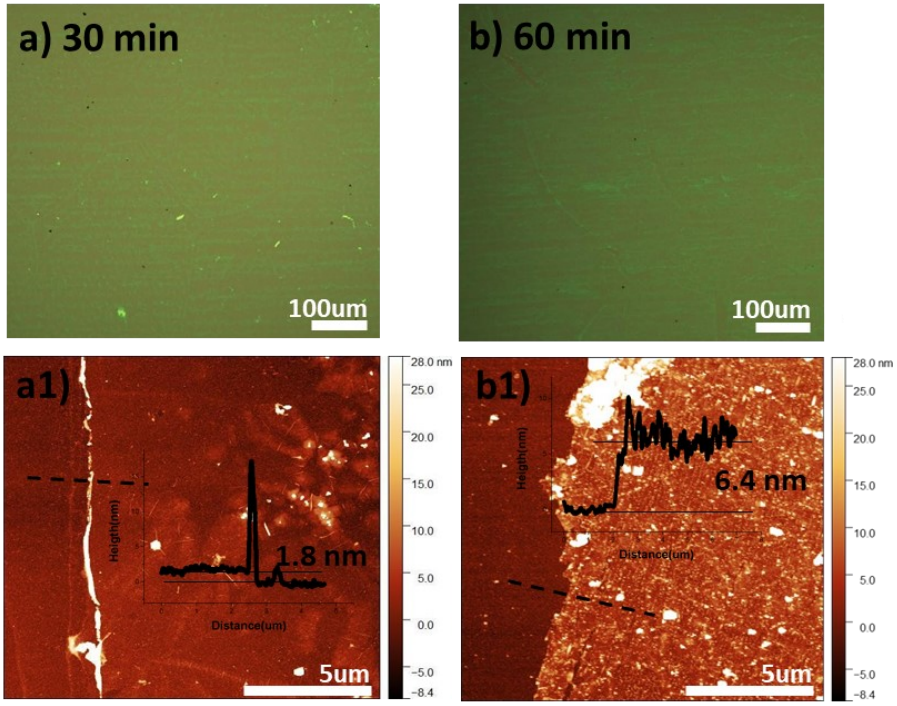

Figure 34. Optical microscope of the hBN films grown with a) 30 min and b) 60min. a1-b1) AFM and line profile of each film, respectively.

4.3 Characterization of the optimized sample

After the previous optimization tests, a series of atomically thin hBN samples were produced, which completely covered Cu substrates with areas up to 20 cm^2. Portions of the film were then transferred to a Si/SiO_2 substrates for characterization. The film edge is clearly visible in the photograph in Figure 35a, as is in the optical micrograph in Figure 35b. The samples were then characterized by confocal Raman spectroscopy. The representative spectrum in Figure 35c shows a strong E_{2g} peak at 1369 cm^{-1} typical of 2D hBN, and a less intense peak at 1450 cm^{-1} (originating from the Si substrate). Two weak D and G bands also appear due to minor carbonaceous contaminations. A map of the E_{2g} peak intensity taken from a representative area of the film is shown in Figure 35d. The E_{2g} peak appear constant throughout the area indicating a continuous and homogenous film; only minor intensity fluctuations appear (as bright spots), possibly due to subtle carbon contamination (which translates in an intense D band and therefore changing the intensity of the peak) or thickness variations. The darker bottom-right corner of the map corresponds to the bare SiO_2 substrate where the E_{2g} peak is absent.

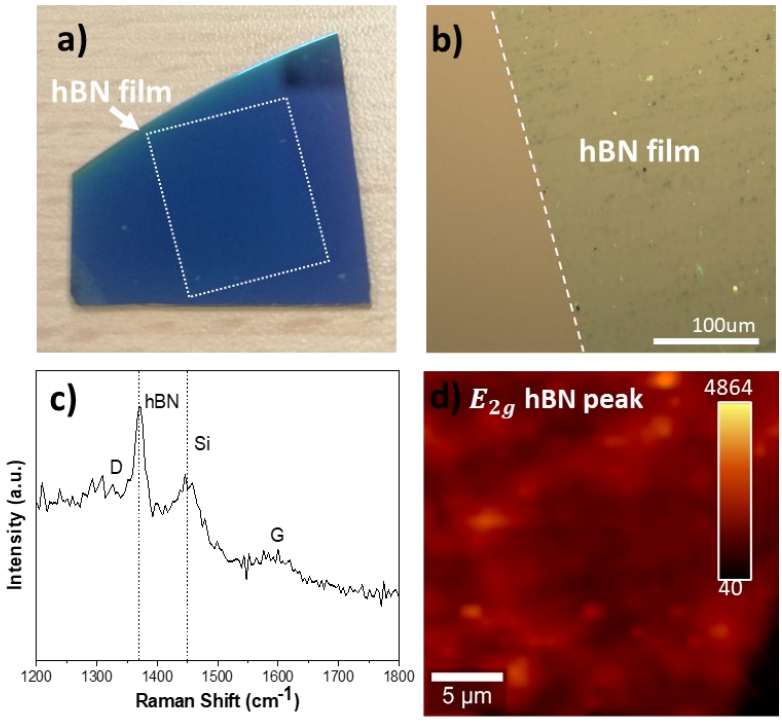

Figure 35. a) Photograph of the transferred hBN film over a SiO_2 substrate. c) OM image of the grown film. c) Representative Raman spectrum of the sample. e) Raman map tracking the intensity of the E_{2g} peak. The map was taken on 45x45 points in a 30x30 μm^2 area.

AFM measurements of the thickness revealed ~3 nm thick films (Figure 36 a). The close-up AFM image in Figure 36b shows the typical wrinkles of 2D films after transfer. In both AFM images the occasional presence of tiny white spots was noticed, which could be assigned with nm-sized SiO_x particles as previously reported for graphene grown on Cu substrates in quartz-tube furnaces [122]. Figures 36c show SEM images of the hBN film transferred onto a Si substrate. The film can be identified by the several bright wrinkles visible all over the area. Again, nm-sized particles were found, highlighted by the white arrows in Figure 36d.

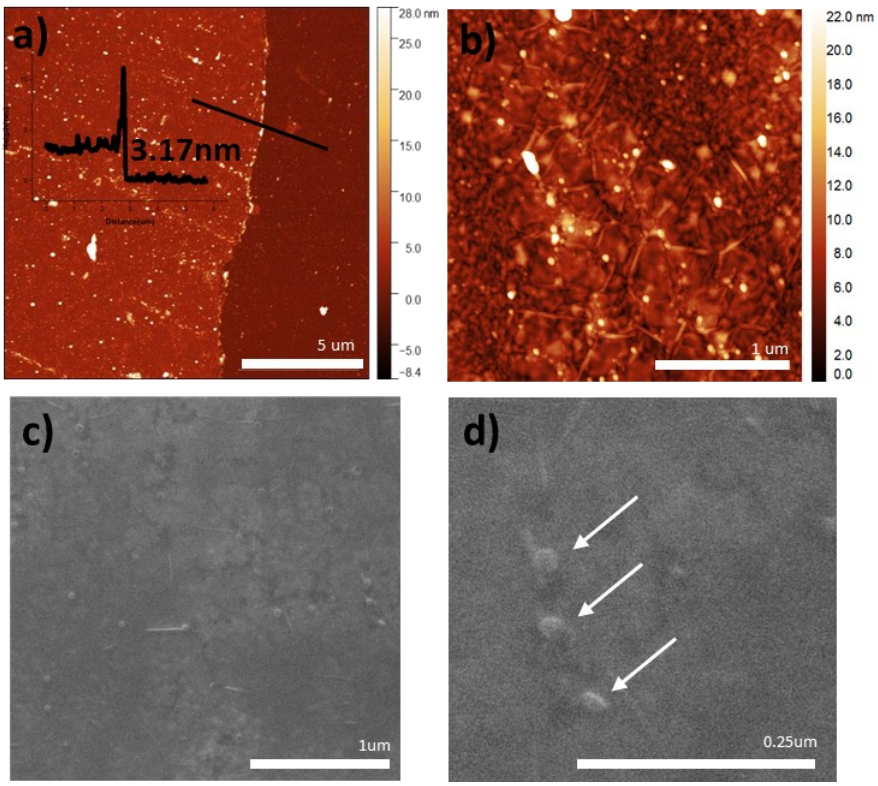

Figure 36- a) AFM and line scan profile of the hBN film. b) AFM close-up image of the hBN film. c-d) SEM images of the hBN film. The white arrows highlight the presence of tiny SiO_x particles.

Transmission electron microscopy (TEM) was performed to analyze the structure and composition of the hBN films. Figure 37a shows the hBN film lying on the lacey carbon grid. Besides that, nm-sized particles (black spots) can be easily identified. The selected area electron diffraction (SAED) pattern (inset) shows circular rings instead of individual spots, suggesting that the h-BN film has a polycrystalline structure. Figure 37b reveals the few layers composing the film, with a perfect interlayer spacing of 3.3 Å. The close-up, top view of the film in Figure 37c highlights an area with three distinct thicknesses, attributed to one to three layers. In other to detect the presence of potential contaminations, possibly originated during the growth or the successive transfer energy dispersive X-ray spectroscopy (EDX) was employed (Figures 37d-i). The elemental distribution of N, B, Fe, Cl, and Si was mapped. The B and N maps show the uniform presence of the main hBN elements in the film. An intensity contrast is visible in both maps, meaning that the area of analysis has different thicknesses. The maps of Cu, Fe and Cl highlight the fact that some residues arising from the transfer process can appear, as described in section 4.1. Apart from that, there is also the presence of SiO_x particles, as previously discussed.

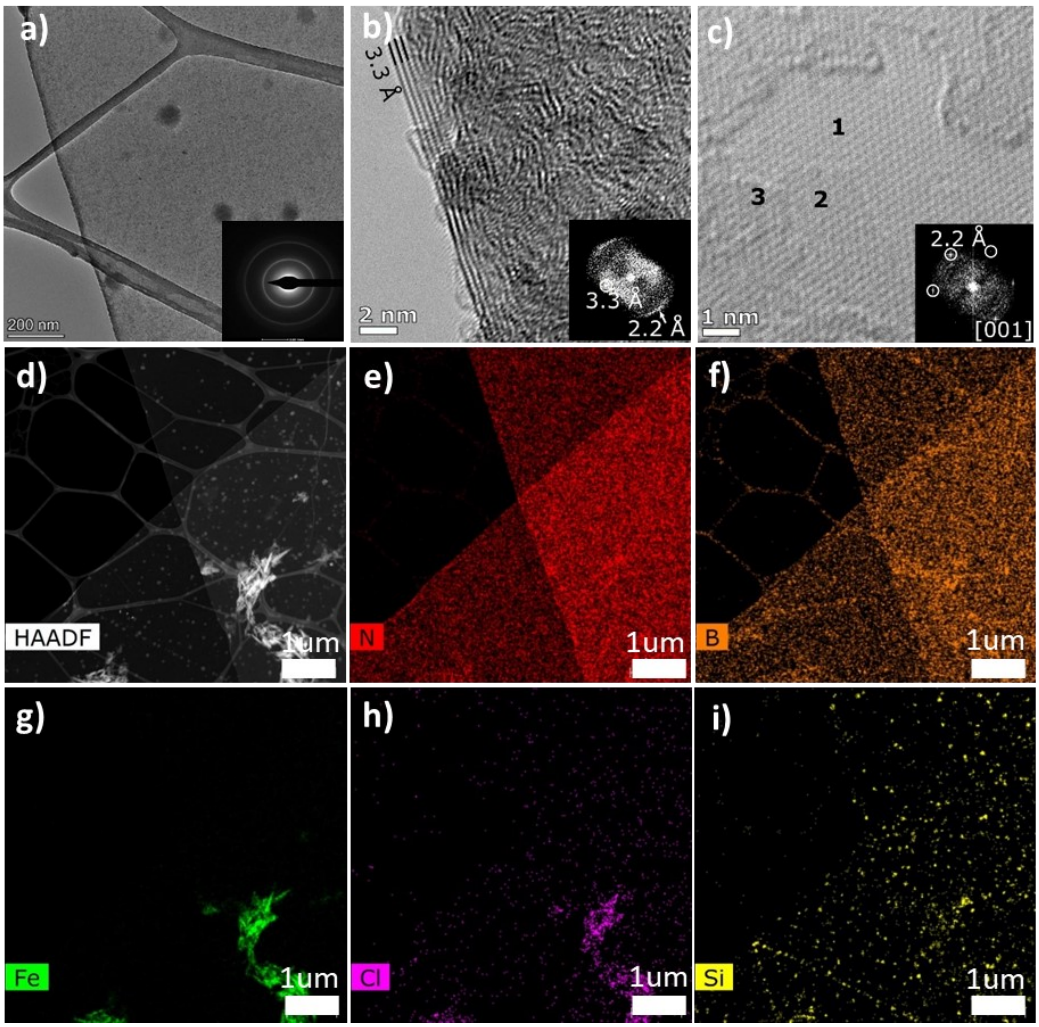

Figure 37. a) TEM image of the hBN film with electron diffraction (inset) .High-resolution TEM image of the hBN film, with b) showing the interlayer spacing of 3.3 Å and c) showing three layers of hBN (numbered 1-3). d) HAADF-STEM and e)-i) corresponding EDX mapping.

Additionally, XPS was conducted to characterize the elemental stoichiometry of the synthesized hBN samples. Figure 38a shows the characteristic survey of the film. Other than B and N, there is a minimal contribution from other elements, as expected. C and O are generally present in samples exposed to air while the Si contribution is due to the substrate. High-resolution N 1s and B 1s spectra (Figures 38b-c) show the usual peak shapes, centered at 398.6 and 191.2 eV, respectively. The atomic percentages are 21.2% and 25.7%, for N and B, respectively. These measurements agree with other studies for CVD hBN [84,123].

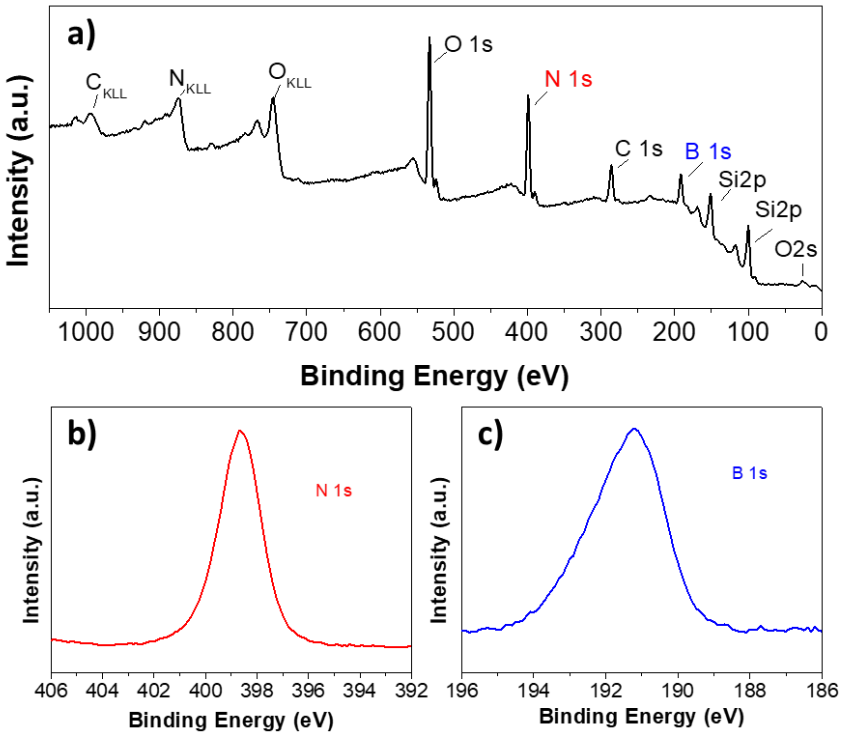

Figure 38. a) XPS survey of hBN film over a substrate. b) Nitrogen and c) Boron XPS spectra, respectively.

4.4 SPE performance

As referred, hBN appears as a viable platform to produce bright and optically stable SPEs at room temperature, actively sought for quantum technologies. In order to ascertain the viability of the grown hBN samples as SPE sources, their fluorescence emission properties were investigated.

TIRFM and confocal images collected are shown in Figures 39a-c. SPE signatures appear as intensity spots with a shape matching the point spread function (PSF) of the microscope. This match was further verified by performing Gaussian fittings of the intensity profiles across individual spots. The measured full-width at half maximum (FWHM) is 218±18 nm (inset in Figures 39c). The value matches the diffraction-limited spot size of the microscope (i.e., 220 nm). Interestingly, the intensity spots show deviations from a circular shape only: They appear also as half circles and single lines/stripes (white and magenta arrows, respectively, in Figures 39c). These shapes are usually indications of "blinking", i.e., a fluorescence intermittency due to emitter transitions between long-lived (ms to s) dark and bright states [124]. The different spot shape is thus determined by the average duration of the bright and dark states, due to the laser scanning nature of the confocal measurement. The intermittent blinking processes appear as deviations from circular intensity spot patterns in the fluorescence intensity images and are a good indication of the SPE density originating in these locations [125]. Blinking is generally undesirable, since

highly stable emitters are required for any operating SPE device [30]. This behavior, observed also in single molecule and quantum dot emitters, still needs to be fully understood. The suspected cause behind blinking is random environment dependent fluctuations of the local electric field of surface defects; this situation has then motivated strategies such as substrate passivation and encapsulation to enhance the SPE stability [126].

SPE density was analyzed by determining the number of well-isolated diffraction-limited spots per unit area in widefield TIRF fluorescence images. In this way, the values reflect the density of SPEs usable in quantum photonic applications, where addressing individual emitters is crucial [127]. The sample has an emitter density of 0.09±0.01 emitters/μm^2, corresponding to a mean distance between emitters of 3.25±0.21 μm. In literature, the SPE density reported for CVD samples varies significantly: Some groups reported densities as low as 0.04 emitters/μm^2 [126], while others as high as 2.2 emitters/ μm^2 [124]. The SPE density from our TIRF data fit well within this range. Dense SPEs could be key elements for the fabrication of efficient quantum photonic devices; however, too high densities may pose challenges for the isolation and control of the individual emitters. The SPE density and position could be controlled by focused ion beam (FIB) nanomachining, which yielded densities of 0.33 emitters/μm^2 at deterministic positions [125]. Our APCVD hBN showed SPE densities of similar magnitude, allowing a good separation between individual SPEs, without the need of any post-processing treatment.

Our hyperspectral confocal microscope images provide spectrally resolved fluorescence emission information. Several categories of spectral fingerprints associated with the pixel colors in the images were analyzed. The signature emission peaks (typically referred to as zero phonon lines – ZPL), appearing in most images at ~538, 582, and 617 nm, were used to analyze the images (Figures 37d). In a minority of images, the ZPL positions appeared slightly shifted from the rest, probably due local strain in the hBN film, as reported in recent studies [128]. Similarly large spectral ranges were also previously reported [129]. Several replica peaks were observed, typically called phonon side bands (PSBs), whose energy difference from their respective ZPL is $\Delta E = 159.8 \pm 12.5$ meV, in agreement with the literature [124].

Thus, considering the PSF shape as an indication of a single dipole emitter, the matching spectral signatures for hBN that are similar to those reported in literature, and the fact that the emission is persistent over long excitation times, there is a strong evidence that the grown hBN films could act proficiently as SPE material.

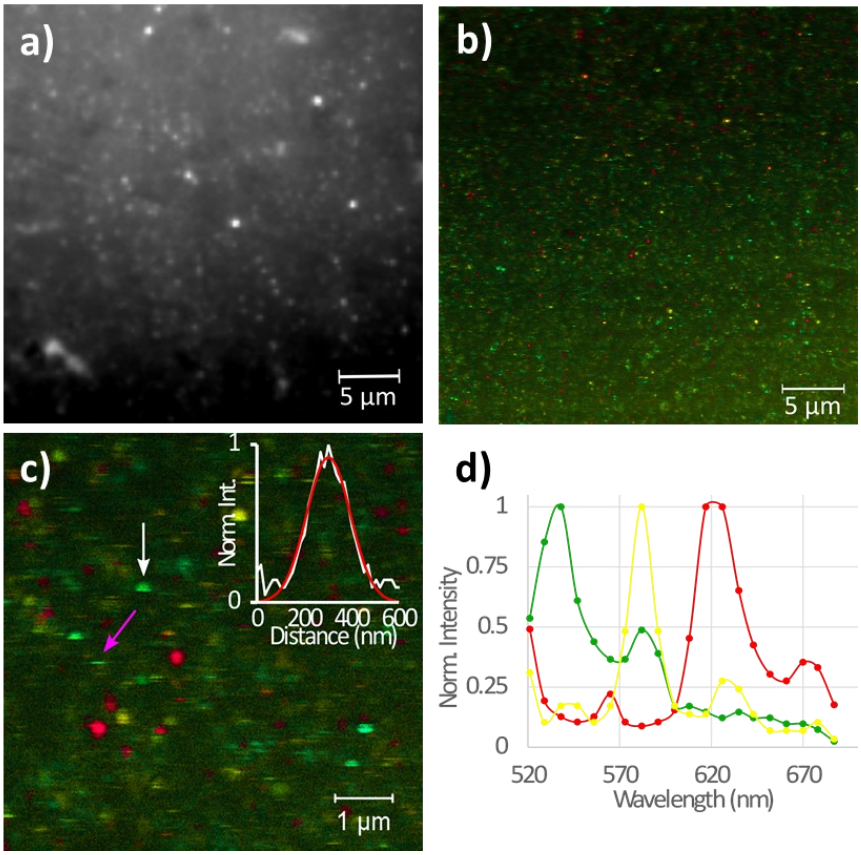

Figure 39. a) Fluorescence intensity image as observed by TIRFM. b) Hyperspectral confocal fluorescence image. c) zoomed-in confocal fluorescent image with inset illustrating the intensity profile of one fluorescent spot and its Gaussian fitting. d) reveal the most representative spectra observed in each sample.

4.5 Conclusion

2D hBN is an emerging material suitable for several technologies, in particular photonics and optoelectronics. However, a method that would guarantee a large-scale, high-quality and low-cost production is still needed. During the course of this thesis the goal of optimizing an APCVD system for production of this material was successfully achieved. First, cleaning the Cu substrate with a specific aqueous solution (composed of 280ml of DIW, 10 ml of HCl 37% and 2.5ml of 2M FeCl3) revealed to be beneficial. Still regarding the substrate, Cu annealing is crucial in order to have proper hBN growth. Furthermore, the AB pre-treatment was tuned and the optimal output was achieved using 100°C over 150min under 15scmm flow. Also, the distance between the precursor and the substrate was studied and 45cm proved to be optimal. Lastly, the role of growth time in the resultant thickness was investigated and a 30min growth was adopted. This optimized APCVD process allows to grow hBN films with high reproducibility. After the growth, the films were transferred to target substrates for a wide range of characterizations. The extensive characterization revealed few-layer, polycrystalline hBN films (~3 nm

thickness) with balanced stoichiometry and uniformity over large-areas (i.e. up to 20cm^2). Besides that, nm-sized SiO_x particles were noticed on top of the films, as reported for CVD growth of graphene. The viability of our APCVD hBN as prospective SPE platform was studied. Two highly sensitive fluorescence microscopy techniques (i.e., total internal reflection and spectrally resolved confocal) were used to this end. Individual and widespread SPEs were measured, which shared comparable spectral properties and same order of densities when compared to literature. This suggest the prospective use of the APCVD hBN films in quantum photonic applications. Thus, although the use of LP is usually associated with a higher hBN quality (along with higher control in thickness and uniformity), the optimized procedure allows to achieve an analogous sample quality by a more versatile approach. Overall, this method entails lower operating and maintenance costs, more suitable for industrial purposes.

5. GROWTH OF 2D $MoSe_2$

5.1 Materials and methods

$MoSe_2$ was grown by CVD in a 3-zone split, 4"-diameter quartz-tube furnace (TermoLab) using Ar/H_2 gases at atmospheric pressure, as shown in Figure 40.

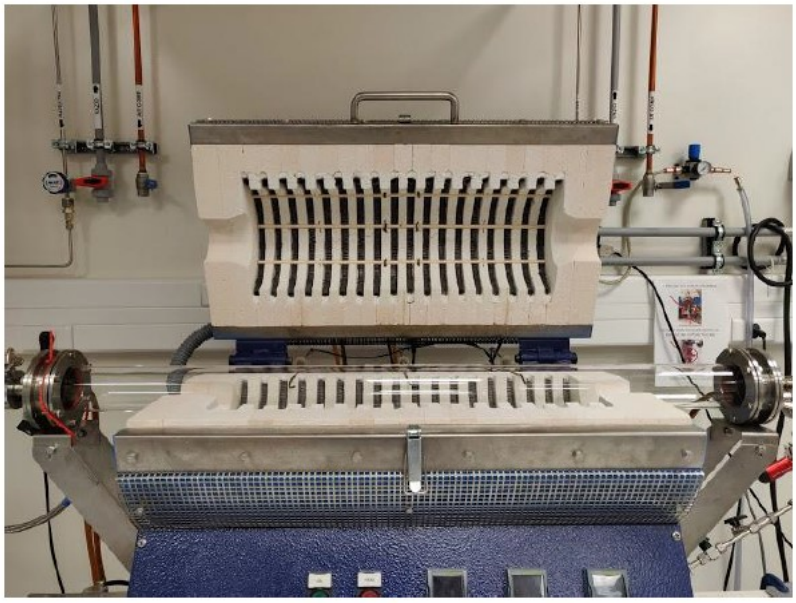

Figure 40. $MoSe_2$ furnace at INL.

Se powder (99.999%, Alfa Aesar) and Mo foil (0.025mm thick, 99.95%, Alfa Aesar) were used as precursors. Substrates and Mo foils were cleaned before the process in an acetone, IPA and DIW individual baths in ultrasound for 10 minutes. The Mo foil was folded to form a bridge-like structure surrounding the borosilicate glass slide substrate and keeping a gap of 0.5/0.7/1cm (Menzel-Gläser, 100 OT). The boat containing 250 mg of Se was kept upstream, 30/45 cm apart from the growth region, as depicted in the schematic from Figure 41. Before deposition, a 45min purge under 200sccm of Ar was done. Then, the furnace substrate region was set to the growth temperature (650°C/720°C/770°C) at a rate of 20°C/min. When the growth temperature was achieved the atmosphere was set to the specific Ar(45/50/55sccm)+H_2(15/10/5sccm) flow. After 12/20/30min min growth, the furnace was turned off and the lid opened to ensure a quick cooldown. The temperature timeline for the furnace is illustrated in Figure 42.

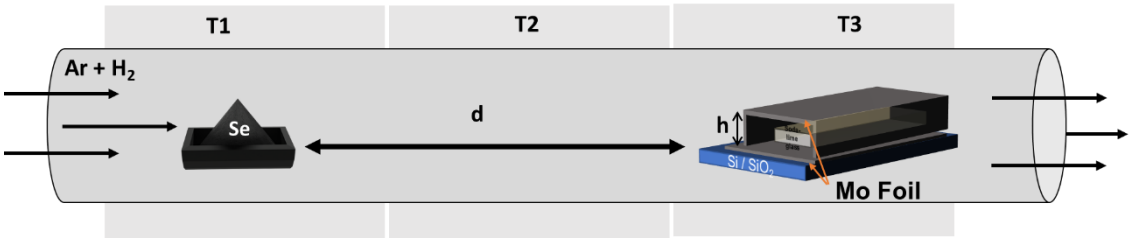

Figure 41. Schematic illustration of the experimental setup utilized for the synthesis of $MoSe_2$.

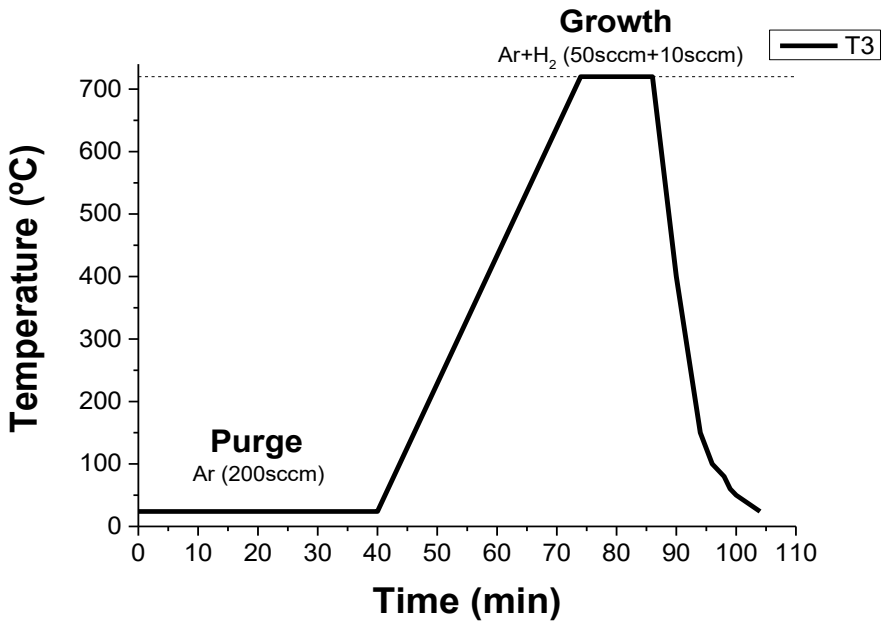

Figure 42. Temperature timeline for the $MoSe_2$ furnace.

The transfer of samples grown on glass substrate was done via an adapted method from Castellanos-Gomez et al. and Ma et al. [130]. A beaker with DIW was preheated to 90°C and a commercial viscoelastic PDMS film (PF Gel-film from Gel-pak) cut into the desire shape. After the PE coversheet was removed, the gel material was then exposed to water vapor for 5-10 seconds and quickly placed on top of the surface of the substrate with $MoSe_2$, gently removing air bubbles and assuring a good contact between the gel and substrate with the tip of a cotton swab. After peeling the film from the substrate, the capillary forces assist the transfer and the 2D material is released from the glass to the PDMS surface and then inspected under a microscope. The PDMS+$MoSe_2$ stack is then held with tape on a glass slide in a cantilever-like configuration and fixed to an XYZ micromanipulator, ensuring a deterministic transfer to the target substrate with an optical microscope. This technique allows the dry-transfer of 2D materials without the need of etching chemicals, hence it has a low contamination risk, while at the same time being precise and compatible with several types of substrates, such as TEM grids, where low

contamination levels are critical to acquire images and correct data analysis. A schematic illustration of the process is shown in Figure 43.

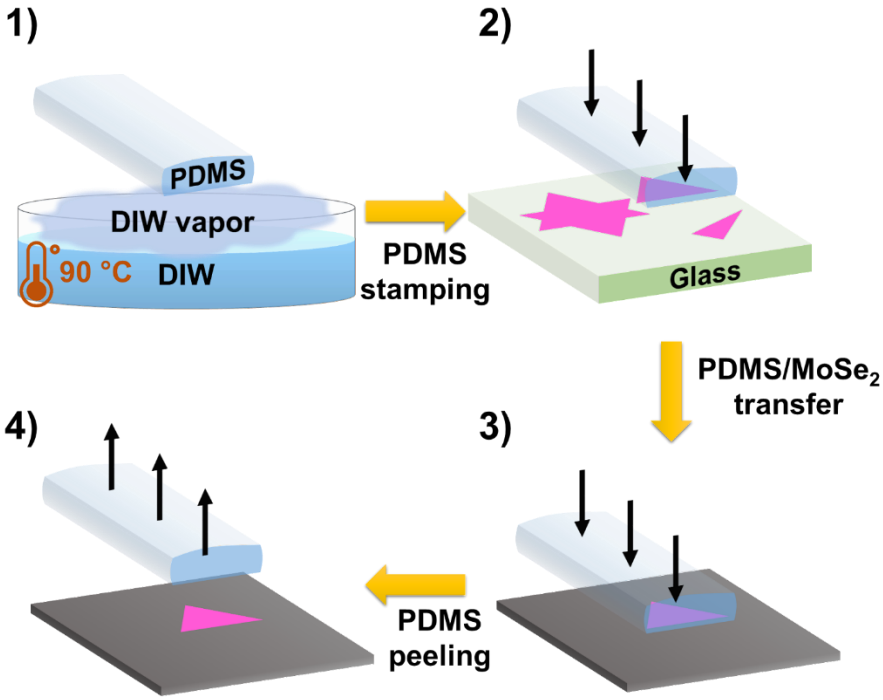

Figure 43. Schematic illustration of the PDMS transfer.

5.2 Parameters and optimization

5.2.1 Mo foil gap

The Mo foil, placed above the substrate, serves as Mo homogeneous supplier for the growth of $MoSe_2$. Besides that, $MoSe_2$ flakes shape and size are tunable by controlling the gap distance between the Mo foil and the substrate [131]. To explore these phenomena, during the experiments the gap between the Mo foil and the substrate was adjusted, ranging from 0.5-1cm. The different outputs are shown in Figure 44. Figure 44a shows an OM image of the sample grown with a 0.5cm gap. As visible, several flake morphologies (mainly triangular-shaped) as well as different thickness zones (with bright zones meaning increased thickness) are noticed. When the gap was increased to 0.7cm the nucleation density dramatically decreased and larger flakes, mainly monolayer, were grown. It is worth to mention that flake shape seriously changed. Lastly, further increasing in the gap distance was revealed to be prejudicial. Although the nucleation density remained similar, the flake size decrease significantly, and some few-layer zones started to reappear. Again, a variation in flake shape was noticed. Thus, the optimal gap distance is shown to be around 0.7cm.

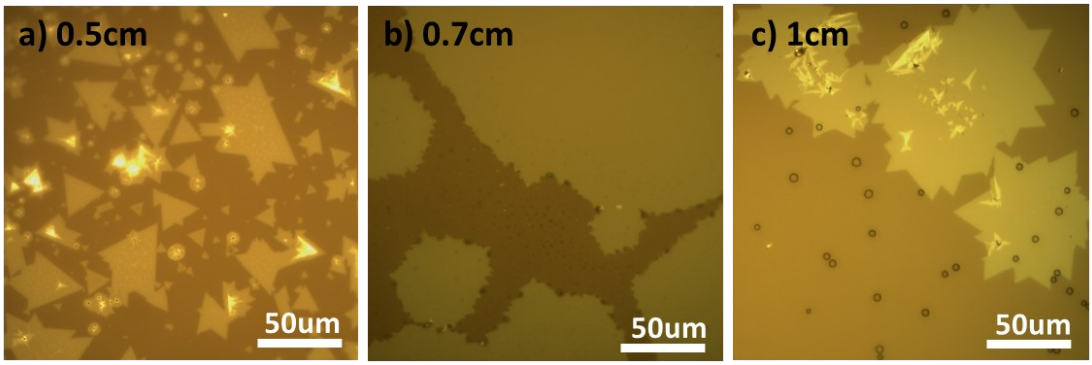

Figure 44. Optical microscope images of the flakes grown with a) 0.5cm, b) 0.7cm and c) 1cm gap between the substrate and the Mo foil.

Besides the flake shape dependence with the gap, it is worth mentioning that several flake morphologies are noticed in each sample (depending on substrate region). This may be explained in the first instance due to the geometry used in the growth zone: the lateral sides of the glass are near the walls of the Mo foil bridge while the back and front parts are left open (Figure 41). As consequence, the Mo supply in the laterals should be somehow different. This will affect the Mo:Se ratio and therefore the flake morphology. In addition, on the laterals, the Mo concentration should be higher leading to higher flake density. Overall, the way in which the Mo foil oxidizes Is uncontrolled so the release of Mo releases during the process is somehow unpredictable and could affect the flake morphology.

5.2.2 Distance between substrate and Se powder

Another crucial parameter throughout the process is the distance between the Se powder and the growth zone, where the substrate (and the Mo foil) are located. As referred, the furnace has three independent temperature zones, but obviously there can be a gradient temperature along the tube (when using temperature above a certain threshold). For this study, the position of the Se powder boat was kept and the substrate was moved. Since precise temperature control is needed in the growth zone, two points were tested, having the substrate placed in the second and third zone of the furnace (allowing perfect alignment with the thermocouples). It is worth mentioning that, further than changing the distance, the Se powder temperature will be affected, because if the powder is kept closer to the growth zone it will achieve a higher temperature. This will automatically affect Se powder evaporation rate and consequently the amount of Se precursor reaching the reaction zone. Figures 45a-b show OM images of the samples grown with 30 and 45cm gap, respectively. Micrometer-sized flakes with similar shape were achieved in both cases. For 30cm gap the flakes show few-layer zones/particles near the edges while for 45cm gap the grown flakes look predominantly monolayer. Besides this, the Raman spectrum of each sample is illustrated in Figure 45c. Raman spectrum of the first sample reveal the characteristic A_{1g} peak from $MoSe_2$

and a strong peak near ~250cm^{-1}, which is a Se vacancy induced defect mode[132]. The defective behavior of the first sample may be explained due to the higher T of Se. As Se powder temperature powder increases, Se evaporates first leading to Se-deficient precursors during the process that are responsible for the growth of defective crystals. On the other hand, the sample grown with a 45cm gap displays a perfect monolayer $MoSe_2$ kind of spectrum. Therefore, a distance of 45cm proved to be optimal.

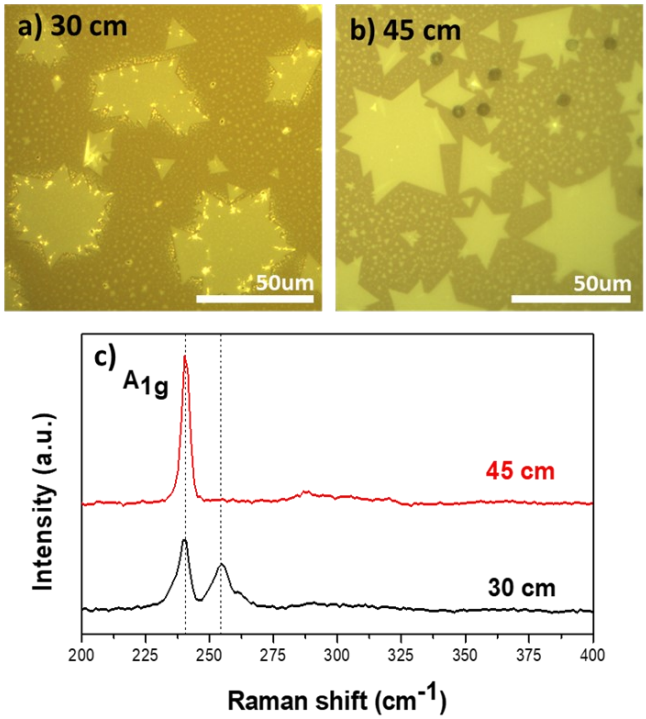

Figure 45. Optical microscope images of the flakes grown with a) 30cm and b) 45cm between the Se powder and the substrate. c) Raman spectrum of each film.

5.2.3 H_2 influence

H_2 is known to have a crucial role in $MoSe_2$ CVD growth. It should not only increase the chemical reactivity of chalcogenides, but also hinder the deposition of intermediate metal oxides. Furthermore, at high flow rates, H_2 can also assist the suppression of vertical growth through an etching effect, aiding the deposition of monolayer materials. With this being said, the ratio of Ar/H_2 gas mixture influences drastically the shape and quality of $MoSe_2$ crystals [96]. During this work, the influence of H_2 was investigated. This was performed by changing the concentration of H_2 in the flowing gas, keeping constant the total gas flow (60sccm). Figures 46a-c show OM images of the grown films while Figure 46d displays the representative Raman spectrum of each sample. Initially, a flow mixture of Ar(45scmm)+H_2(15scmm) was tested (Figure 46a). It is possible to see that the growth conditions gave rise to random shaped/sized flakes. The respective Raman of the sample shows that, besides the strong A_{1g} vibration mode from $MoSe_2$, there is

also an additional peak located at ~250cm^{-1}, which is directly related to Se vacancies, as reported somewhere else [106]. Lowering the H_2 concentration reduced the nucleation density and enlarged the flake size (although the randomness in shape and size remained). However, the biggest difference was noticed in the representative Raman spectrum: reducing hydrogen helped soften defects peaks and strengthen A_{1g} vibration mode, in accordance with the literature [107]. This can be explained be the fact that H_2 has an etching effect on the CVD growth of $MoSe_2$ which mean that higher H_2 concentration could led to more intense defect peak. Finally, a further reduction of H_2 concentration gave rise to the reduction in flake size whereas the nucleation density increased dramatically. Regarding the representative Raman spectrum, A_{1g} vibration mode intensity and the position remained unchanged. Thus, the optimal flow seems to be Ar(50sccm)+H_2(10sccm).

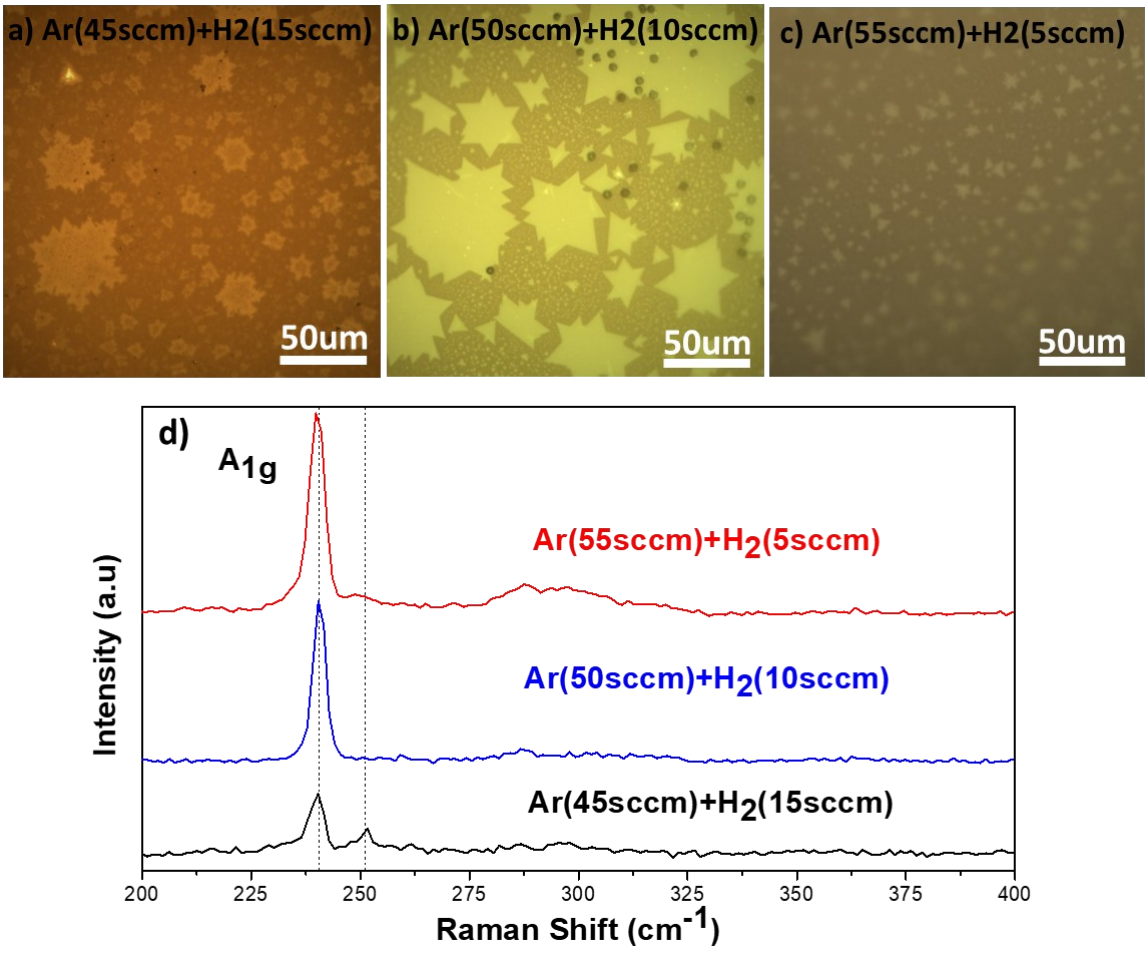

Figure 46. Optical microscope images of the flakes grown with a) Ar(45sccm)+H_2(15sccm), b) Ar(50sccm)+H_2(10sccm) and c) Ar(55sccm)+H_2(5sccm). d) Raman spectrum of each film.

5.2.4 Growth temperature

Growth temperature is crucial during the process since it directly influences the nucleation density and the grain size [109]. Nevertheless, the growth temperature must be compatible with the substrate used. We chose borosilicate glass substrates, due to a low cost and possible scalability. The main drawback is represented by a reduced temperature range, since the glass could melt or be structurally compromised (above 736°C from supplier's technical specifications). Three temperatures were tested: 650°C, 720°C and 770°C. Figure 47a show the substrates after each run. In the first case, although the glass maintained its original structure, no sign of $MoSe_2$ was detected. When the temperature was increased to 720°C, $MoSe_2$ flakes were found on the substrate, but a bending in glass was noticed (mainly in the borders). Lastly, at 770°C the substrate completely melted, although $MoSe_2$ growth was noticed. Figure 47b shows the Mo foils after each procedure. As visible, different color tones are noticed which may be related to different oxidation states achieved at the different temperatures. We aimed at preserving the original surface morphology of the glass substrate, thus providing higher potential for a batch production: for this reason, the growth temperature was set to 720°C for the next experiments. Nevertheless, it is worth mentioning that molten glass has been also proposed as substrate for $MoSe_2$ growth [109].

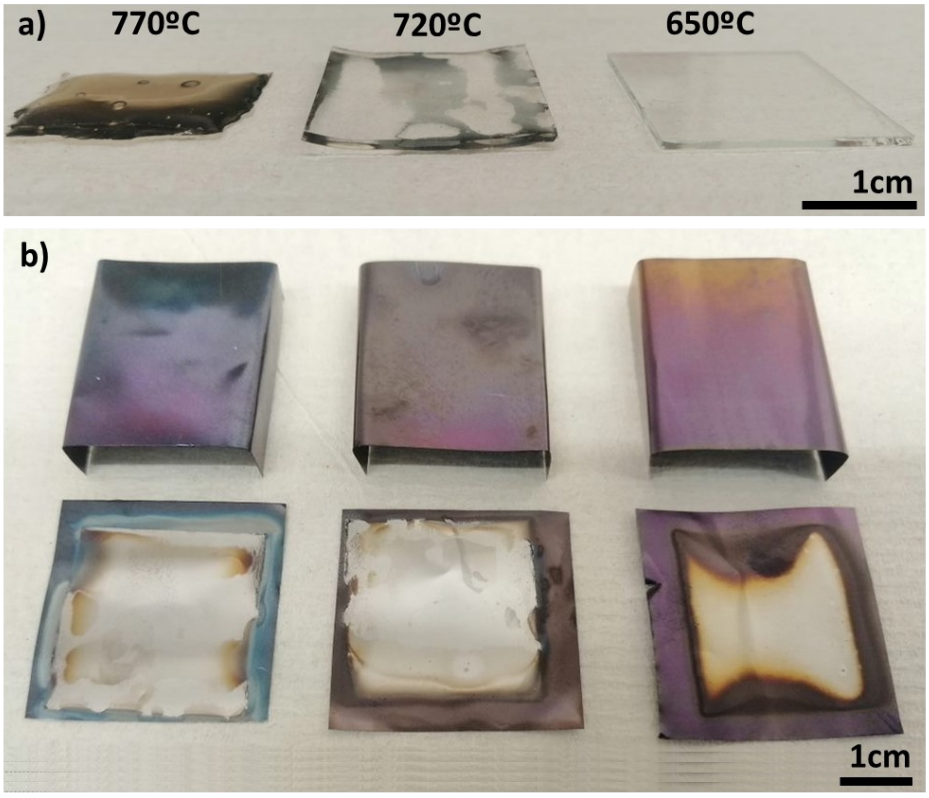

Figure 47. a) Photograph of the glass substrates after process. b) Photograph of the Mo foils after process.

5.2.5 Growth time

The process time has a critical role in $MoSe_2$ growth. Identifying the ideal process duration can allow the lateral growth of the grains into continuous films [131]. However, a too long duration may as well induce vertical growth of the 2D TMDC, which should be avoided [133]. In an attempt to attain 2D $MoSe_2$ over large areas, several growth times were investigated: 12min, 20min and 30min. Figures 48a-c show OM images of the samples, grown at increasing times. As expected, the lateral size of the flakes increases with time. However, the presence of multilayer zones also increased, allows us to conclude that vertical growth becomes dominant after 20min. Figure 48d illustrates representative Raman spectra for monolayer and few-layer zones. A_{1g} vibration mode for monolayer region appears at 240.5 cm^{-1}, while it blue-shift to 242.3 cm^{-1} for the sporadic crystal regions with increased thickness (few-layer). E^1_{2g} undergoes a red-shift when passing from a monolayer to a few-layer zone. The absence of the B^1_{2g}mode is also an indicative of the monolayer regions of the sample. Therefore, a 12 min growth was adopted in order to achieve monolayer flakes.

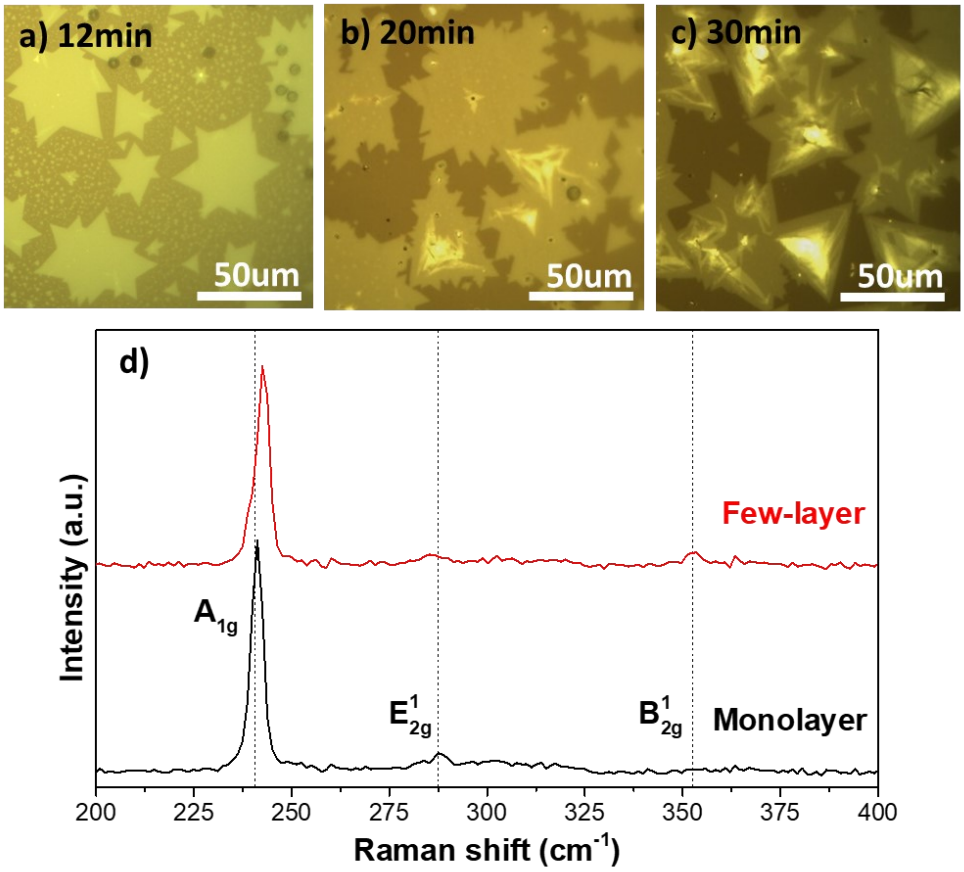

Figure 48- Optical images of the flakes grown with: a) 12min, b) 20min and c) 30min. d) Raman spectrum of each grown film.

5.3 Characterization of the optimized sample

The optimized samples show localized $MoSe_2$ growth, mostly near the borders of the glass substrate, as shown in Figurer 49a. Figure 49b shows a region where $MoSe_2$ flakes coalesced to form large crystals and. A μm-sized film can be identified in the top corner after complete coalescence of the flakes. Besides, small particles surrounding the edges and in the center of the bare substrate are highlighted by the black arrows in Figure 49c). As proposed by Li et al., these could be metastable nanoparticles that act as an intermediate reaction compound, serving as feedstock of both Mo and Se for the formation of the $MoSe_2$ layer [134]. The analysis of the Raman spectra shown in 49d) reveals the monolayer nature of the flakes with the A_{1g} mode at 240.5 cm^{-1} that is blue-shifted to 241.7 cm^{-1} for the sporadic crystal regions with increased thickness (few-layer). As before, E^1_{2g}exhibts a red-shift when going from a monolayer to a few-layer zone. The absence of the B^1_{2g}mode is also an indicative of the monolayer regions of the sample. PL emission from the sample was also measured (Figure 49e). A peak centered at ∼790 nm for the monolayer region and a lower intensity and broader peak with a slight redshift to ∼785 nm for bilayer-layer appear, as expected with the increase of thickness [111]. Interestingly, the peak position at lower-than-expected wavelength for a monolayer may be caused by compressive strain in the flakes, as mentioned before. This hypothesis is backed up by the systematic study on the strain of $MoSe_2$ conducted by Cheng et al. [135]. AFM was used to determine the thickness and roughness of the samples. These generally consist of isolated and not fully coalesced flakes with a thickness of ∼1.0 nm (Figure 49f). The difference from the expected value for a monolayer (∼0.7 nm) might attributed to the surface of the glass becoming uneven after being exposed to thermal range required for the growth. AFM also reveals that the sample exhibit thicker particles in the center of the flake and small particles and triangular nanosheets are visible in the edges, similar to the reported precipitation of liquid Na-Mo-O droplets around the dendritic-shaped $MoSe_2$ flakes grown by Wang et al. [108].

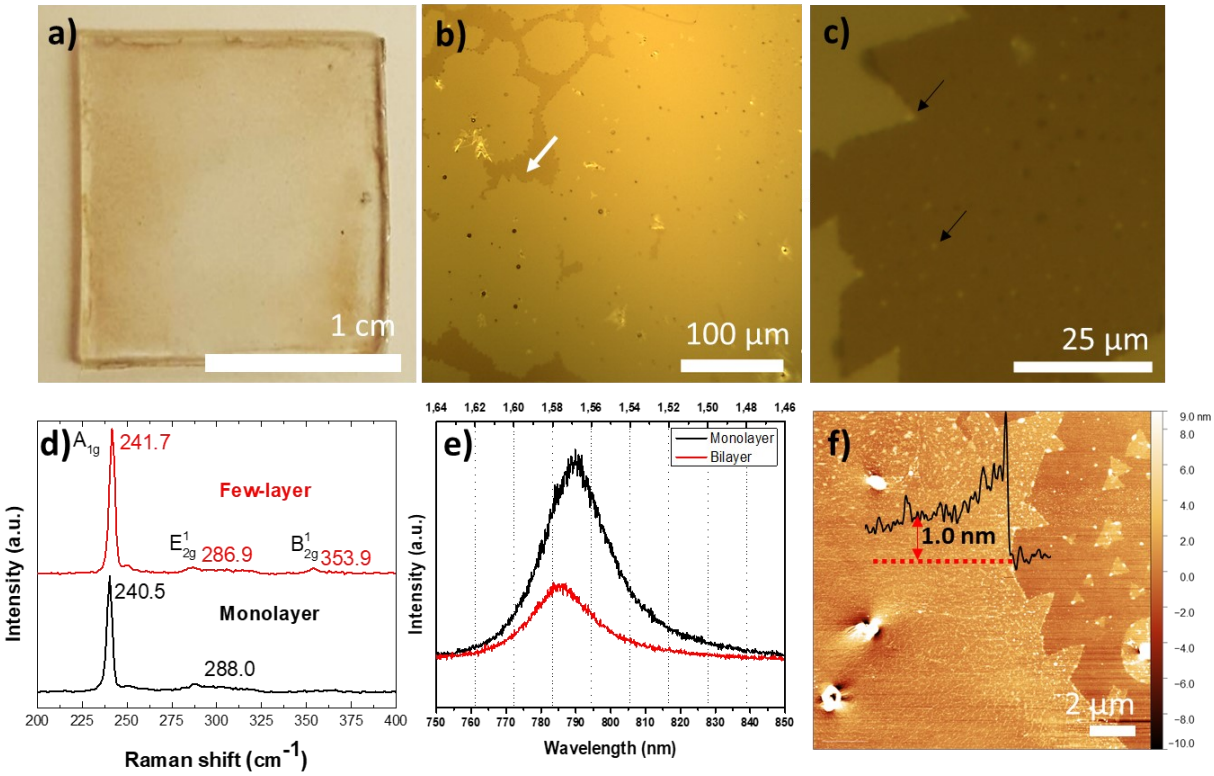

Figure 49. a) Photograph of the glass substrate after grow. b) Optical image of the $MoSe_2$ flakes on glass, mostly monolayer with sporadic bi-layer and few-layer nucleation spots. c) Optical image of the zone highlighted by the white arrow in panel b), with visible particles nearby the surrounding of the flake edges and in the bare substrate, as pointed by the black arrows. d) Raman spectra of the sample. e) PL spectra of the sample. e-f) AFM image of the sample, measuring a thickness of ~1 nm.

TEM imaging was employed to further characterize the atomic structure of the samples. Figure 50a shows triangular shaped crystals of $MoSe_2$ with a lateral size of ~6.5 µm. Besides that, nanoparticles were randomly formed together with the $MoSe_2$ crystals, as shown in Figure 50b (highlighted by the white arrow). In some cases, these nanoparticles are located along defects in $MoSe_2$ crystals (Figure 50c). As mentioned, most of these defects (Figure 50d) are due to vacancies in the $MoSe_2$ layers.

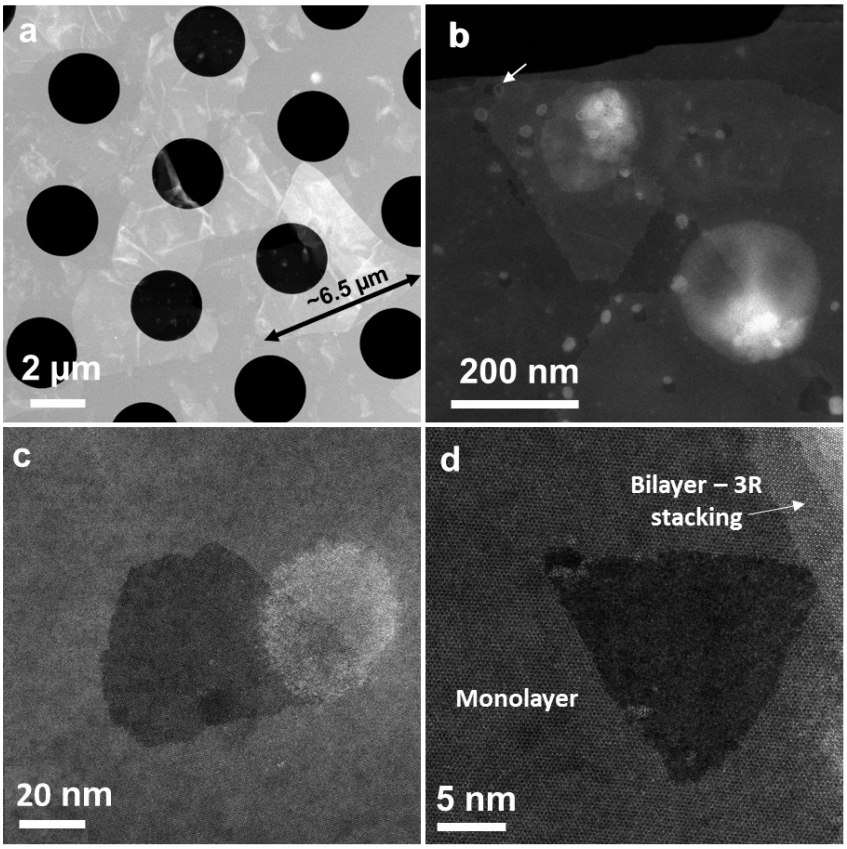

Figure 50. a) HAADF STEM image showing the triangular shaped $MoSe_2$ crystals with lateral size of ~6.5 µm. b) HAADF STEM image of nanoparticles randomly distributed within the $MoSe_2$ crystals. c) Higher magnification HAADF STEM image showing the presence of defects next to the nanoparticles. d) Higher magnification HAADF STEM image showing the hole in monolayer $MoSe_2$.

To ascertain the chemical composition of these nanoparticles, HAADF STEM imaging, coupled with Energy Dispersive X-ray spectroscopy (EDS) was performed (Figure 51). Due to a higher concentration of Na, O and Se detected within the round-shaped particles suggests that the detected nanoparticles could be made of sodium selenite (Na_2SeO_3) [136]. The Mo distribution is uniform in the analyzed region meaning that the $MoSe_2$ flake has a balanced stoichiometry. It is noteworthy that the Na-containing particles (originating from the glass substrate) were detected also after the transfer from the original substrate to the TEM grid, meaning that they become embedded into the $MoSe_2$ flake structure.

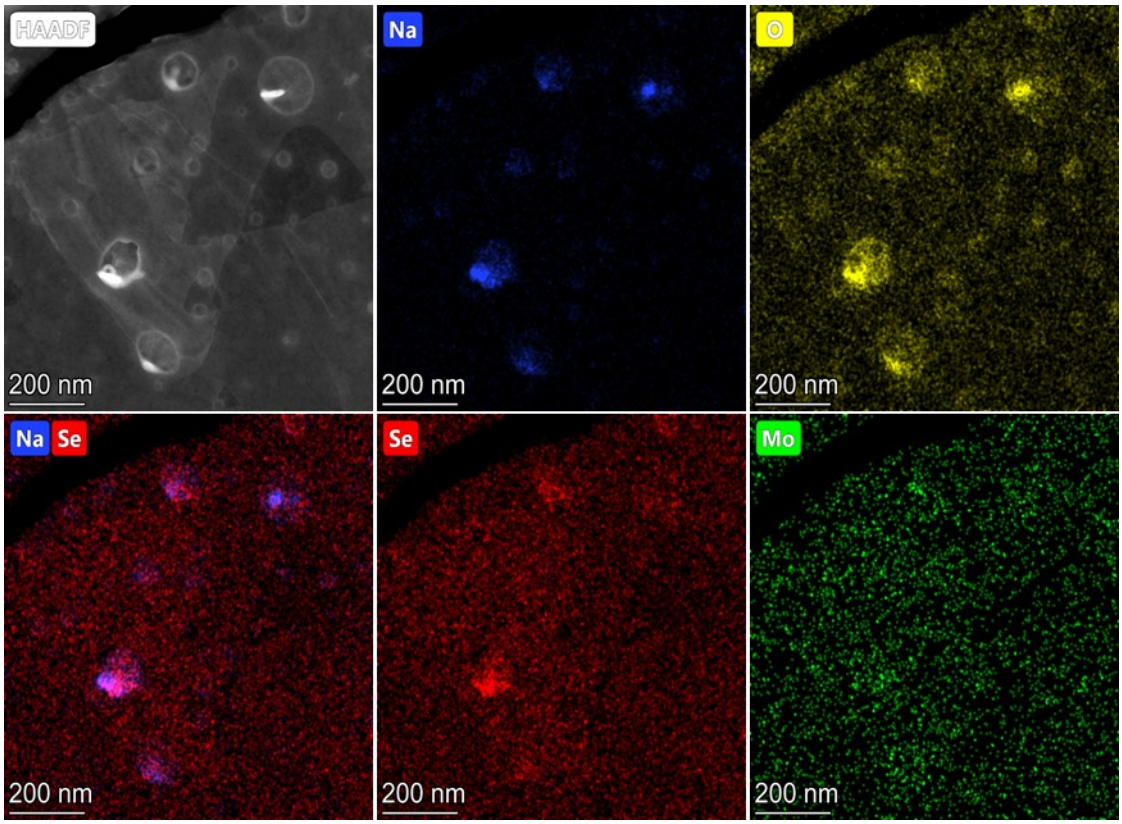

Figure 51. HAADF STEM image of MoSe2 crystals grown and chemical EDX maps of the various species.

Lastly, XPS was done to provide information on the elemental composition and chemical status of the grown flakes. The stoichiometry and bonding state of Mo and Se atoms was studied in detail, and the potential presence of heterogeneous phases was carefully ascertained. In the XPS analysis of an atomically thin sample, the substrate and the sample processing may have an undetermined effect on the measurements. This is even more subtle for CVD samples, which need to be grown on specific, fixed substrates. Therefore, two samples were characterized: $MoSe_2$ flakes on the original substrate (glass) and after a dry-transfer to a Si substrate. The respective surveys are shown in Figure 52a). The C1s and O1s signals observed derive from air exposure. For the transferred sample, the carbon signal can be also assigned to the species related to the PDMS transfer. Se/Mo concentration ratio is ~2.4-2.6 for the samples, which correlates quite well with the $MoSe_2$ stoichiometry given the rather large data scattering in the concentration quantification. The potential presence of Na (arising from the substrate) in the samples was carefully evaluated too. Marked Na1s and NaKLL peaks appear in the Na samples measured by XPS on the very glass substrate, clearly stemming from the Na contained in the glass. When the same sample was dry-transferred to a Si substrate and measured, a small Na amount could be still detected (Table 3). This means that the Na released from the glass during the growth not only participate to the gas phase reaction but might as well end up embedded as tiny particles (perhaps of heterogamous

content) within the growing crystals. The binding energy of the Na1s peak at 1070.8 eV is similar to reported values for Na_2SeO_3 [137,138], in agreement with the HAADF STEM elemental analysis (Figure 51) that shows particles containing Na, Se and O. Figure 52b shows the high-resolution spectra for Mo3d region. The Mo3d range consists of two spin-orbit components, overlapping with the Se3s peak (at ~229 eV). Mo3d spectra were fitted using two peaks at ~228.5 and ~231.7 eV: Those correspond to $Mo3d_{5/2}$ and $Mo3d_{3/2}$ (with constraint for intensity ratio $Mo3d_{5/2}$:$Mo3d_{3/2}$=3:2). One peak was added to fit the Se3s contribution. Figure 52c shows the high-resolution spectra for the Se3d spectra region (~54.3 eV). The Se3d range can be deconvoluted into two peaks corresponding to the $Se3d_{5/2}$ and $Se3d_{3/2}$ spin-orbit components. Thus, the deconvolution of the Mo3d as well as the Se3d with only one set of spin-orbit peaks evidences the formation of virtually oxygen-free $MoSe_2$ samples. The sample revealed binding energies around 54 and 55 eV for the $3d_{5/2}$ and $3d_{3/2}$ peaks, respectively. These values are congruent with the literature for the energy binding position of 2H $MoSe_2$ [42,99,139,140].

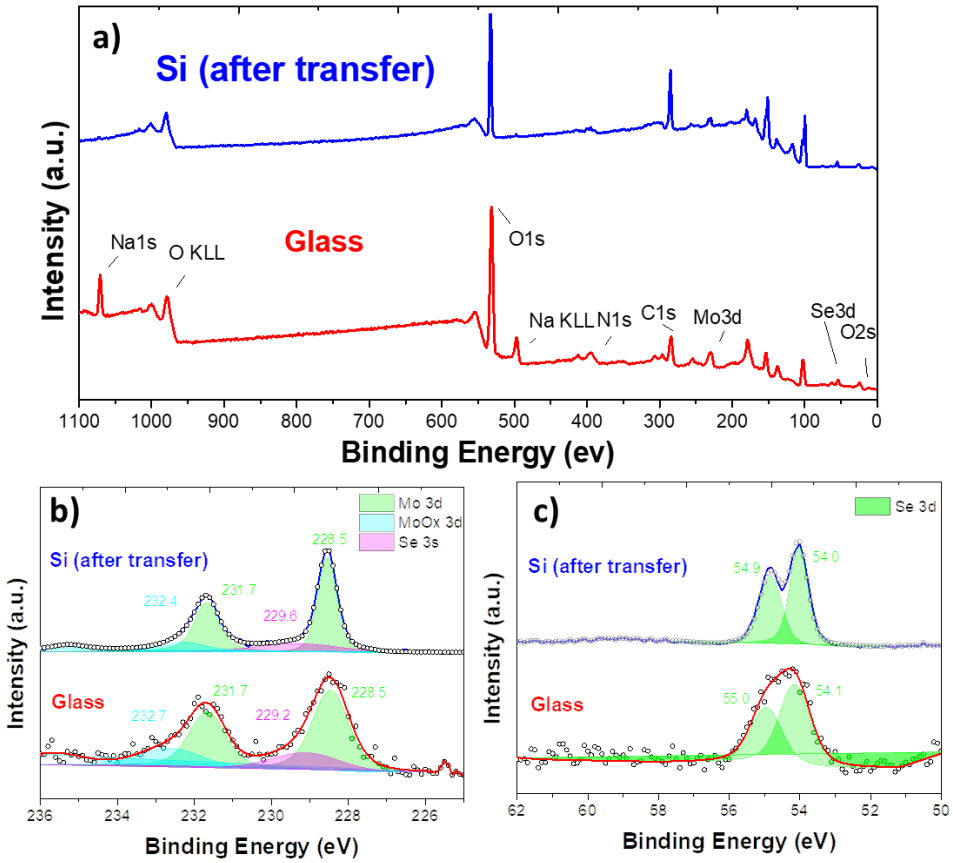

Figure 52. a) XPS survey spectra of the sample on the original glass and after transfer to a Si substrate. b) and c) High-resolution spectra for Mo 3d and Se 3d before and after transfer.

Table 3- Elemental composition in at% of the samples, as given through XPS.

	Mo ($MoSe_2$)	Mo (MoO_x)	Se	O Oxide; SiOx	Si (SiO_x, x≤2)	C	Na
Si (after trasnfer)	0.5	0.1	1.3	29.9	15.4	31.2	0.3
Glass	1.0	0.45	2.4	47.2	21.4	21-22	5.6

5.4 Uniaxial tension studies

The possibility to tune and enhance the physical properties of 2D TMDCs by strain engineering seems very appealing since it may cause a breakthrough in flexible nanoelectronics and optoelectronics. Among these materials, 2D $MoSe_2$ is known to have superior physical properties so understand its behavior under strain is pivotal in order to aim its integration into practical flexible applications. There are several ways to induce strain to 2D materials such as lattice mismatch—the use of different substrates, such as flexible substrates, patterned substrates, and piezoelectric substrates—, the action of atomic force microscope (AFM) tip or bubbles. However, the most straightway to do it is by using flexible substrates with high Young's modulus (such as PET or PDMS) that are able to directly apply strain on the upper surface of 2D materials by bending with external force. By controlling the flexible substrates to be bent up or down, tensile or compressive strain is induced in 2D materials, corresponding to positive or negative strain values, respectively. The amount of strain can be estimated by:

$$\varepsilon \approx \frac{t}{2R} \quad (1)$$

where t is the thickness of the flexible substrate and R the bending radius [141].

In this work, strain inducing experiments (by applying uniaxial tensile strain) were performed on the grown $MoSe_2$ flakes. For this, the flakes were transferred to a PDMS and the setup illustrated in Figure 53a was used. Raman and PL measurements were acquired in four different strain stages - starting from flat up to extra bent and coming back to the flat again position, in this order. By the use of formula (1) it is possible to estimate the amount of strain induced in the flakes. In this case the thickness of the PDMS used is 292μm (t) while R is 6 cm and 4 cm (measured in ImageJ software) for bent and extra bent stages, respectively. This gives strain values in the range 0%-0.4%. Figure 53b shows the grown $MoSe_2$ flakes after dry-transfer to a PDMS stamp. Due to the transfer, the flakes ended up damage, so an intact area was chosen for the measurements. Raman analysis of the flakes was performed during the different strain stages. As visible in Figure 53c, Raman spectra remains unchanged no matter the strain the flake was experiencing, with the A_{1g} vibration mode showing up at 240.5 cm^{-1}, as expected for monolayer. Besides that, PL performance under different strains was acquired (Figure53d). When moving the apparatus from a flat to an extra stage, i.e, increasing the strain from 0% to 0.4% a red-shift in PL position

is noticed. Finally, moving the apparatus down to the flat position again PL position is blue-shifted, matching the initial position. This shift in PL position can be assigned to changes in the electronic band structure of the material. Under tension, the lattice parameter of the material changes which affects its electronic band structure and gives rise to a new bandgap energy (different PL position). During signal acquisition it was hard to always keep the same focus on the microscope (due to bending) which hardly affects PL Intensity, therefore PL intensity comparison for different strain stages is not reliable. These PL shifting observations are in line with current literature. Several reports on strain engineering agree that PL emission on $MoSe_2$ flakes steadily shifts toward lower energies for higher strains, indicating a reduction of the band gap [55,56,135]. Thus, these studies are an experimental evidence that the optical properties of the $MoSe_2$ flakes, in particular PL emission, are tunable by strain engineering which turns the material suitable for flexible optoelectronic devices.

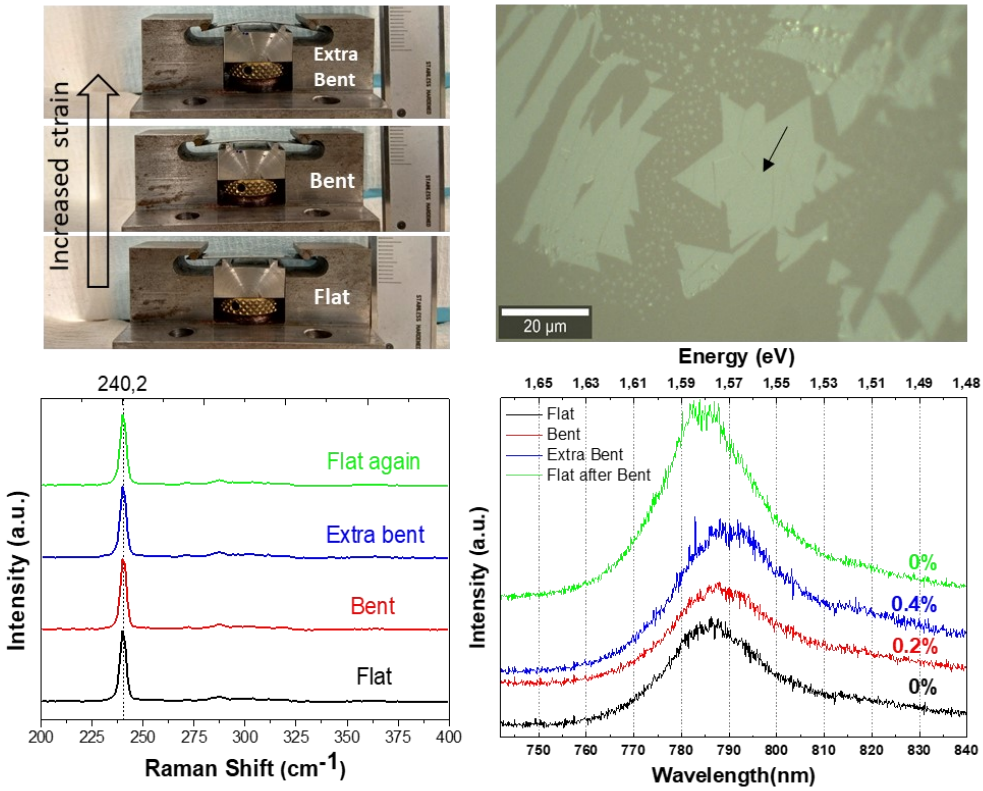

Figure 53. a) Setup used to induce strain on the $MoSe_2$ flakes. b) Optical microscope image of the $MoSe_2$ flake. c) Raman and d) PL spectra for the different strain conditions.

5.5 Conclusion

2D $MoSe_2$ is a promising semiconductor belonging to the family of TMDCs which demonstrated novel optoelectronic properties. However, the lower chemical reactivity of Se and higher melting point, compared to S, makes it challenging to synthesize large-scale, atomically thin Se-based TMDCs. In this work, an innovative APCVD alkali metal-assisted (provided by the Na-containing glass substrates) route using Se powder and Mo foil precursors was successfully optimized. First, the optimal gap between the Mo foil and the substrate revealed to be 0.7cm. Furthermore, the distance between the substrate and Se powder revealed crucial since it affects Se powder evaporation rate. The optimal distance was shown to be 45cm. As expected, Hydrogen shown to have a crucial role on flake shape, size, and quality. The optimal flux during growth was found to be Ar(50sccm)+H_2(10sccm). In this process, due to the usage of a borosilicate glass, growth temperature needs to be chosen wisely. In order to keep the substrate with the minimum damage a temperature of 720°C was chosen. Finally, a growth time of 12 min revealed to be optimal in order to growth large monolayer flakes. The optimized APVCD protocol allows to grow μm-sized $MoSe_2$ crystalline monolayer domains (sporadic bilayer and few-layer regions appear) on a borosilicate substrate. These domains sometimes coalesce and form a continuous film in the border regions of the substrate. The flakes showed intense photoluminescence in monolayer regions with quenched intensity in bilayer regions, as expected. However, the presence of Na/Se/O nanoparticles of unknown stoichiometry resulted from growth, as demonstrated by HRTEM and XPS. Our investigation showed that the nanoparticles are embedded within the $MoSe_2$ crystals or aligned along the grain edges and are not removed after the dry-transfer steps. The viability of integrating the grown $MoSe_2$ flakes into flexible optoelectronic applications was studied. In this regard, uniaxial strain was induced in the flakes and Raman and PL were measured. The results follow quite well the literature, proving that PL emission behavior is tunable by strain engineering. Thus, this novel route proved to be a viable and simple route to grow single-crystalline monolayer $MoSe_2$ flakes on a borosilicate glass, a substrate relevant for transparent applications.

6. Future Outlook

Following the conclusions, future studies concerning the two atmospheric-pressure CVD procedures can be envisaged. Regarding 2D hBN films, the main optimization would regard a way to suppress the presence of SiO_x nanoparticles, which are typical of CVD processes carried out in quartz furnaces using Cu substrates. Following an approach proposed for the CVD growth of graphene, this could be achieved by introducing an inert confinement box (with a small open slit) to hold the Cu foil [122]. Nonetheless, the use of said box would interfere with the flow dynamics during the process, so further optimization steps will be required. As a further improvement, an additional Cu pre-treatment could be introduced, such as electropolishing. In electropolished substrates the nucleation density of h-BN is significantly reduced while the domain size increases [86]. By achieving larger h-BN domains, the grain boundary-induced defects would be effectively reduced, increasing the crystallinity. Regarding the use of hBN films as reliable SPE sources, this work demonstrated a strong evidence of SPE at room temperature. However, it will be pivotal to measure and interpret the $g^{(2)}(\tau)$ function of the emission.

About 2D $MoSe_2$, the remaining concern of the novel route employed in this work is the use of glass as substrate. As shown, the glass substrates can partially soften during the CVD process. This can lead to a certain surface waviness that might induce intrinsic strain on the flakes, affect the optoelectronic properties. Other than that, this also brings additional complexity to the transfer process. The role of different Na concentrations (given by the different substrates) on the grown $MoSe_2$ flakes should be also evaluated. Regarding the strain studies, higher strain levels (such as 1%) should be tested, as well as compressive strain conditions.

REFERENCES

1. Mounet N, Gibertini M, Schwaller P, Campi D, Merkys A, Marrazzo A, Sohier T, Castelli IE, Cepellotti A, Pizzi G, Marzari N. Two-dimensional materials from high-throughput computational exfoliation of experimentally known compounds. Nat Nanotechnol [Internet]. 2018;13(3):246–52.
2. Khandelwal A, Mani K, Karigerasi MH, Lahiri I. Phosphorene – The two-dimensional black phosphorous: Properties, synthesis and applications. Mater Sci Eng B Solid-State Mater Adv Technol. 2017;221:17–34.
3. Rubab A, Baig N, Sher M, Sohail M. Advances in ultrathin borophene materials. Chem Eng J [Internet]. 2020;401:126109.
4. Kara A, Enriquez H, Seitsonen AP, Lew Yan Voon LC, Vizzini S, Aufray B, Oughaddou H. A review on silicene - New candidate for electronics. Surf Sci Rep. 2012;67(1):1–18.
5. Dávila ME, Xian L, Cahangirov S, Rubio A, Le Lay G. Germanene: A novel two-dimensional germanium allotrope akin to graphene and silicene. New J Phys. 2014;16.
6. Lyu JK, Zhang SF, Zhang CW, Wang PJ. Stanene: A Promising Material for New Electronic and Spintronic Applications. Ann Phys. 2019;531(10):1–12.
7. Cai X, Han X, Zhao C, Niu C, Jia Y. Tellurene: An elemental 2D monolayer material beyond its bulk phases without van der Waals layered structures. J Semicond. 2020;41(8).
8. Dobrzhinetskaya LF, Wirth R, Yang J, Hutcheon ID, Weber PK, Green HW. High-pressure highly reduced nitrides and oxides from chromitite of a Tibetan ophiolite. Proc Natl Acad Sci U S A. 2009;106(46):19233–8.
9. Mishima O, Yamaoka S. Diode Made at High Pressure.
10. Kubota Y, Watanabe K, Tsuda O, Taniguchi T. Deep ultraviolet light-emitting hexagonal boron nitride synthesized at atmospheric pressure. Science (80-). 2007;317(5840):932–4.
11. Watanabe K, Taniguchi T, Kanda H. Direct-bandgap properties and evidence for ultraviolet lasing of hexagonal boron nitride single crystal. Nat Mater. 2004;3(6):404–9.
12. Constantinescu G, Kuc A, Heine T. Stacking in bulk and bilayer hexagonal boron nitride. Phys Rev Lett. 2013;111(3):1–5.
13. Benka SG. Two-dimensional atomic crystals. Phys Today. 2005;58(9):9–9.
14. Zhi C, Bando Y, Tang C, Golberg D. Boron nitride nanotubes. Mater Sci Eng R Reports. 2010;70(3–6):92–111.
15. Kim SS, Van Khai T, Kwon YJ, Katoch A, Wu P, Kim HW. One-pot synthesis of h-BN fullerenes usinsg a graphene oxide template. Met Mater Int. 2015;21(5):950–5.
16. Chen ZG, Zou J, Liu G, Li F, Wang Y, Wang L, Yuan XL, Sekiguchi T, Cheng HM, Lu GQ. Novel boron nitride hollow nanoribbons. ACS Nano. 2008;2(10):2183–91.
17. Chen YJ, Zhang HZ, Chen Y. Pure boron nitride nanowires produced from boron triiodide. Nanotechnology. 2006;17(3):786–9.
18. Qiu Y, Yu J, Yin J, Tan C, Zhou X, Bai X, Wang E. Synthesis of continuous boron nitride nanofibers by solution coating electrospun template fibers. Nanotechnology. 2009;20(34).
19. Yin J, Li X, Zhou J, Guo W. Ultralight three-dimensional boron nitride foam with ultralow permittivity and superelasticity. Nano Lett. 2013;13(7):3232–6.
20. Giovannetti G, Khomyakov PA, Brocks G, Kelly PJ, Van Den Brink J. Substrate-induced band gap in graphene on hexagonal boron nitride: Ab initio density functional calculations. Phys Rev B - Condens Matter Mater Phys. 2007;76(7):2–5.
21. Dean CR, Young AF, Meric I, Lee C, Wang L, Sorgenfrei S. Boron nitride substrates for high quality graphene electronics. NatureCom.
22. Ji Y, Pan C, Zhang M, Long S, Lian X, Miao F, Hui F, Shi Y, Larcher L, Wu E, Lanza M. Boron nitride as two dimensional dielectric: Reliability and dielectric breakdown. Appl Phys Lett.

2016;108(1).
23. Mayorov AS, Gorbachev R V., Morozov S V., Britnell L, Jalil R, Ponomarenko LA, Blake P, Novoselov KS, Watanabe K, Taniguchi T, Geim AK. Micrometer-scale ballistic transport in encapsulated graphene at room temperature. Nano Lett. 2011;11(6):2396–9.
24. Ju L, Velasco J, Huang E, Kahn S, Nosiglia C, Tsai HZ, Yang W, Taniguchi T, Watanabe K, Zhang Y, Zhang G, Crommie M, Zettl A, Wang F. Photoinduced doping in heterostructures of graphene and boron nitride. Nat Nanotechnol. 2014;9(5):348–52.
25. Xu YN, Ching WY. Calculation of ground-state and optical properties of boron nitrides in the hexagonal, cubic, and wurtzite structures. Phys Rev B. 1991;44(15):7787–98.
26. Gao SP. Crystal structures and band gap characters of h-BN polytypes predicted by the dispersion corrected DFT and GW method. Solid State Commun. 2012;152(19):1817–20.
27. Cassabois G, Valvin P, Gil B. Hexagonal boron nitride is an indirect bandgap semiconductor. Nat Photonics. 2016;10(4):262–6.
28. Elias C, Valvin P, Pelini T, Summerfield A, Mellor CJ, Cheng TS, Eaves L, Foxon CT, Beton PH, Novikov S V., Gil B, Cassabois G. Direct band-gap crossover in epitaxial monolayer boron nitride. Nat Commun. 2019;10(1):1–7.
29. Aldalbahi A, Feng P. Development of 2-D boron nitride nanosheets UV photoconductive detectors. IEEE Trans Electron Devices. 2015;62(6):1885–90.
30. Aharonovich I, Englund D, Toth M. Solid-state single-photon emitters. Nat Photonics. 2016;10(10):631–41.
31. Toth M, Aharonovich I. Single Photon Sources in Atomically Thin Materials. Annu Rev Phys Chem. 2019;70:123–42.
32. Ngoc My Duong H, Nguyen MAP, Kianinia M, Ohshima T, Abe H, Watanabe K, Taniguchi T, Edgar JH, Aharonovich I, Toth M. Effects of High-Energy Electron Irradiation on Quantum Emitters in Hexagonal Boron Nitride. ACS Appl Mater Interfaces. 2018;10(29):24886–91.
33. Vogl T, Campbell G, Buchler BC, Lu Y, Lam PK. Fabrication and Deterministic Transfer of High-Quality Quantum Emitters in Hexagonal Boron Nitride. ACS Photonics. 2018;5(6):2305–12.
34. Naguib M, Mashtalir O, Carle J, Presser V, Lu J, Hultman L, Gogotsi Y, Barsoum MW. Two-Dimensional Transition-Metal Dichalcogenides. Vol. 6, ACS Nano. 2012. 1322–1331 p.
35. Wang Y, Ni Y. Molybdenum disulfide quantum dots as a photoluminescence sensing platform for 2,4,6-trinitrophenol detection. Anal Chem. 2014;86(15):7463–70.
36. Hong X, Liu J, Zheng B, Huang X, Zhang X, Tan C, Chen J, Fan Z, Zhang H. A Universal Method for Preparation of Noble Metal Nanoparticle-Decorated Transition Metal Dichalcogenide Nanobelts. Adv Mater. 2014;26(36):6250–4.
37. Gibertini M, Marzari N. Emergence of One-Dimensional Wires of Free Carriers in Transition-Metal-Dichalcogenide Nanostructures. Nano Lett. 2015;15(9):6229–38.
38. Mobilities H, Pradhan NR, Rhodes D, Xin Y, Memaran S, Bhaskaran L, Siddiq M. Ambipolar Molybdenum Diselenide. ACS Nano. 2014;(8):7923–9.
39. Larentis S, Fallahazad B, Tutuc E. Field-effect transistors and intrinsic mobility in ultra-thin MoSe 2 layers. Appl Phys Lett. 2012;101(22).
40. Sarkar P De, Paul A, Ghosh KK. Thin Film Dichalcogenide MoSe2 Solar Cell with Optimized Design Parameters. IOSR J Electron Commun Eng. 2017;12(03):13–7.
41. Hsiao KJ, Liu J Da, Hsieh HH, Jiang TS. Electrical impact of MoSe2 on CIGS thin-film solar cells. Phys Chem Chem Phys. 2013;15(41):18174–8.
42. Chang YH, Zhang W, Zhu Y, Han Y, Pu J, Chang JK, Hsu WT, Huang JK, Hsu CL, Chiu MH, Takenobu T, Li H, Wu CI, Chang WH, Wee ATS, Li LJ. Monolayer MoSe2 grown by chemical vapor deposition for fast photodetection. ACS Nano. 2014 Aug;8(8):8582–90.
43. Du W, Yu P, Zhu J, Li C, Xu H. An ultrathin MoSe2 photodetector with near-perfect absorption.

2018;
44. Silva JPB, Almeida Marques C, Moreira JA, Conde O. Resistive switching in MoSe2/BaTiO3 hybrid structures. J Mater Chem C. 2017;5(39):10353–9.
45. Vitale SA, Nezich D, Varghese JO, Kim P, Gedik N, Jarillo-Herrero P, Xiao D, Rothschild M. Valleytronics: Opportunities, Challenges, and Paths Forward. Small. 2018;14(38):1–15.
46. Lundt N, Maryński A, Cherotchenko E, Pant A, Fan X, Tongay S, Sek G, Kavokin A V., Höfling S, Schneider C. Monolayered MoSe2: A candidate for room temperature polaritonics. 2D Mater. 2017;4(1).
47. Feng S, Lin Z, Gan X, Lv R, Terrones M. Doping two-dimensional materials: Ultra-sensitive sensors, band gap tuning and ferromagnetic monolayers. Nanoscale Horizons. 2017;2(2):72–80.
48. Yang S, Kang J, Yue Q, Coey JMD, Jiang C. Defect-Modulated Transistors and Gas-Enhanced Photodetectors on ReS2 Nanosheets. Adv Mater Interfaces. 2016;3(6):1–5.
49. Search H, Journals C, Contact A, Iopscience M, Address IP, Rahman AM, Manuscript TA, Publishing IOP, Manuscript A, Manuscript A, By-nc-nd CC, Manuscript A. Electronic and optical properties of strained graphene and other strained 2D materials: a review. 2017;0–68.
50. Akinwande D, Petrone N, Hone J. Two-dimensional flexible nanoelectronics. Nature Communications. 2014.
51. Conley HJ, Wang B, Ziegler JI, Haglund RF, Pantelides ST, Bolotin KI. Bandgap engineering of strained monolayer and bilayer MoS2. Nano Lett. 2013;13(8):3626–30.
52. Zhu CR, Wang G, Liu BL, Marie X, Qiao XF, Zhang X, Wu XX, Fan H, Tan PH, Amand T, Urbaszek B. Strain tuning of optical emission energy and polarization in monolayer and bilayer MoS2. Phys Rev B - Condens Matter Mater Phys. 2013;88(12):1–5.
53. De Fazio D, Goykhman I, Yoon D, Bruna M, Eiden A, Milana S, Sassi U, Barbone M, Dumcenco D, Marinov K, Kis A, Ferrari AC. High Responsivity, Large-Area Graphene/MoS2 Flexible Photodetectors. ACS Nano. 2016;10(9):8252–62.
54. Cheng X, Jiang L, Li Y, Zhang H, Hu C, Xie S, Liu M, Qi Z. Using strain to alter the energy bands of the monolayer MoSe2: A systematic study covering both tensile and compressive states. Appl Surf Sci. 2020 Aug;521(April):146398.
55. Island JO, Kuc A, Diependaal EH, Bratschitsch R, Van Der Zant HSJ, Heine T, Castellanos-Gomez A. Precise and reversible band gap tuning in single-layer MoSe2 by uniaxial strain. Nanoscale. 2016;8(5):2589–93.
56. Ji J, Zhang A, Xia T, Gao P, Jie Y, Zhang Q, Zhang Q. Strain-modulated excitonic gaps in mono- and bi-layer MoSe2. Chinese Phys B. 2016;25(7).
57. Alem N, Erni R, Kisielowski C, Rossell MD, Gannett W, Zettl A. Atomically thin hexagonal boron nitride probed by ultrahigh-resolution transmission electron microscopy. Phys Rev B - Condens Matter Mater Phys. 2009;80(15):1–7.
58. Magda GZ, Pető J, Dobrik G, Hwang C, Biró LP, Tapasztó L. Exfoliation of large-area transition metal chalcogenide single layers. Sci Rep. 2015;5:3–7.
59. Petrelli C, Goos A, Ruhlandt-Senge K, Spencer JT. Functionalization of boron nitride nanosheets (BNNSs) by organic polymers: formation of substituted polythiophene–BNNS structures. J Mater Sci. 2016;51(10):4952–62.
60. Han WQ, Wu L, Zhu Y, Watanabe K, Taniguchi T. Structure of chemically derived mono- and few-atomic-layer boron nitride sheets. Appl Phys Lett. 2008;93(22):91–4.
61. Zhi C, Bando Y, Tang C, Kuwahara H, Golberg D. Large-scale fabrication of boron nitride nanosheets and their utilization in polymeric composites with improved thermal and mechanical properties. Adv Mater. 2009;21(28):2889–93.
62. Kumar R, Singh RK, Yadav SK, Savu R, Moshkalev SA. Mechanical pressure induced chemical cutting of boron nitride sheets into boron nitride quantum dots and optical properties. J Alloys

Compd. 2016;683:38–45.
63. Wang Y, Shi Z, Yin J. Boron nitride nanosheets: Large-scale exfoliation in methanesulfonic acid and their composites with polybenzimidazole. J Mater Chem. 2011;21(30):11371–7.
64. Lin Y, Williams T V., Connell JW. Soluble, exfoliated hexagonal boron nitride nanosheets. J Phys Chem Lett. 2010;1(1):277–83.
65. Coleman JN, Lotya M, O'Neill A, Bergin SD, King PJ, Khan U, Young K, Gaucher A, De S, Smith RJ, Shvets I V., Arora SK, Stanton G, Kim HY, Lee K, Kim GT, Duesberg GS, Hallam T, Boland JJ, Wang JJ, Donegan JF, Grunlan JC, Moriarty G, Shmeliov A, Nicholls RJ, Perkins JM, Grieveson EM, Theuwissen K, McComb DW, Nellist PD, Nicolosi V. Two-dimensional nanosheets produced by liquid exfoliation of layered materials. Science (80-). 2011;331(6017):568–71.
66. Gupta U, Naidu BS, Maitra U, Singh A, Shirodkar SN, Waghmare U V., Rao CNR. Characterization of few-layer 1T-MoSe2 and its superior performance in the visible-light induced hydrogen evolution reaction. APL Mater [Internet]. 2014;2(9).
67. Wang H, Zhang X, Liu H, Yin Z, Meng J, Xia J, Meng XM, Wu J, You J. Synthesis of Large-Sized Single-Crystal Hexagonal Boron Nitride Domains on Nickel Foils by Ion Beam Sputtering Deposition. Adv Mater. 2015;27(48):8109–15.
68. Sutter P, Lahiri J, Zahl P, Wang B, Sutter E. Scalable synthesis of uniform few-layer hexagonal boron nitride dielectric films. Nano Lett. 2013;13(1):276–81.
69. Cheng TS, Summerfield A, Mellor CJ, Davies A, Khlobystov AN, Eaves L, Foxon CT, Beton PH, Novikov S V. High-temperature molecular beam epitaxy of hexagonal boron nitride layers. J Vac Sci Technol B, Nanotechnol Microelectron Mater Process Meas Phenom. 2018;36(2):02D103.
70. Hirama K, Taniyasu Y, Karimoto SI, Krockenberger Y, Yamamoto H. Single-crystal cubic boron nitride thin films grown by ion-beam-assisted molecular beam epitaxy. Appl Phys Lett. 2014;104(9).
71. Muratore C, Hu JJ, Wang B, Haque MA, Bultman JE, Jespersen ML, Shamberger PJ, McConney ME, Naguy RD, Voevodin AA. Continuous ultra-thin MoS2 films grown by low-temperature physical vapor deposition. Appl Phys Lett. 2014;104(26):1–6.
72. Li N, Liu ZT, Feng LP, Su J, Li DP, Zeng W. Effect of substrate temperature on the electrical characteristics of MoSex thin films and back-gated MoSex transistors. J Alloys Compd [Internet]. 2015;623:209–12.
73. Zhu Y, Yang J. MoS2 materials synthesized on SiO 2/Si substrates via MBE. 2017;6–10.
74. Nakano M, Wang Y, Kashiwabara Y, Matsuoka H, Iwasa Y. Layer-by-Layer Epitaxial Growth of Scalable WSe2 on Sapphire by Molecular Beam Epitaxy. Nano Lett. 2017;17(9):5595–9.
75. Jiao L, Liu HJ, Chen JL, Yi Y, Chen WG, Cai Y, Wang JN, Dai XQ, Wang N, Ho WK, Xie MH. Molecular-beam epitaxy of monolayer MoSe2: Growth characteristics and domain boundary formation. New J Phys. 2015;17.
76. Baptista A, Silva FJG, Porteiro J, Míguez JL, Pinto G, Fernandes L. On the Physical Vapour Deposition (PVD): Evolution of Magnetron Sputtering Processes for Industrial Applications. Procedia Manuf [Internet]. 2018;17:746–57.
77. Sun L, Yuan G, Gao L, Yang J, Chhowalla M, Gharahcheshmeh MH, Gleason KK, Choi YS, Hong BH, Liu Z. Chemical vapour deposition. Nat Rev [Internet]. 2021;1–20.
78. Cai Z, Liu B, Zou X, Cheng HM. Chemical Vapor Deposition Growth and Applications of Two-Dimensional Materials and Their Heterostructures. Chem Rev. 2018;118(13):6091–133.
79. Torigoe M, Kamimura Y, Teii K, Matsumoto S. Effect of low-energy ion impact on the structure of hexagonal boron nitride films studied in surface-wave plasma. Surf Interface Anal. 2019;51(1):126–30.
80. Arias P, Ebnonnasir A, Ciobanu C V., Kodambaka S. Growth Kinetics of Two-Dimensional Hexagonal Boron Nitride Layers on Pd(111). Nano Lett. 2020;20(4):2886–91.

81. Shi Z, Wang X, Li Q, Yang P, Lu G, Jiang R, Wang H, Zhang C, Cong C, Liu Z, Wu T, Wang H, Yu Q, Xie X. Vapor–liquid–solid growth of large-area multilayer hexagonal boron nitride on dielectric substrates. Nat Commun [Internet]. 2020;11(1):1–8.
82. Khan MH, Liu HK, Sun X, Yamauchi Y, Bando Y, Golberg D, Huang Z. Few-atomic-layered hexagonal boron nitride: CVD growth, characterization, and applications. Mater Today [Internet]. 2017;20(10):611–28.
83. Babenko V, Lane G, Koos AA, Murdock AT, So K, Britton J, Meysami SS, Moffat J, Grobert N. Time dependent decomposition of ammonia borane for the controlled production of 2D hexagonal boron nitride. Sci Rep. 2017;7(1):1–12.
84. Wen Y, Shang X, Dong J, Xu K, He J, Jiang C. Ultraclean and large-area monolayer hexagonal boron nitride on Cu foil using chemical vapor deposition. Nanotechnology. 2015;26(27):1–8.
85. Kim KK, Hsu A, Jia X, Kim SM, Shi Y, Hofmann M, Nezich D, Rodriguez-Nieva JF, Dresselhaus M, Palacios T, Kong J. Synthesis of monolayer hexagonal boron nitride on Cu foil using chemical vapor deposition. Nano Lett. 2012;12(1):161–6.
86. Tay RY, Griep MH, Mallick G, Tsang SH, Singh RS, Tumlin T, Teo EHT, Karna SP. Growth of large single-crystalline two-dimensional boron nitride hexagons on electropolished copper. Nano Lett. 2014;14(2):839–46.
87. Wang L, Wu B, Chen J, Liu H, Hu P, Liu Y. Field-Effect Transistors: Monolayer Hexagonal Boron Nitride Films with Large Domain Size and Clean Interface for Enhancing the Mobility of Graphene-Based Field-Effect Transistors (Adv. Mater. 10/2014). Adv Mater. 2014;26(10):1474–1474.
88. Ismach A, Chou H, Ferrer DA, Wu Y, McDonnell S, Floresca HC, Covacevich A, Pope C, Piner R, Kim MJ, Wallace RM, Colombo L, Ruoff RS. Toward the controlled synthesis of hexagonal boron nitride films. ACS Nano. 2012;6(7):6378–85.
89. Wang L, Xu X, Zhang L, Qiao R, Wu M, Wang Z, Zhang S, Liang J, Zhang Z, Zhang Z, Chen W, Xie X, Zong J, Shan Y, Guo Y, Willinger M, Wu H, Li Q, Wang W, Gao P, Wu S, Zhang Y, Jiang Y, Yu D, Wang E, Bai X, Wang ZJ, Ding F, Liu K. Epitaxial growth of a 100-square-centimetre single-crystal hexagonal boron nitride monolayer on copper. Nature [Internet]. 2019;570(7759):91–5.
90. Song L, Ci L, Lu H, Sorokin PB, Jin C, Ni J, Kvashnin AG, Kvashnin DG, Lou J, Yakobson BI, Ajayan PM. Large scale growth and characterization of atomic hexagonal boron nitride layers. Nano Lett. 2010;10(8):3209–15.
91. Tay RY, Wang X, Tsang SH, Loh GC, Singh RS, Li H, Mallick G, Tong Teo EH. A systematic study of the atmospheric pressure growth of large-area hexagonal crystalline boron nitride film. J Mater Chem C. 2014;2(9):1650–7.
92. Song X, Li Q, Ji J, Yan Z, Gu Y, Huo C, Zou Y, Zhi C, Zeng H. A comprehensive investigation on CVD growth thermokinetics of h-BN white graphene. 2D Mater. 2016;3(3).
93. Stehle Y, Meyer HM, Unocic RR, Kidder M, Polizos G, Datskos PG, Jackson R, Smirnov SN, Vlassiouk I V. Synthesis of Hexagonal Boron Nitride Monolayer: Control of Nucleation and Crystal Morphology. Chem Mater. 2015;27(23):8041–7.
94. Shaw JC, Zhou H, Chen Y, Weiss NO, Liu Y, Huang Y, Duan X. Chemical vapor deposition growth of monolayer MoSe2 nanosheets. Nano Res. 2014;7(4):1–7.
95. Sial MN, Usman M, Zheng B, Yu Y, Mavrič A, Qing F, Valant M, Wang ZM. CVD growth of molybdenum diselenide surface structures with tailored morphology. CrystEngComm. 2018;20(33):4867–74.
96. Li Y, Wang F, Tang D, Wei J, Li Y, Xing Y, Zhang K. Controlled synthesis of highly crystalline CVD-derived monolayer MoSe2 and shape evolution mechanism. Mater Lett. 2018;216:261–4.
97. Wang S, Wang G, Yang X, Yang H, Zhu M, Zhang S, Peng G, Li Z. Synthesis of monolayer MoSe2 with controlled nucleation via reverse-flow chemical vapor deposition. Nanomaterials. 2020;10(1).
98. Campbell PM, Friedman AL, Hanbicki AT, Sivaram S V, Kusterbeck AJ, Nguyen VK, Andrew McGill

R. Chemical vapor sensing with CVD-grown monolayer MoSe2 using photoluminescence modulation. Appl Phys Lett. 2018;113(16).
99. Zhao Y, Lee H, Choi W, Fei W, Lee CJ. Large-area synthesis of monolayer MoSe2 films on SiO2/Si substrates by atmospheric pressure chemical vapor deposition. RSC Adv. 2017;7(45):27969–73.
100. Chen T, Hao G, Wang G, Li B, Kou L, Yang H, Zheng X, Zhong J. Controlled growth of atomically thin MoSe2 films and nanoribbons by chemical vapor deposition. 2D Mater. 2019;6(2).
101. Lu X, Utama MIB, Lin J, Gong X, Zhang J, Zhao Y, Pantelides ST, Wang J, Dong Z, Liu Z, Zhou W, Xiong Q. Large-area synthesis of monolayer and few-layer MoSe2 films on SiO2 substrates. Nano Lett. 2014;
102. Kong D, Wang H, Cha JJ, Pasta M, Koski KJ, Yao J, Cui Y. Synthesis of MoS2 and MoSe2 films with vertically aligned layers. Nano Lett. 2013;13(3):1341–7.
103. Tai G, Zeng T, Yu J, Zhou J, You Y, Wang X, Wu H, Sun X, Hu T, Guo W. Fast and large-area growth of uniform MoS2 monolayers on molybdenum foils. Nanoscale. 2016;8(4):2234–41.
104. Liu J, Zeng M, Wang L, Chen Y, Xing Z, Zhang T, Liu Z, Zuo J, Nan F, Mendes RG, Chen S, Ren F, Wang Q, Rümmeli MH, Fu L. Ultrafast Self-Limited Growth of Strictly Monolayer WSe2 Crystals. Small. 2016;12(41):5741–9.
105. Park JC, Yun SJ, Kim H, Park JH, Chae SH, An SJ, Kim JG, Kim SM, Kim KK, Lee YH. Phase-Engineered Synthesis of Centimeter-Scale 1T′- and 2H-Molybdenum Ditelluride Thin Films. ACS Nano. 2015;9(6):6548–54.
106. Li J, Yan W, Lv Y, Leng J, Zhang D, Coileaín CO, Cullen CP, Stimpel-Lindner T, Duesberg GS, Cho J, Choi M, Chun BS, Zhao Y, Lv C, Arora SK, Wu HC. Sub-millimeter size high mobility single crystal MoSe2 monolayers synthesized by NaCl-assisted chemical vapor deposition. RSC Adv. 2020;10(3):1580–7.
107. Yan H, Yu T, Li H, Li Z, Tang H, Hu H, Yu H, Yin S. Synthesis of large-area monolayer and few-layer MoSe2continuous films by chemical vapor deposition without hydrogen assistance and formation mechanism. Nanoscale. 2021;13(19):8922–30.
108. Wang W, Shu H, Zhou D, Wang J, Chen X. Ultrafast nucleation and growth of high-quality monolayer MoSe2crystals via vapor-liquid-solid mechanism. Nanotechnology. 2020;31(33).
109. Chen J, Zhao X, Tan SJR, Xu H, Wu B, Liu B, Fu D, Fu W, Geng D, Liu Y, Liu W, Tang W, Li L, Zhou W, Sum TC, Loh KP. Chemical Vapor Deposition of Large-Size Monolayer MoSe 2 Crystals on Molten Glass . J Am Chem Soc. 2017;139(3):1073–6.
110. Li LH, Chen Y. Atomically Thin Boron Nitride: Unique Properties and Applications. Adv Funct Mater. 2016;26(16):2594–608.
111. Tonndorf P, Schmidt R, Bottger P, Zhang X, Borner J, Liebig A, Albrecht M, Kloc C, Gordan O, Zahn DRT, De Vasconcellos SM, Bratschitsch R. Photoluminescence emission and Raman response of MoS2, MoSe 2, and WSe2 nanolayers. 2013 Conf Lasers Electro-Optics, CLEO 2013. 2013;(February).
112. McCreary KM, Hanbicki AT, Sivaram S V., Jonker BT. A- and B-Exciton Photoluminescence Intensity Ratio as a Measure of Sample Quality for Transition Metal Dichalcogenide Monolayers. arXiv. 2018;1–17.
113. Leng Y. Materials Characterization: Introduction to Microscopic and Spectroscopic Methods. 2008. 383 p.
114. Sharma S. Handbook of Materials Characterization. 2018. 77–111 p.
115. Ingo GM, Padeletti G, De Caro T, Riccucci C, Faraldi F, Curulli A, Mezzi A, Piccinini M. Novel route to high-yield synthesis of sp2-hybridized boron nitride nanoplates on stainless steel. J Mater Chem. 2011;21(28):10268–72.
116. Krivanek OL, Chisholm MF, Nicolosi V, Pennycook TJ, Corbin GJ, Dellby N, Murfitt MF, Own CS, Szilagyi ZS, Oxley MP, Pantelides ST, Pennycook SJ. Atom-by-atom structural and chemical

analysis by annular dark-field electron microscopy. Nature. 2010;464(7288):571–4.
117. Xia J, Huang X, Liu LZ, Wang M, Wang L, Huang B, Zhu DD, Li JJ, Gu CZ, Meng XM. CVD synthesis of large-area, highly crystalline MoSe2 atomic layers on diverse substrates and application to photodetectors. Nanoscale. 2014;6(15):8949–55.
118. Zhao Y, Lee H, Choi W, Fei W, Lee CJ. Large-area synthesis of monolayer MoSe2 films on SiO2/Si substrates by atmospheric pressure chemical vapor deposition. RSC Adv. 2017;7(45):27969–73.
119. Li X, Zhu Y, Cai W, Borysiak M, Han B, Chen D, Piner RD, Colomba L, Ruoff RS. Transfer of large-area graphene films for high-performance transparent conductive electrodes. Nano Lett. 2009;9(12):4359–63.
120. Song Y, Zhang C, Li B, Jiang D, Ding G, Wang H, Xie X. Triggering the atomic layers control of hexagonal boron nitride films. Appl Surf Sci [Internet]. 2014;313:647–53.
121. Iqbal MW, Iqbal MZ, Khan MF, Shehzad MA, Seo Y, Park JH, Hwang C, Eom J. High-mobility and air-stable single-layer WS2 field-effect transistors sandwiched between chemical vapor deposition-grown hexagonal BN films. Sci Rep [Internet]. 2015;5(June).
122. Lisi N, Dikonimos T, Buonocore F, Pittori M, Mazzaro R, Rizzoli R, Marras S, Capasso A. Contamination-free graphene by chemical vapor deposition in quartz furnaces. Sci Rep [Internet]. 2017;7(1):1–11.
123. Kidambi PR, Blume R, Kling J, Wagner JB, Baehtz C, Weatherup RS, Schloegl R, Bayer BC, Hofmann S. In situ observations during chemical vapor deposition of hexagonal boron nitride on polycrystalline copper. Chem Mater. 2014;26(22):6380–92.
124. Mendelson N, Xu ZQ, Tran TT, Kianinia M, Scott J, Bradac C, Aharonovich I, Toth M. Engineering and Tuning of Quantum Emitters in Few-Layer Hexagonal Boron Nitride. ACS Nano. 2019;13(3):3132–40.
125. Ziegler J, Klaiss R, Blaikie A, Miller D, Horowitz VR, Alemán BJ. Deterministic Quantum Emitter Formation in Hexagonal Boron Nitride via Controlled Edge Creation. Nano Lett. 2019;19(3):2121–7.
126. Stern HL, Wang R, Fan Y, Mizuta R, Stewart JC, Needham LM, Roberts TD, Wai R, Ginsberg NS, Klenerman D, Hofmann S, Lee SF. Spectrally Resolved Photodynamics of Individual Emitters in Large-Area Monolayers of Hexagonal Boron Nitride. ACS Nano. 2019;13(4):4538–47.
127. Lee J, Leong V, Kalashnikov D, Dai J, Gandhi A, Krivitsky L. Integrated Single Photon Emitters. AVS Quantum Sci. 2020;2:1–46.
128. Grosso G, Moon H, Lienhard B, Ali S, Efetov DK, Furchi MM, Jarillo-Herrero P, Ford MJ, Aharonovich I, Englund D. Tunable and high-purity room temperature single-photon emission from atomic defects in hexagonal boron nitride. Nat Commun [Internet]. 2017;8(1):1–8.
129. Xu ZQ, Elbadawi C, Tran TT, Kianinia M, Li X, Liu D, Hoffman TB, Nguyen M, Kim S, Edgar JH, Wu X, Song L, Ali S, Ford M, Toth M, Aharonovich I. Single photon emission from plasma treated 2D hexagonal boron nitride. Nanoscale. 2018;10(17):7957–65.
130. Castellanos-Gomez A, Vicarelli L, Prada E, Gacem K, Boukhicha M, Chen Z, Uwanno T, Hattori Y, Taniguchi T, Ferraz Da Costa MC, Ribeiro HB, Kessler F, Spectroscopy R, Park J-H, Choi SH, Chae WU, Sinha S, Takabayashi Y, Shinohara H, Buscema M, Molenaar R, Singh V, Janssen L, van der Zant HSJ, Steele GA. Deterministic transfer of two-dimensional materials by all-dry viscoelastic stamping. 2D Mater. 2014;1(1):011002.
131. Yang P, Zou X, Zhang Z, Hong M, Shi J, Chen S, Shu J, Zhao L, Jiang S, Zhou X, Huan Y, Xie C, Gao P, Chen Q, Zhang Q, Liu Z, Zhang Y. Batch production of 6-inch uniform monolayer molybdenum disulfide catalyzed by sodium in glass. Nat Commun [Internet]. 2018;9(1):1–10.
132. Zhao S, Lu M, Xue SS, Yan L, Miao P, Hang Y, Wang X, Liu Z, Wang Y, Tao L, Sui Y, Wang Y. A Se vacancy induced localized Raman mode in two-dimensional MoSe2 grown by CVD. arXiv. 2019;1–16.

133. Zheng J, Yan X, Lu Z, Qiu H, Xu G, Zhou X, Wang P, Pan X, Liu K, Jiao L. High-Mobility Multilayered MoS2 Flakes with Low Contact Resistance Grown by Chemical Vapor Deposition. Adv Mater. 2017;29(13):2–7.
134. Li B, Gong Y, Hu Z, Brunetto G, Yang Y, Ye G, Zhang Z, Lei S, Jin Z, Bianco E, Zhang X, Wang W, Lou J, Galvão DS, Tang M, Yakobson BI, Vajtai R, Ajayan PM. Solid–Vapor Reaction Growth of Transition-Metal Dichalcogenide Monolayers. Angew Chemie - Int Ed. 2016;
135. Cheng X, Jiang L, Li Y, Zhang H, Hu C, Xie S, Liu M, Qi Z. Using strain to alter the energy bands of the monolayer MoSe2: A systematic study covering both tensile and compressive states. Appl Surf Sci [Internet]. 2020;521(March):146398.
136. Li S, Lin YC, Hong J, Gao B, Lim HE, Yang X, Liu S, Tateyama Y, Tsukagoshi K, Sakuma Y, Suenaga K, Taniguchi T. Mixed-Salt Enhanced Chemical Vapor Deposition of Two-Dimensional Transition Metal Dichalcogenides. Chem Mater. 2021;33(18):7301–8.
137. Wagner CD. Chemical shifts of Auger lines, and the Auger parameter. Faraday Discuss Chem Soc. 1975 Jan;60(0):291–300.
138. Park S, Champness CH, Shih I. XPS Se 3d peaks in Na-added Bridgman CuInSe2+x. In: 2015 IEEE 42nd Photovoltaic Specialist Conference, PVSC 2015. Institute of Electrical and Electronics Engineers Inc.; 2015.
139. Hanson ED, Lilley LM, Cain JD, Hao S, Palacios E, Aydin K, Wolverton C, Meade T, Dravid VP. Phase engineering and optical properties of 2D MoSe 2 : Promise and pitfalls. Mater Chem Phys. 2019;225(January 2018):219–26.
140. Wang X, Gong Y, Shi G, Chow WL, Keyshar K, Ye G, Vajtai R, Lou J, Liu Z, Ringe E, Tay BK, Ajayan PM. Chemical vapor deposition growth of crystalline monolayer MoSe2. ACS Nano. 2014;
141. Roldán R, Castellanos-Gomez A, Cappelluti E, Guinea F. Strain engineering in semiconducting two-dimensional crystals. J Phys Condens Matter. 2015;27(31).